Technische Universität München
Fakultät für Physik

Master Thesis

Measurement of the $pp \to H \to ZZ^* \to 4\ell$ Production and HZZ Tensor Coupling with the ATLAS Detector at 13 TeV Centre-of-Mass Energy

von
Verena Maria Walbrecht

28. September 2016

CERN-THESIS-2016-122
18/10/2016

Max-Planck-Institut für Physik
(Werner-Heisenberg-Institut)

Examiner: Priv.-Doz. Dr. H. Kroha
Co-examiner: Prof. Dr. L. Oberauer

Supervisor: Dr. S. Kortner

I assure the single handed composition of this master's thesis is only supported by declared resources.

Ich versichere, dass ich diese Masterarbeit selbstständig verfasst und nur die angegebenen Quellen und Hilfsmittel verwendet habe.

München, September 2016

Unterschrift

Abstract

In this master thesis the measurement of the Higgs boson production in the $H \rightarrow ZZ^* \rightarrow 4\,\ell$ decay channel ($\ell = e, \mu$) is performed together with the measurement of the tensor structure of the Higgs boson couplings to Z bosons. The results are based on the Run II dataset of LHC's proton-proton collisions at a centre-of-mass energy of 13 TeV, with the ATLAS detector and corresponding to a total integrated luminosity of 14.78 fb^{-1}. Special emphasis is given to the estimation of the reducible background contribution. Based on the signal and background estimations, there are 32.0 ± 3.2 Higgs boson candidates expected after the final event selection, while 44 candidates are observed. The difference is compatible at the level of about 2 standard derivations with the Standard Model predictions. All selected candidates are used in the study of the tensor structure of the HZZ coupling between the Higgs boson and the two Z bosons. For this study a dedicated signal model is introduced to describe the signal dependence on the anomalous contribution relative to the Standard Model HZZ coupling. The allowed range of anomalous CP-even and CP-odd coupling parameters has been reduced by a factor of 4 to 10 compared to the constraints from Run I data.

Contents

Chapter 1

Introduction

The Standard Model of particle physics is a quantum field theory describing the electromagnetic, weak and strong interactions between the known elementary particles. Its formulation was introduced in the mid 1970's and has demonstrated ever since an enormous and continuing successes in providing experimental predictions. For a long time the Higgs boson was the last missing particle predicted by the Standard Model. This massive scalar particle is a consequence of the Brout-Englert-Higgs mechanism introduced to explain the origin of elementary particle masses.
In July 2012, the ATLAS and the CMS experiments at the Large Hadron Collider at CERN [1] announced independently the discovery of a new particle with properties compatible with those of the Standard Model Higgs boson [2, 3]. Further measurements of the spin and charge-conjugation and parity (CP) properties of the discovered particle by both experiments [4, 5] confirmed its spin-0 nature and showed that a CP-even state (i.e. positive parity) is strongly preferred. Also the measured couplings to Standard Model particles are compatible with the Standard Model predictions [6].
However, despite of the numerous experimental verifications of the Standard Model predictions, there are several questions left open, such as the unification with gravity, the origin of dark matter and the asymmetry between matter and antimatter in the universe. In this context many theories beyond the Standard Model predict the existence of an extended Higgs sector. In these theories it is still possible, that the Higgs boson is not a pure CP-state, but rather has admixtures of higher-order CP-even or CP-odd contributions [7]. CP-odd contributions to the Higgs boson couplings would lead to CP-violation in the Higgs sector and could help to explain the asymmetry between baryon and anti-baryon content in the universe. By measuring the structure of the tensor coupling of the Higgs boson to vector bosons (HVV), such admixtures could be identified [38].
In this thesis, one of the most sensitive channels for the study of HVV coupling structure is studied - the Higgs boson decay into two Z bosons, which subsequently decay into a pair of oppositely charged leptons, $H \rightarrow ZZ^* \rightarrow 4\,\ell$ ($\ell = e, \mu$). Due to the Higgs boson mass being below the double Z boson mass, one of the Z bosons (Z^*) is produced only as a virtual, off-shell particle.

The present analysis is based on the dataset of proton-proton collisions at a centre-of-mass energy of $\sqrt{s} = 13$ TeV recorded during Run II data taking in 2015 and 2016 with the ATLAS detector. The dataset corresponds to the total integrated luminosity of 14.78 fb^{-1}.
In the first part of this thesis the production of the Higgs boson in the decay channel $H \to ZZ^* \to 4\ell$ is measured. The observed number of events after the full event selection is compared to the signal and background predictions. The signal and the dominant ZZ^* background are estimated from simulation. Dedicated signal-depleted and background-enriched control data is introduced to evaluate the contribution of the reducible background. This background originates from misidentified leptons or leptons from hadron decays. Several control regions are formed with an enhanced contribution of different reducible processes such as Z+jets and $t\bar{t}$ production. The background event yields determined in the control regions are extrapolated to the signal region based on extrapolation factors from simulation. Additional validation data is introduced for additional cross checks of extrapolation factors with data. In this thesis, the extrapolation factors are examined for events with off-shell Z boson decaying into a pair of muons.
In the second part of this thesis a measurement of the structure of the HVV tensor coupling is performed on a sample of Higgs boson candidates selected in the first part. A dedicated signal model is introduced and optimised in order to model the expected number of signal events in dependence on anomalous non-Standard Model coupling parameters with the lowest possible statistical uncertainties. Since the production cross sections in different Higgs boson production modes have different sensitivity to the size of non-Standard Model couplings, the selected Higgs boson candidates are categorised according to their production mode, allowing for more stringent coupling parameter space.

Chapter 2

The Higgs Boson in the Standard Model

2.1 The Standard Model

The Standard Model (SM) [8–11] of particle physics is a well established and extensively tested quantum field theory describing the known particle interactions with the exception of gravity, which is described by the classical field theory of General Relativity [12].
This chapter introduces the SM, with particular emphasis on the Higgs mechanism responsible for the electroweak (EW) symmetry breaking and the origin of elementary particle masses. The Higgs mechanism predicts the existence of a massive scalar particle, the Higgs boson. In 2012, the Higgs boson was discovered with a mass of $m_H = 125$ GeV by both the ATLAS and the CMS experiment [2, 3].

2.1.1 Particle Content of the Standard Model

The SM is a relativistic gauge field theory. In addition to the Higgs boson as the only scalar (spin-0) particle, there are two kinds of elementary particles in the SM - fermions and gauge bosons (see Figure 2.1). The fermions and their antiparticles with the same mass and opposite electric charge have half-integer spin and can be divided into leptons, interacting only electroweakly, and quarks which, in addition, participate in the strong interaction. The six leptons and six quarks are organised in three so-called generations ordered by increasing mass. Each generation contains two leptons, a charged lepton and its corresponding neutrino, and two so-called up- and down-type quarks.
The interactions between the fermions are mediated by spin-1 gauge bosons which correspond to the generators of the gauge symmetries. The gluons mediate the strong interaction, the photon the electromagnetic and the Z^0 and $W^\pm$ bosons the weak interactions. Whereas the gluons and the photon are massless, the weak gauge bosons have mass. The masses of the fermions and the weak gauge bosons are obtained by electroweak symmetry breaking (EWSB) [13, 14], which is discussed in Section 2.2.

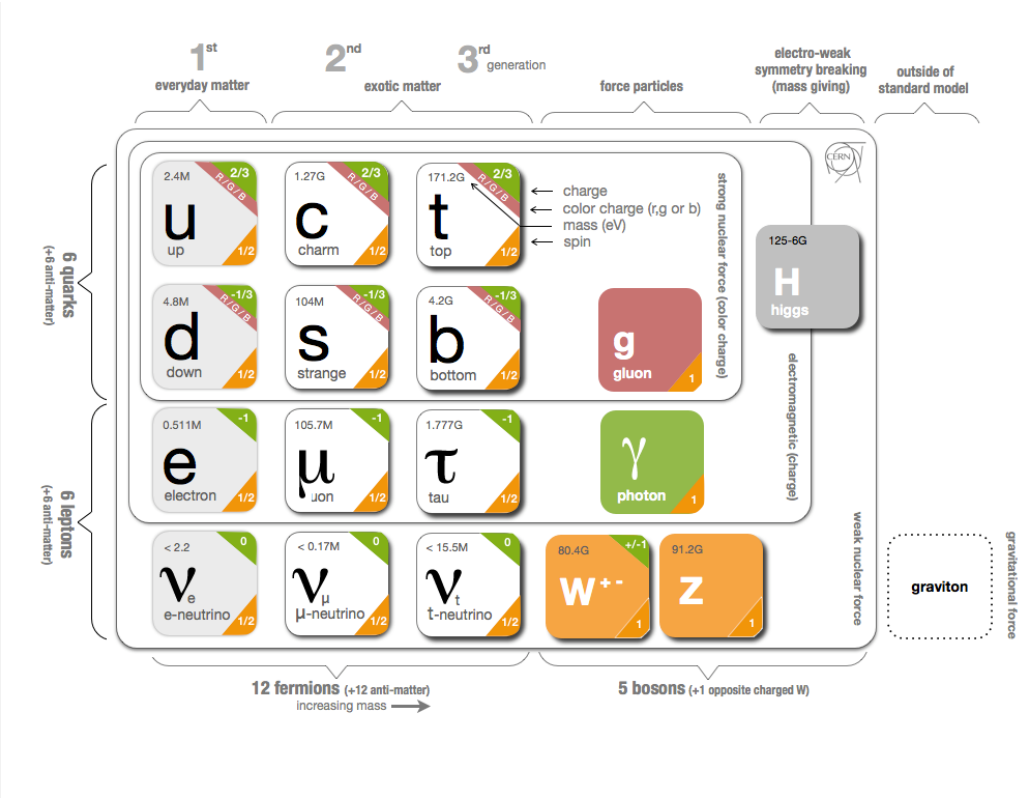

Figure 2.1: Overview of the fundamental particles of the SM [15].

2.1.2 The Electroweak Interaction

In the SM, the electromagnetic and weak interactions are unified in the so-called Glashow-Salam-Weinberg (GSW) theory [16–18]. The weak hypercharge Y_W and the weak isospin vector $\vec{I}$ are the conserved charges of the unified electroweak interaction and the generators of the $U(1)_Y \otimes SU(2)_L$ electroweak gauge symmetry. Experiments showed that only the left-handed helicity state, $\psi_L = P_L\psi$, of the fermions interact with the $SU(2)_L$ gauge bosons, where $P_{L/R} = \left(1 \mp \gamma^5\right)/2$ are the left- and right-handed projection operators and $\psi = P_L\psi + P_R\psi = \psi_L + \psi_R$. Right-handed fermion states are singlets, with the weak isospin charge $|\vec{I}| = 0$. Table 2.1 summarises the electroweak multiplets and their quantum numbers.

Table 2.1: The electroweak multiplets and their quantum numbers: Q is the electric charge, I_3 the third component of the weak isospin and Y_W the weak hypercharge.

	Particle Type			Q	I_3	Y_W
Leptons	$L_L =$	$\left(\begin{pmatrix}\nu_e\\ e\end{pmatrix}_L,\right.$	$\left.\begin{pmatrix}\nu_\mu\\ \mu\end{pmatrix}_L,\right.$	$\left.\begin{pmatrix}\nu_\tau\\ \tau\end{pmatrix}_L\right)$	$\begin{matrix}0\\ -1\end{matrix}$	$\begin{matrix}+1/2\\ -1/2\end{matrix}$	$\begin{matrix}-1\\ -1\end{matrix}$
	$\ell_R =$	$(e_R,$	$\mu_R,$	$\tau_R)$	-1	0	-2
Quarks	$Q_L =$	$\left(\begin{pmatrix}u\\ d\end{pmatrix}_L,\right.$	$\left.\begin{pmatrix}c\\ s\end{pmatrix}_L,\right.$	$\left.\begin{pmatrix}t\\ b\end{pmatrix}_L\right)$	$\begin{matrix}+2/3\\ -1/3\end{matrix}$	$\begin{matrix}+1/2\\ -1/2\end{matrix}$	$\begin{matrix}+1/3\\ +1/3\end{matrix}$
	$u_R =$	$(u_R,$	$c_R,$	$t_R)$	$+2/3$	0	$+4/3$
	$d_R =$	$(d_R,$	$s_R,$	$b_R)$	$-1/3$	0	$-2/3$

The gauge invariant electroweak Lagrangian is given by

$$\begin{aligned}\mathcal{L}_{weak} = &-\frac{1}{2}\mathrm{tr}\{W^{\mu\nu}(x)W_{\mu\nu}(x)\} - \frac{1}{2}B^{\mu\nu}(x)B_{\mu\nu}(x)\\ &+\bar{Q}_L(x)(i\not{D})Q_L(x) + \bar{u}_R(x)(i\not{D})u_R(x) + \bar{d}_R(x)(i\not{D})d_R(x)\\ &+\bar{L}_L(x)(i\not{D})L_L(x) + \bar{\ell}_R(x)(i\not{D})\ell_R(x),\end{aligned} \tag{2.1}$$

with the covariant derivative

$$D_\mu = \mathbb{1}\left[\left(\partial_\mu + ig_1\frac{Y_W}{2}B_\mu(x)\right) + ig_2\vec{I}\cdot\overrightarrow{W_\mu}(x)\right], \tag{2.2}$$

and $\not{D} = \gamma^\mu D_\mu$. $B_\mu(x)$ is the gauge field associated with the Abelian gauge group $U(1)_Y$. $\overrightarrow{W_\mu}(x)$ is associated with $SU(2)_L$. The vector $\vec{I} = \frac{\vec{\tau}}{2} = \frac{1}{2}(\tau_1, \tau_2, \tau_3)$ contains the Pauli matrices τ_i. Moreover, g_1 and g_2 are the coupling constants of the weak hypercharge and of the weak isospin interactions. The gauge field tensors are given by

$$B_{\mu\nu}(x) = \partial_\mu B_\nu(x) - \partial_\nu B_\mu(x) \quad \text{and} \tag{2.3}$$

$$W^i_{\mu\nu}(x) = \partial_\mu W^i_\nu(x) - \partial_\nu W^i_\mu(x) - g_2\epsilon^{ijk}W^j_\mu(x)W^k_\nu(x). \tag{2.4}$$

The totally antisymmetric tensor ϵ^{ijk} is the structure constant of the $SU(2)_L$ Lie algebra.
In contradiction to the experimental observation, the fermions and the weak

gauge bosons in Equation 2.1 are massless. Explicit mass terms for gauge bosons, $-\frac{m^2}{2}A_\mu A^\mu$, would violate the local gauge symmetry and fermion mass terms,

$$-m\bar{\psi}\psi = -m\bar{\psi}\left(P_L^2 + P_R^2\right)\psi = m\left(\bar{\psi}_L\psi_R + \bar{\psi}_R\psi_L\right), \tag{2.5}$$

the global $SU(2)_L$ invariance.
This conflict is solved by the Brout-Englert-Higgs mechanism of EWSB discussed in Section 2.2, where the electroweak $SU(2)_L \otimes U(1)_Y$ gauge symmetry is spontaneously broken to the electromagnetic gauge group $U(1)_Q$ with the charge operator Q as generator, which is a linear combination of the weak isospin I_3 and the hypercharge Y_W:

$$Q = I_3 + \frac{Y_W}{2}. \tag{2.6}$$

2.2 The Higgs Mechanism

The Brout-Englert-Higgs mechanism of EWSB [13, 14, 19–23] introduces a spin-0 field, called the Higgs field. It is a complex $SU(2)_L$ doublet

$$\Phi = \begin{pmatrix} \phi^+ \\ \phi^0 \end{pmatrix} \tag{2.7}$$

and colour singlet with hypercharge $Y_W = 1$. The fermions and weak gauge bosons acquire their mass trough interaction with this field. The Lagrangian for the scalar Higgs field is given by

$$\mathcal{L}_{scalar} = (D_\mu\Phi)^\dagger(D^\mu\Phi) - V(\Phi), \tag{2.8}$$

with the electroweak covariant derivative as in Equation 2.2 . Renormalisability [24–26] and gauge invariance demand that the potential of the Higgs field is of the form

$$V(\Phi) = \mu^2\Phi^\dagger\Phi + \lambda(\Phi^\dagger\Phi)^2, \tag{2.9}$$

where λ is the dimensionless self-coupling and μ^2 a mass parameter. Vacuum stability requires λ to be larger than zero. For the mass parameter $\mu^2 > 0$, the potential has its minimum at $|\Phi_0^2| = 0$ and the vacuum state of the theory obeys the same gauge symmetries as the Lagrangian. For $\mu^2 < 0$, the scalar field achieve a non-vanishing vacuum expectation value $v \equiv \sqrt{\frac{-\mu^2}{\lambda}}$. Due to electric charge conservation only the neutral scalar field component can acquire a finite vacuum expectation value. The ground state, therefore, can be chosen as

$$\langle\Phi\rangle_0 = \frac{1}{\sqrt{2}}\begin{pmatrix} 0 \\ v \end{pmatrix}. \tag{2.10}$$

This particular choice of the vacuum expectation state breaks the $SU(2)_L \otimes U(1)_Y$ gauge symmetry spontaneously. Invariance under the $U(1)_Q$ symmetry is still preserved:

$$Q \langle \Phi \rangle_0 = \left(I_3 + \frac{Y_W}{2} \right) \langle \Phi \rangle_0 = 0. \tag{2.11}$$

Three degrees-of-freedom of the Higgs field are absorbed in the longitudinal polarisation of the weak gauge bosons, which in this way acquire their mass. In the unitary gauge, the scalar field $\Phi(x)$ can be parametrised as

$$\Phi = \frac{1}{\sqrt{2}} \begin{pmatrix} 0 \\ v + h(x) \end{pmatrix}, \tag{2.12}$$

with the scalar Higgs field $h(x)$ as massive radial excitation from the new ground state $\langle \Phi \rangle_0$. By inserting the expansion (Equation 2.12) into $\mathcal{L}_{scalar}$ one obtains

$$\begin{aligned} \mathcal{L}_{scalar} = & \frac{1}{2} \partial_\mu h(x) \partial^\mu h(x) - \lambda v^2 h^2(x) - \lambda v h^3(x) - \frac{\lambda}{v} h^4(x) \\ & + \frac{g_2^2 \left(2vh(x) + h^2(x) \right)}{4} \left(W_\mu^+(x) W^{-\mu}(x) + \frac{1}{2 \cos^2 \theta_W} Z_\mu(x) Z^\mu(x) \right) \\ & + \frac{g_2^2 v^2}{8} \left(W_\mu^+(x) W^{+\mu}(x) + W_\mu^-(x) W^{-\mu}(x) \right) + \frac{g_2^2 v^2}{4 \cos^2 \theta_W} Z_\mu(x) Z^\mu(x). \end{aligned} \tag{2.13}$$

The charged gauge fields $W_\mu^\pm$ are the linear combinations of the W_μ^1 and W_μ^2 fields:

$$W_\mu^\pm = \frac{1}{\sqrt{2}} \left(W_\mu^1 \mp i W_\mu^2 \right). \tag{2.14}$$

The mass eigenstates Z_μ and A_μ of the neutral weak gauge fields are obtained by a rotation

$$Z_\mu = \frac{-g_1 B_\mu + g_2 W_\mu^3}{\sqrt{g_1^2 + g_2^2}} \quad \text{and} \quad A_\mu = \frac{g_1 B_\mu + g_2 W_\mu^3}{\sqrt{g_1^2 + g_2^2}} \tag{2.15}$$

with the Weinberg angle θ_W and

$$\sin \theta_W = \frac{g_1}{\sqrt{g_1^2 + g_2^2}} = \frac{e}{g_2}, \tag{2.16}$$

where e is the elementary charge, the coupling constant of the electromagnetic interactions.
According to the Equation 2.13 the masses of the three massive gauge bosons and of

the Higgs boson are given by [27]

$$\begin{aligned} m_{W^\pm} &= \frac{g_2 v}{2} = 80.385 \pm 0.015 \text{ GeV}, \\ m_Z &= \frac{g_2 v}{2\cos\theta_W} = \frac{m_{W^\pm}}{\cos\theta_W} = 91.1876 \pm 0.0021 \text{ GeV} \quad \text{and} \\ m_h &= v\sqrt{2\lambda} = 125.09 \pm 0.24 \text{ GeV}. \end{aligned} \tag{2.17}$$

The masses of the fermions are obtained by introducing a Yukawa interaction between the scalar Higgs field and fermionic matter fields with Yukawa couplings [28] Y_f of the form

$$\mathcal{L}_{Yukawa} = -Y_f \left(\bar{\psi}_L \Phi \psi_R + \bar{\psi}_R \left(i\frac{\tau_2}{2}\Phi \right) \psi_L \right). \tag{2.18}$$

For the first generation of leptons, for example, the Yukawa couplings are

$$\mathcal{L}_{Yukawa} = -Y_e \left((\bar{\nu}_e, e)_L \Phi e_R + \bar{e}_R \left(i\frac{\tau_2}{2}\Phi \right) \begin{pmatrix} \nu_e \\ e \end{pmatrix}_L \right), \tag{2.19}$$

which after electroweak symmetry breaking (Equation 2.12) become

$$\mathcal{L}_{Yukawa} = -Y_e \frac{v + h(x)}{\sqrt{2}} \left(\bar{e}_L e_R + \bar{e}_R e_L \right). \tag{2.20}$$

Terms of that form occur for all SM fermions. Hence the masses of the fermions are given by

$$m_f = Y_f \frac{v}{\sqrt{2}}. \tag{2.21}$$

However, the mass eigenstates of the quarks differ from their electroweak $SU(2)_L$ eigenstates and are obtained by bi-unitary transformations which diagonalize the mass matrices $m_{ij}^u = Y_{ij}^u \frac{v}{\sqrt{2}}$ and $m_{ij}^d = Y_{ij}^d \frac{v}{\sqrt{2}}$:

$$\mathcal{V}_{u_L}^\dagger m_u \mathcal{V}_{u_R} = \text{diag}\left(m_u, m_c, m_t\right) \quad \text{and} \quad \mathcal{V}_{d_L}^\dagger m_d \mathcal{V}_{d_R} = \text{diag}\left(m_d, m_s, m_b\right). \tag{2.22}$$

The mass eigenstates m_f are proportional to the Yukawa couplings Y_f. The product of $\mathcal{V}_{u_L}^\dagger$ and $\mathcal{V}_{d_L}$ defines the unitary Cabibbo-Kobayashi-Maskawa (CKM) quark flavour mixing matrix [29, 30]

$$\mathcal{V}_{u_L}^\dagger \mathcal{V}_{d_L} \equiv V_{CKM}, \tag{2.23}$$

which leads to weak charged current transitions of the three generations of quark mass eigenstates. The elements of the CKM matrix determine the probabilities of the charged current transitions. In the SM, the unitary 3-dimensional CKM matrix is determined by three mixing angles and one complex phase, which is the source of CP violation in the SM.

Chapter 3

The Higgs Boson at the Large Hadron Collider

3.1 Proton-Proton Collisions at the Large Hadron Collider

At the Large Hadron Collider (LHC) [1], described in Chapter 4, protons collide at centre-of-mass energies of up to 14 TeV. During 2010 and 2011, the LHC operated at a centre-of-mass energy of $\sqrt{s} = 7$ TeV and in 2012 of 8 TeV. This period marks the so-called Run I of the LHC. In 2015 the Run II of the LHC started with proton-proton (pp) collisions at a centre-of-mass energy of $\sqrt{s} = 13$ TeV.
As the proton is not an elementary particle, but a bound state of strongly interacting partons - valence quarks (uud), gluons and sea quarks ($\bar{q}q$) -, the interactions between the colliding protons have to be described as a superposition of partons with momentum fraction x carried by a parton relative to the total momentum p of the proton.
Scattering processes in pp collisions can be divided into soft and hard interactions. Hard interactions are characterised by high momentum transfer, Q^2, allowing for the production of heavy resonances such as the Higgs boson. These can be described perturbatively with high precision. On the other hand, the low momentum transfer of soft interactions leads to final state radiation of additional quarks or gluons which subsequently fragment into hadrons. Due to the low energy scale, such QCD processes cannot be described perturbatively. An illustration of a hadronic interaction including both hard and soft processes is shown in Figure 3.1.
Considering two partons a and b in each of the colliding protons (p_A and p_B), the production cross section $\sigma_{p_A+p_B\to H+X}$ for Higgs boson production together with additional hadronic particles X is given by

$$\sigma_{p_A+p_B\to H+X} = \int \mathrm{d}x_a \mathrm{d}x_b \; f_{a/A}(x_a, \mu_F^2) f_{b/B}(x_b, \mu_F^2) \hat{\sigma}_{ab\to H}(\mu_F^2, \mu_R^2). \tag{3.1}$$

According to the factorisation theorem [32], $\hat{\sigma}_{ab\to H}(\mu_F^2, \mu_R^2)$ is the hard-scatter parton cross section which can be calculated perturbatively. Here μ_R is the renormalisation scale of the running strong coupling and μ_F the factorisation scale. The cross

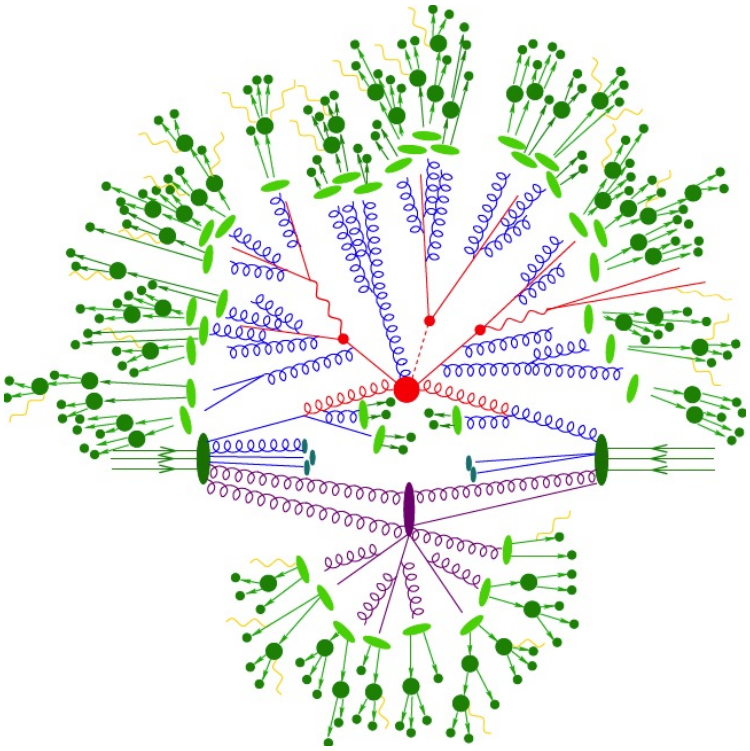

Figure 3.1: Illustration of a proton-proton collision at high energies [31]. The hard scattering of partons is shown in red, Bremsstrahlung processes produced in parton showers in blue, hadronizing partons in green and secondary soft interactions in purple. Moreover, hadron decays are shown in dark green and QED Bremsstrahlung in yellow.

section depends on the two parton distribution functions (PDFs), $f_{a/A}(x_a, \mu_F^2)$ and $f_{b/B}(x_b, \mu_F^2)$, which are the probability densities for finding a parton $i = a, b$ with momentum fraction x_i in proton $j = A, B$ at a given μ_F^2. The PDFs are not predicted in perturbative QCD, but can be measured in dedicated experiments at an arbitrary hadronization scale μ_0 and then extrapolated to the scale μ_F using the DGLAP equation [33, 34].

3.2 Standard Model Higgs Boson Production

The Higgs boson mass m_H is not predicted by the SM. For given Higgs boson mass, the production cross sections of all production modes, as well as the decay rates to fermions and vector bosons and the total decay width are fully determined [35].

The four main mechanisms for the SM Higgs boson production at the LHC, shown in Figure 3.2, are gluon-fusion (ggF), vector boson fusion (VBF), associated production with vector bosons $V = W, Z$ (VH) and with heavy quarks ($t\bar{t}H/b\bar{b}H$) [35].

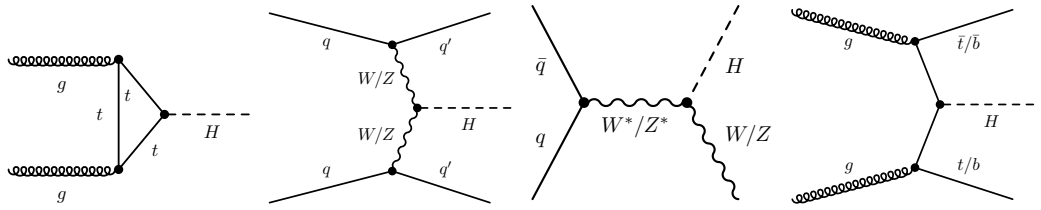

(a) (b) (c) (d)

Figure 3.2: Tree-level Feynman diagrams for the main SM Higgs boson production mechanisms at the LHC: (a) gluon-fusion, (b) vector boson fusion, (c) associated production with vector bosons and (d) associated production with heavy quarks [35].

The production cross sections for a SM Higgs boson with mass $m_H = 125$ GeV are shown in Figure 3.3 for the main production modes as a function of the centre-of-mass energy $\sqrt{s}$. The production cross sections at a centre-of-mass energy of $\sqrt{s} = 13$ TeV are summarised in Table 3.1. In all production modes the production cross section increases the centre-of-mass energy.

Table 3.1: Production cross sections for the dominant production modes of the SM Higgs boson with a mass of $m_H = 125$ GeV at the LHC at a centre-of-mass energy of $\sqrt{s} = 13$ TeV [36].

Production mode	Production mechanism	Cross section [pb]
ggF	$pp \to H$	$48.64^{+6.8\%}_{-6.7\%}$
VBF	$pp \to qqH$	$3.782^{+2.2\%}_{-2.2\%}$
VH	$pp \to W^* \to WH$	$1.373^{+2.0\%}_{-2.0\%}$
	$pp \to Z^* \to ZH$	$0.884^{+4.1\%}_{-3.5\%}$
$t\bar{t}H$	$pp \to t\bar{t}H$	$0.507^{+6.8\%}_{-9.9\%}$
$b\bar{b}H$	$pp \to b\bar{b}H$	$0.488^{+20.2\%}_{-23.9\%}$

The dominant production mechanism is the gluon-fusion via an intermediate quark loop (see Figure 3.2(a)). Due to the mass dependence of the Higgs boson coupling to the quarks (Section 2.2), the top-quark loop gives the largest contribution.

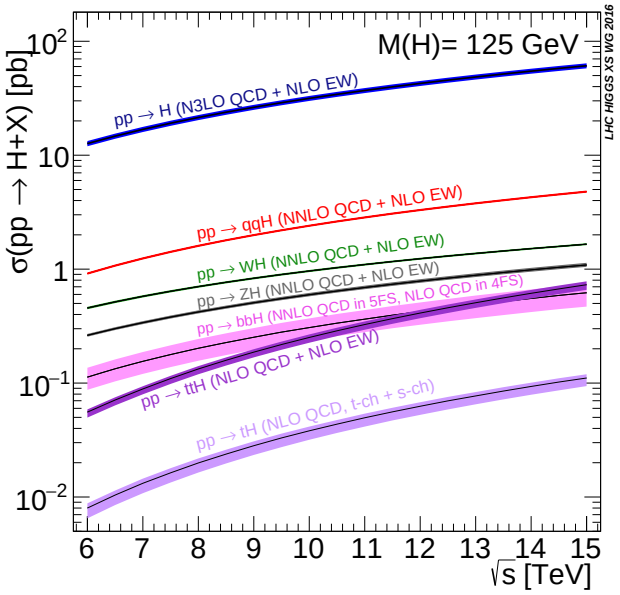

Figure 3.3: SM production cross sections for the main Higgs boson production modes in proton-proton collisions as a function of the centre-of-mass energy for a Higgs boson mass of $m_H = 125$ GeV [36].

The production mode with the second-largest cross section is the vector boson fusion (Figure 3.2(b)), where the Higgs boson is produced in the scattering of two weak gauge bosons emitted from scattered quarks which can be detected as two high-energy jets in the forward regions of the detector, providing powerful discrimination of the Higgs boson signal against the QCD background.
The third strongest Higgs boson production mechanism of the LHC is in association with gauge bosons as shown in Figure 3.2(c). A virtual W or Z boson is created via quark-antiquark annihilation which emits a Higgs boson together with a real weak boson in the final state.
Higgs boson production in association with heavy quarks (see Figure 3.2(d)) has an even smaller cross section. The Higgs boson production in the fusion of top- antitop quark pairs is a direct probe of the top-Higgs Yukawa coupling. Furthermore, the weak bosons and the top-quarks produced in the VH and $t\bar{t}H$ production modes help in the detection of $H \to b\bar{b}$ decays, which otherwise is not feasible due to the large QCD background.

3.3 Higgs Boson Decay Modes

The total decay width and the branching ratios (BR) of the SM Higgs boson are shown in Figure 3.4 as a function of the Higgs boson mass m_H.

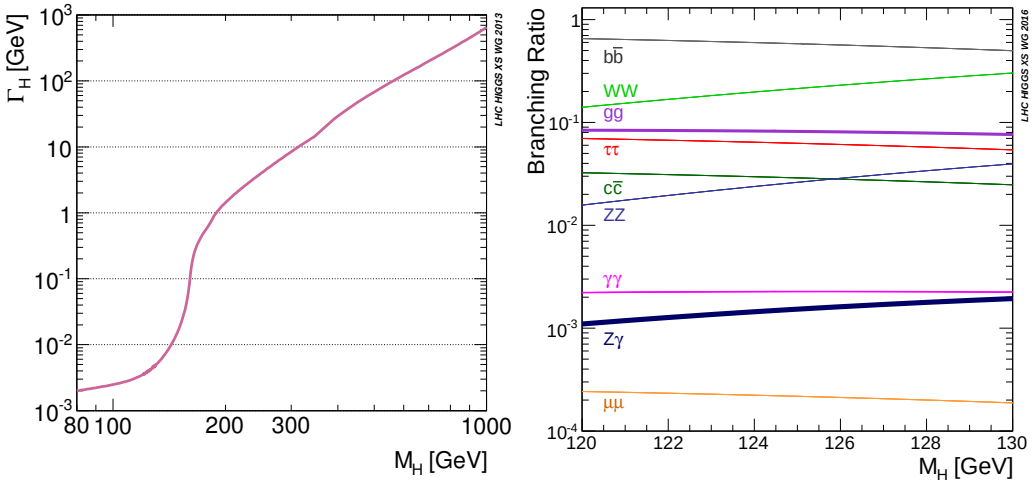

(a) (b)

Figure 3.4: (a) Total decay width and (b) branching ratios of the SM Higgs boson decay as a function of the Higgs boson mass m_H [36].

The total decay width of a mass of $m_H = 125$ GeV is approximately 4 MeV, too small to be measured directly due to the limited mass resolution of the detector. The Higgs boson is detected via its decay products. Since the couplings of the Higgs boson to fermions and gauge bosons are proportional to their masses, the Higgs boson decays preferentially into the heaviest particles allowed by energy conservation.

At a mass of 125 GeV, the Higgs boson decays most frequently into pairs of bottom quarks, W bosons, gluons and τ leptons, followed by $c\bar{c}$, ZZ and $\gamma\gamma$ pairs. The Feynman diagrams for the SM Higgs boson decays into fermions, W/Z bosons and photons are shown in Figure 3.5. Since photons and gluons are massless particles, they do not couple directly to the Higgs boson. The decay into these particles is only possible via loop processes involving mainly heavy quarks or W bosons.
Due to the large background contributions, in particular in the fully hadronic final states, not all of these decay channels can be detected. The largest sensitivity is reached in final states with electrons (e), muons (μ) or photons (γ), such as in $H \to \gamma\gamma$ or $H \to 4\ell$ decays ($\ell = e, \mu$) .

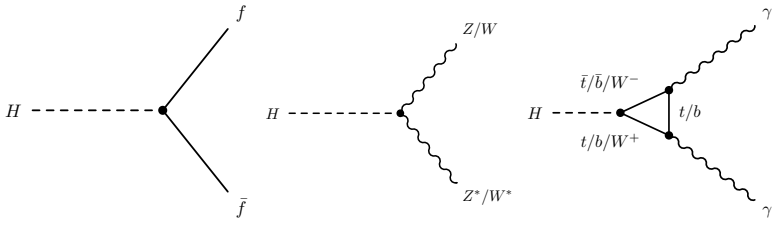

(a) (b) (c)

Figure 3.5: Feynman diagrams of the SM Higgs boson decays into (a) two fermions, (b) two vector bosons and (c) via a fermion or W loop process, two photons [35].

3.4 Spin and CP Properties of the Higgs Boson

The CP symmetry is invariance under the combination of charge conjugation (C) and parity (P) transformation [37]. According to spin (J) and behaviour under the CP transformation, particles can be categorised as scalars, pseudo-scalars, vectors or pseudo-vectors. As an example, J^{CP} quantum numbers are shown in Table 3.2 for several particles.

Table 3.2: Spin and CP quantum numbers J^{CP} for various particles in the SM.

Conjugation	scalar	pseudo-scalar	vector	pseudo-vector
Spin: J	0	0	1	1
Charge: C	$+1$	$+1$	$+1$	$+1$
Parity: P	$+1$	-1	-1	$+1$
J^{CP}	0^{++}	0^{+-}	1^{+-}	1^{++}
Example	SM Higgs boson	π, K, η, η'	Z, W, γ, g	pseudo-vector mesons

As charge conjugation is conserved for neutral particles such as the Higgs boson, the spin and CP quantum number is labelled as J^P in the following.
In the SM the Higgs boson is a CP-even scalar particle, $J^P = 0^+$. In contrast to the electroweak sector (Section 2.1.2) the CP quantum number in the Higgs sector is conserved. For example in the $H \to ZZ$ decay, both the Higgs boson and the two Z bosons, are even eigenstates under CP transformations,

$$CP\,|H\rangle = +1\,|H\rangle \quad \text{and} \quad CP\,|ZZ\rangle = +1\,|ZZ\rangle\,. \tag{3.2}$$

After the discovery of a Higgs-like boson by the ATLAS and CMS experiments [2, 3] its spin and CP quantum numbers have been probed [4, 5, 38]. The results of these studies, presented in Section 3.6, indicate the compatibility with the SM prediction. However, theories Beyond the Standard Model (BSM) allow for possible small admixtures of higher-order non-SM CP-even or CP-odd contributions to the SM CP-even state [7]. The observed Higgs boson would in that case be a mass eigenstate but no longer a CP-eigenstate. The presence of CP-odd contributions, for example, would lead to CP-violation in the Higgs sector, possibly related to the baryon-antibaryon asymmetry in the universe.
The CP-nature of the discovered boson is investigated by measuring the tensor structure of the Higgs boson coupling to the SM particles such as vector bosons $V = W, Z$. The tensor structure of the HVV interaction can be studied in kinematic distributions of the Higgs boson production and decay products, as well as in the relative production rates via different production modes [39]. Theoretical description of the HVV tensor structure with non-SM contributions is described in the following section, under the assumption of a spin-0 Higgs boson, as indicated by the latest measurements.

3.5 The Higgs Characterisation Model

The HVV interaction between the Higgs boson and heavy vector bosons including the SM and higher-order CP-even and CP-odd BSM contributions is described in terms of an effective field theory (EFT). In this approach, the mass of the interaction mediator, related to the energy scale Λ at which new physics appears, is assumed to be much larger than the interaction energy E, $E \ll \Lambda$. Thus, a point HVV interaction can be assumed.
Within the so-called Higgs characterisation (HC) EFT model [40] the HVV interactions are described in terms of effective couplings, with the following effective Lagrangian for a spin-0 Higgs boson:

$$\begin{aligned}\mathcal{L}_0^V = &\Bigg\{ \cos(\alpha)\,\kappa_{SM}\left[\frac{1}{2}g_{HZZ}Z_\mu Z^\mu + g_{HWW}W_\mu^+ W^{-\mu}\right] \\ &- \frac{1}{4}\frac{1}{\Lambda}\left[\cos(\alpha)\,\kappa_{HZZ}Z_{\mu\nu}Z^{\mu\nu} + \sin(\alpha)\,\kappa_{AZZ}Z_{\mu\nu}\tilde{Z}^{\mu\nu}\right] \\ &- \frac{1}{2}\frac{1}{\Lambda}\left[\cos(\alpha)\,\kappa_{HWW}W_{\mu\nu}^+ W^{-\mu\nu} + \sin(\alpha)\,\kappa_{AWW}W_{\mu\nu}^+ \tilde{W}^{-\mu\nu}\right]\Bigg\}\mathcal{X}_0,\end{aligned} \tag{3.3}$$

with the vector boson fields $V^\mu = Z^\mu, W^\mu$, the reduced field tensors $V^{\mu\nu}$ and the dual tensors defined as $\tilde{V}^{\mu\nu} = \frac{1}{2}\epsilon^{\mu\nu\rho\sigma}V_{\rho\sigma}$. The effective HC coupling parameters κ_{SM}, κ_{HVV} and κ_{AVV} describe respectively the SM, BSM CP-even and CP-odd interaction of the VV (ZZ and WW) pairs with the spin-0 field $\mathcal{X}_0$. In order for the Lagrangian

terms to be hermitian, the HC coupling parameters have to be real. The SM coupling of the Higgs boson to vector bosons is denoted as g_{HVV}. Mixing angle α allows for the CP-mixing and implies CP-violation if $\alpha \neq 0$ and $\alpha \neq \pi$. The EFT scale Λ denotes, the energy scale up to which the model is valid. In present studies Λ is set to 1 TeV, since current experimental results show no evidence for new physics up to this scale. The Lagrangian described in Ref. [40] includes additional operators for gg, $\gamma\gamma$ and $Z\gamma$ interactions. These are neglected in the presented analysis, since no sensitivity to this interactions is expected with the current data.
The HC model assumes that the observed resonance at 125 GeV is a scalar particle with a decay width much smaller than the resolution of the ATLAS detector. Furthermore it is assumed that any additional BSM particles would exist only above the scale Λ.
Summary of the HC parameter settings for the SM Higgs boson ($J^P = 0^+$), a pure higher-order CP-even ($J^P = 0_h^+$) and CP-odd ($J^P = 0^-$) state is given in Table 3.3.

Table 3.3: HC-model parameters for different parity states of a spin-0 particle [38].

J^P	Description	Values of HC-model parameters			
		κ_{SM}	κ_{HVV}	κ_{AVV}	α
0^+	SM Higgs boson	1	0	0	0
0_h^+	BSM spin-0 CP-even	0	1	0	0
0^-	BSM spin-0 CP-odd	0	0	1	$\pi/2$

3.6 Status of Higgs Boson Property Measurements

In July 2012, the ATLAS and CMS collaborations independently announced the discovery of a new particle with a mass of approximately 125 GeV with properties consistent with those of a SM Higgs boson [2, 3]. Further dedicated measurements of the Higgs boson couplings to SM particles as well as the study of its spin and CP quantum numbers confirm the compatibility with SM predictions [4–6, 38]. In the following the combined results of the ATLAS and CMS coupling measurements are presented. Also the results of ATLAS spin and parity studies are shown [4, 38]. Similar results are also obtained by the CMS collaboration [41, 42]. The results are obtained with the pp dataset recorded during Run I and corresponding to an integrated luminosity of 4.6 fb^{-1} at a centre-of-mass energy of 7 TeV in 2011 and 20.7 fb^{-1} at 8 TeV in 2012.

The mass of the discovered Higgs boson has been measured in the $H \to \gamma\gamma$ and $H \to ZZ^* \to 4\ell$ decay channels [43]. These are the only two high-sensitive channels allowing for a precise full reconstruction of the invariant mass of the Higgs boson decay products. The combined measurement of ATLAS and CMS experiments results in a Higgs boson mass of

$$m_H = 125.09 \pm 0.21(\text{stat.}) \pm 0.11(\text{sys.}) \text{ GeV}. \tag{3.4}$$

In order to study the Higgs boson couplings to SM particles, different combinations of Higgs boson production and decay modes have been studied. The product of the production cross section and the branching ratio, $\sigma_i \cdot B^f$, has been measured for individual processes $i \to H \to f$, where i denotes the production mechanism (ggF, VBF, WH, ZH and $\bar{\text{t}}\text{tH}$) and f the main Higgs boson decay mode [6]. The ggF and VBF production modes have not been probed in case of $H \to bb$ decays due to a large multijet background contribution. Due to a very small expected number of events for the ZH, WH and $\bar{\text{t}}\text{tH}$ production in case of $H \to ZZ$ decays, $\sigma_i \cdot B^f$ has not been measured for these processes. The measured $\sigma_i \cdot B^f$ values, normalised to the SM prediction for a Higgs boson with a mass of 125.09 GeV, are shown in Figure 3.6. Within the experimental and theoretical uncertainties, all measurements of $\sigma_i \cdot B^f$ are consistent with the SM prediction.
The product $\sigma_i \cdot B^f$ can be related to the couplings of the Higgs boson to the corresponding fermions or vector bosons [6]. The coupling modifier κ_j is defined as

$$\kappa_j^2 = \frac{\sigma_j}{\sigma_j^{SM}} \quad \text{or} \quad \kappa_j^2 = \frac{\Gamma_j}{\Gamma_j^{SM}}. \tag{3.5}$$

In the SM, all κ_j values equal unity. The coupling modifiers are obtained from the combined fit of expected to all measured $\sigma_i \cdot B^f$ values. In order to illustrate the dependence of the Higgs boson couplings on the particle mass a redefined set of parameters can be used, linear in Yukawa coupling for fermions and quadratic for the gauge coupling to the weak bosons. For fermions with mass m_F the new parameters are $\kappa_F \frac{y_F}{\sqrt{2}} = \kappa_F \frac{m_F}{v}$, where y_F is the Yukawa coupling strength and $v = 246$ GeV the vacuum expectation value of the Higgs field. For the weak bosons with mass m_V the new parameters are $\sqrt{\kappa_V \frac{g_V}{2v}} = \sqrt{\kappa_V} \frac{m_V}{v}$, where g_V is the absolute Higgs boson gauge coupling strength. The measured dependence of these new parameters on the particle mass is shown in Figure 3.7. The measured coupling parameters are in a good agreement with the SM prediction.

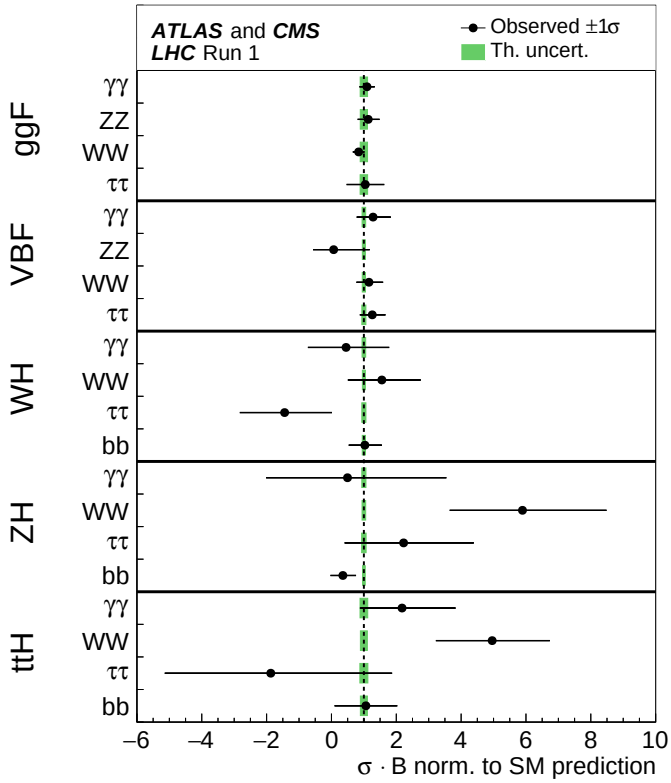

Figure 3.6: Combined ATLAS and CMS measurement of the products of Higgs boson production cross section and branching ratio, $\sigma_i \cdot B^f$, for different combinations of Higgs boson production (i) and decay modes (f) normalised to the corresponding SM prediction. The results are based on the Run I dataset with an integrated luminosity of 4.6 fb^{-1} at a centre-of-mass energy of 7 TeV and 20.7 fb^{-1} at 8 TeV [6].

The spin and parity properties of the discovered Higgs boson have been studied using the Higgs boson decays $H \to \gamma\gamma$, $H \to ZZ^* \to 4\ell$ and $H \to WW^* \to \ell\nu\ell\nu$ [38]. The SM $J^P = 0^+$ hypothesis has been compared with several alternative hypotheses, namely $J^P = 0^-, 1^+, 1^-, 2^+_m$. The $J^P = 2^+_m$ hypothesis is based on a graviton model [44]. Figure 3.8 shows the expected and observed confidence level values CL_s [45] for the different spin-parity hypotheses. All alternative hypotheses are excluded at 99.9% confidence level. The quantum number predicted by the SM, $J^P = 0^+$, is favoured by the data.
In addition to the tests of pure CP-state hypotheses the search was also performed for possible small admixtures of higher-order CP-even or CP-odd states to the dominant SM CP-even state, as described in Section 3.4. The ratio of the HC coupling para-

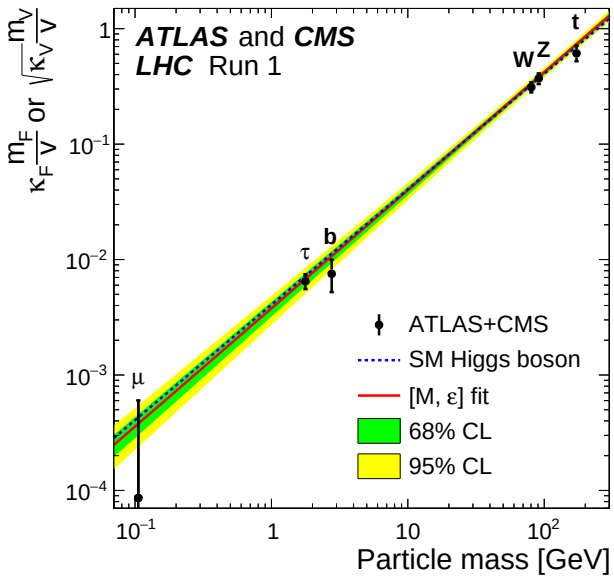

Figure 3.7: Coupling parameters $\kappa_F \frac{m_F}{v}$ and $\sqrt{\kappa_V}\frac{m_V}{v}$ from the combined fit to ATLAS and CMS data, shown as a function of particle mass (m_F, m_V). The SM prediction is shown as the dashed blue line with corresponding uncertainties in a green and yellow band. The results are based on the Run I dataset with an integrated luminosity of 4.6 fb^{-1} at a centre-of-mass energy of 7 TeV and 20.7 fb^{-1} at 8 TeV [6].

meters (Section 3.5), $(\tilde{\kappa}_{AVV}/\kappa_{SM}) \cdot \tan(\alpha)$ and $\tilde{\kappa}_{HVV}/\kappa_{SM}$, where $\tilde{\kappa}_{XVV} = \frac{1}{4}\frac{v}{\Lambda}\kappa_{XVV}$, has been measured in $H \to ZZ^* \to 4\ell$ and $H \to WW \to \ell\nu\ell\nu$ decays [38]. The measurement was based on the shape of the CP-sensitive kinematic distributions of the Higgs boson decay products. The expected and observed values of coupling parameters excluded at a 95% confidence level after combination of both decay channels are given in Table 3.4.

Table 3.4: Expected and observed best-fit values and exclusion regions at 95% confidence level for the higher-order BSM CP-odd and CP-even coupling parameters, $(\tilde{\kappa}_{AVV}/\kappa_{SM}) \cdot \tan(\alpha)$ and $\tilde{\kappa}_{HVV}/\kappa_{SM}$, respectively. Results are obtained from the combined analysis of the $H \to ZZ^* \to 4\ell$ and $H \to WW^* \to \ell\nu\ell\nu$ decay channels [38].

Coupling ratio	Best-fit value	95% CL Exclusion regions	
combined	Observed	Expected	Observed
$(\tilde{\kappa}_{AVV}/\kappa_{SM}) \cdot \tan(\alpha)$	-0.68	$(-\infty, -2.33] \bigcup [2.30, \infty)$	$(-\infty, -2.18] \bigcup [0.83, \infty)$
$\tilde{\kappa}_{HVV}/\kappa_{SM}$	-0.48	$(-\infty, -0.55] \bigcup [4.80, \infty)$	$(-\infty, -0.73] \bigcup [0.63, \infty)$

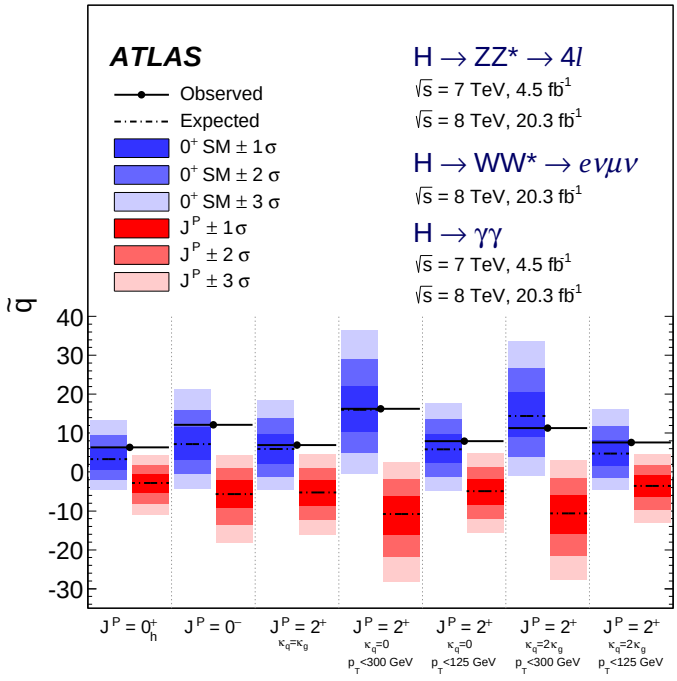

Figure 3.8: Confidence levels, CL_s, for all alternative spin-parity hypotheses ($J^P = 0^-, 1^+, 1^-, 2^+_m$) tested against the SM hypotheses $J^P = 0^+$. The results are based on the Run I dataset with an integrated luminosity of 4.6 fb^{-1} at a centre-of-mass energy of 7 TeV and 20.7 fb^{-1} at 8 TeV [38].

For the CP-odd coupling parameter the best fit value is $(\tilde{\kappa}_{AVV}/\kappa_{SM}) \cdot \tan(\alpha) = -0.68$ and the region outside $-2.18 < (\tilde{\kappa}_{AVV}/\kappa_{SM}) \cdot \tan(\alpha) < 0.83$ is excluded at 95% confidence level. For the CP-even coupling parameter the best fit value is $\tilde{\kappa}_{HVV}/\kappa_{SM} = -0.48$ and the region outside $-0.73 < \tilde{\kappa}_{HVV}/\kappa_{SM} < 0.63$ is excluded at 95% confidence level. All results are consistent with the SM prediction.

Chapter 4

The ATLAS Detector at the Large Hadron Collider

4.1 The Large Hadron Collider

The Large Hadron Collider (LHC) [1] is a circular proton and heavy ion accelerator and collider situated at the European Organization for Nuclear Research (CERN). It is hosted in a tunnel with a 27 km circumference 170 m below the ground. The particle beams circulate in opposite direction in two separate beam pipes in an ultra-high vacuum. A strong magnetic field of 8.33 T maintained by superconducting electromagnets bends the two particle beams along the accelerator ring. The LHC is designed to collide protons at a centre-of-mass energy of up to 14 TeV. During 2010 and 2011 the proton-proton (pp) collision data were taken at a centre-of-mass energy of 7 TeV, increasing to 8 TeV in 2012. This data taking period marks the so-called Run I of the LHC. After a subsequent collider shut down for maintenance and upgrades, the Run II of the LHC started in 2015 with proton-proton collisions at a centre-of-mass energy of 13 TeV.
Before the colliding protons are injected into the LHC they transverse a chain of pre-accelerators shown in Figure 4.1. First the hydrogen atoms with stripped off valence electron are accelerated in the Linear accelerator 2 (LINAC2) up to 50 MeV and are injected afterwards into the Proton Synchrotron Booster (PSB). This first circular pre-accelerator increases the energy of the protons up to 1.4 GeV. After that the protons are accelerated to 25 GeV in the Proton Synchrotron (PS) and then injected into the Super Proton Synchrotron (SPS), where they are accelerated up to 450 GeV and then piped to the LHC. At the LHC the protons are further accelerated to their maximum achievable energy and are then collided at one of the four interaction points, at which the four main LHC experiments are hosted, the ATLAS, CMS, ALICE and LHCb experiment.
The general purpose experiments, ATLAS and CMS, are designed for broad search for new physics, such as the search for the Higgs boson, dark matter, supersymmetry or extra dimensions, as well as for precision tests of the SM predictions. The heavy-ion detector ALICE studies the physics of strongly interacting matter at

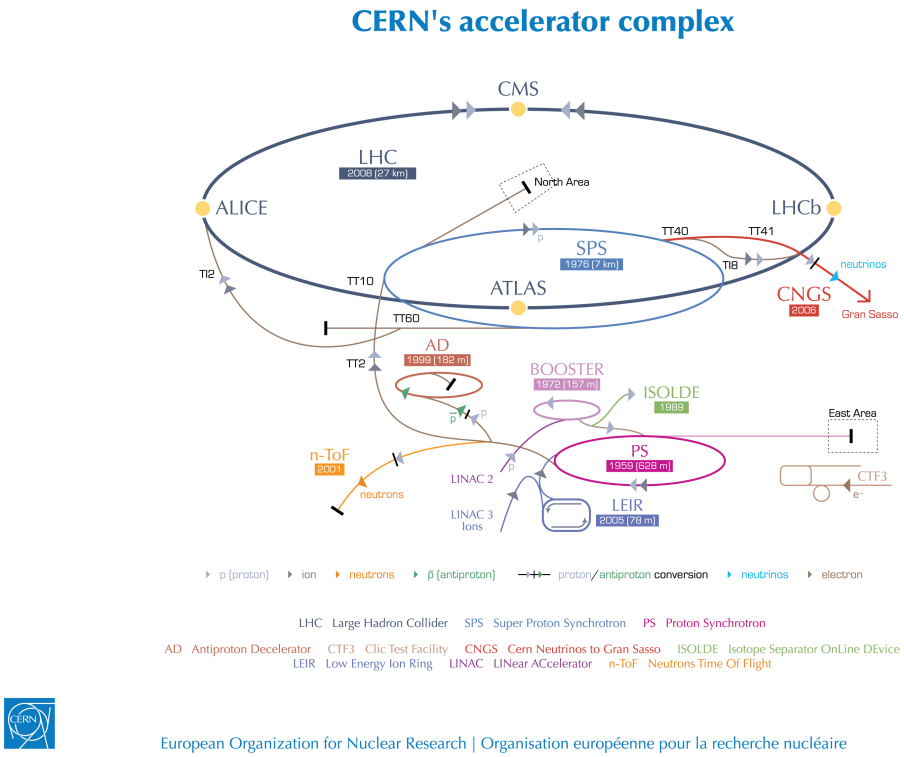

Figure 4.1: The CERN accelerator complex [46]. The illustration shows the injection chain traversed by protons colliding in the LHC.

extreme energy densities, the so-called quark-gluon plasma. As opposed to these experiments, the LHCb experiment is designed to detect particles mainly in the forward direction along the beam axis. It is specialised for the investigation of the difference between matter and antimatter via decay products of hadronized b-quarks.

Luminosity

The number of expected pp collisions, i.e. events, N_{exp} in which a given process occurs over a given time period is given by

$$N_{exp} = \mathcal{L} \cdot \sigma = \int \mathrm{d}t \, \mathscr{L} \cdot \sigma, \tag{4.1}$$

where σ is the cross section for such a process and $\mathscr{L}$ is the instantaneous luminosity. The former depends on the centre-of-mass energy while the latter is dependent on the number of proton bunches per beam n_b, the number of protons per bunch

N_b, the revolution frequency f_{rev}, the relativistic gamma factor γ_r, the normalised transverse beam emittance ϵ_n, the beta function β^* at the interaction point and the geometric luminosity reduction factor F due to a non-zero crossing angle at the interaction point [47] resulting in

$$\mathscr{L} = \frac{N_b^2 n_b \gamma_r f_{rev}}{2\pi\epsilon_n \beta^*} \cdot F. \tag{4.2}$$

The LHC is designed for pp collisions at a nominal integrated luminosity of $\mathcal{L} \sim 10^{34}$ cm^{-2}s^{-1}, using $n_b = 2808$ bunches per beam, with $N_b = 1.15 \cdot 10^{11}$ protons and 25 ns bunch spacing [1]. Figure 4.2(a) shows the delivered integrated luminosity $\mathcal{L}$ as a function of time for Run I (2011 and 2012) and Run II (2015-presumably 2016) data taking periods. In addition, for data taking period in 2016 Figure 4.2(b) shows the peak luminosity per time.
This thesis is based on Run II pp collision data recorded until August 2016.

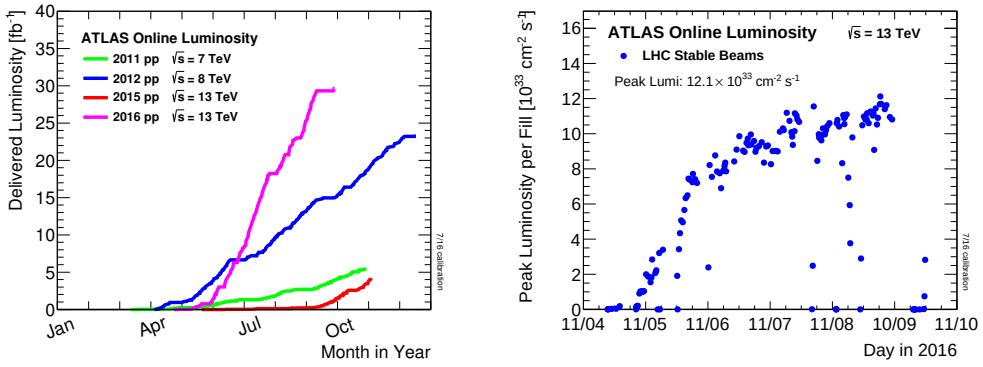

(a) (b)

Figure 4.2: (a) Cumulative integrated luminosity delivered to the ATLAS experiment as a function of the time and (b) the peak luminosity per fill in 2016 [48].

4.2 The ATLAS Detector

The ATLAS detector [49] is one of the two general purpose experiments at the LHC. It is designed for a broad range of physics studies in the harsh LHC experiment, resulting in an efficient trigger system, powerful particle identification, energy and momentum resolution and vertexing. The coverage of almost an entire solid angle by the detector components is also essential to allow for the reconstruction of the complete event topology.

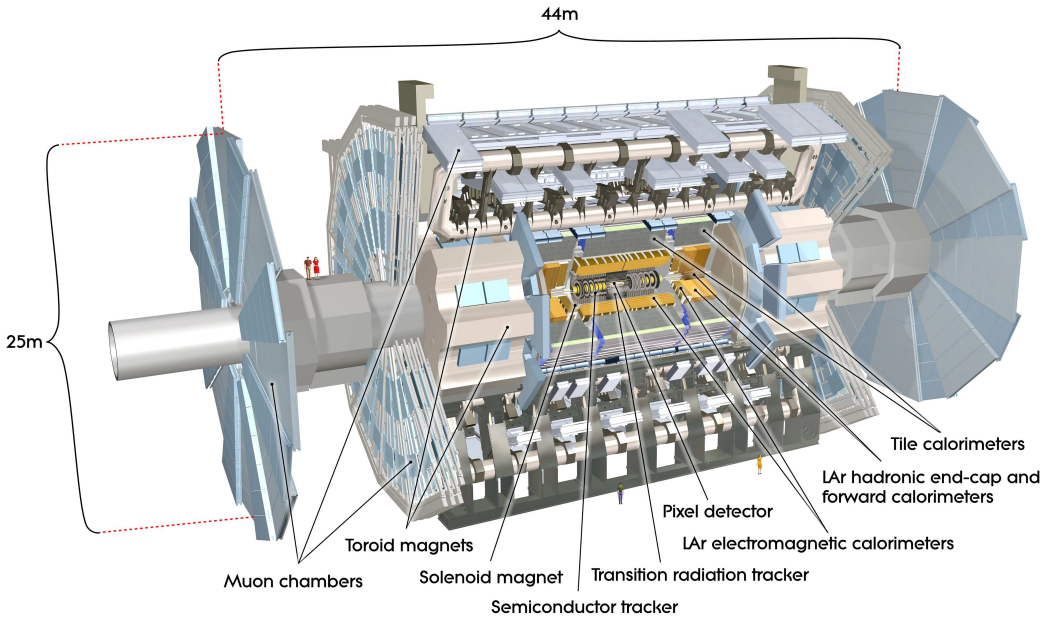

Figure 4.3: Cut-away view of the ATLAS detector [49]. The detector sub-systems are indicated and labelled.

Figure 4.3 shows the ATLAS detector with its sub-detectors. The origin of the right-handed detector coordinate system, shown in Figure 4.4(a), is set to the nominal interaction point [49]. The x-axis is pointing to the centre of the LHC ring, the y-axis points upwards and the z-axis along the beam direction. In cylindric coordinates, the azimuthal angle $\phi \in [-\pi, \pi]$ is measured in the transverse x-y plane relative to the x-axis. The polar angle $\theta \in [0, \pi]$ between the plane and the z-axis is given relative to the positive z-axis. The particle pseudorapidity η is defined as an invariant under longitudinal boost in z-direction,

$$\eta = -\ln \tan\left(\frac{\theta}{2}\right). \tag{4.3}$$

In case of particles where mass is comparable to their energy, rapidity is used instead

$$y = \frac{1}{2} \ln\left(\frac{E + p_z}{E - p_z}\right). \tag{4.4}$$

The angular distance ΔR of two particle trajectories is defined as

$$\Delta R = \sqrt{(\eta_1 - \eta_2)^2 + (\phi_1 - \phi_2)^2} = \sqrt{\Delta\eta^2 + \Delta\phi^2}, \tag{4.5}$$

similarly, $\Delta R_y = \sqrt{\Delta y^2 + \Delta\phi^2}$.

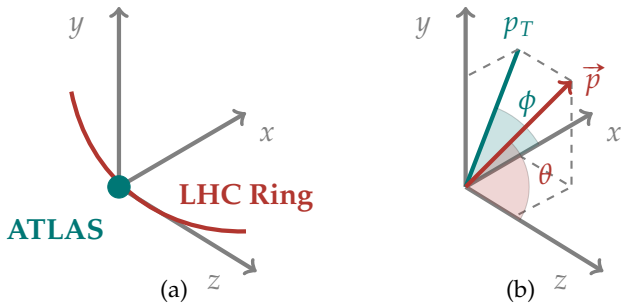

Figure 4.4: (a) Illustration of the ATLAS coordinate system and (b) commonly used polar notation in the ATLAS coordinates.

Several other variables are introduced to describe the trajectory of a particle. The transverse momentum, as shown in Figure 4.4(b),

$$p_T = p \cdot \sin\theta \tag{4.6}$$

is the component of the momentum p in the transverse plane orthogonal to the beam axis. Similarly as p_T, also the energy component is computed in the x-y plane. The closest distance between the trajectory and the reconstructed primary vertex in the transverse plane corresponds to the transverse impact parameter d_0, shown in Figure 4.5(a). The longitudinal impact parameter z_0 is defined as the distance to the closest approach to the interaction point in longitudinal z-direction (see Figure 4.5(b)).

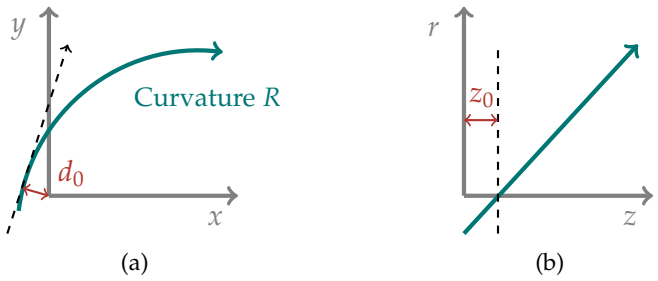

Figure 4.5: (a) Transverse impact parameter d_0 and (b) longitudinal impact parameter z_0.

Along the beam pipe the detector can be divided into three regions, one central barrel region with a cylindric shape, and two lateral end-cap regions with discs of detector components. The innermost part around the beam axis is the Inner Detector (ID), detecting the trajectories of charged particles in a solenoidal magnetic field, thus measuring their momentum and vertex points. It is surrounded by the calorimeter system, including the electromagnetic and the hadronic calorimeter. These are used to identify and measure the energy of photons, electrons and hadrons. The outermost part of the detector is the muon spectrometer which allows for the muon identification and momentum measurement in a toroidal magnetic field. A dedicated triggering system is designed to select interesting events based on the information from all of the ATLAS sub-detectors.

4.2.1 The Trigger System

The detector operates in a high occupancy environment with a bunch crossing frequency of 40 MHz. As it is not possible to record every event a dedicated trigger system is designed to select interesting physics events. In Run II the trigger is composed of two stages, the hardware-based Level-1 (L1) trigger and a software-based High-Level Trigger (HLT) [50, 51].
The L1 trigger performs the initial selection within 2 μs with an output-rate of 100 kHz. Until the trigger decision the detector signals are stored in pipelines of the front-end electronics. The L1 trigger also defines the so-called Regions of Interest (RoI) that are analysed in the next trigger level.
In the next step the software-based HLT processes the information within each RoI for every event accepted by the L1 trigger. The HLT uses fast algorithms equivalent to those used for the offline reconstruction of the particles. It is sub-divided into the fast tracking and the precision tracking part. Fast tracking stage is seeded by the coarse RoI information of the L1 trigger and decides within approximately 40 ms whether the event should be further processed. Subsequently, a detailed precision tracking is performed seeded by the fast tracking stage. The HLT triggering procedure proceeds a decision within 4 s, reducing the original event rate down to 1 kHz. The triggered event is recorded and fully reconstructed by means of the offline ATLAS reconstruction software.

4.2.2 The Inner Detector

The innermost part of the ATLAS detector surrounding the beam pipe is the Inner Detector (ID) [52, 53], shown in Figure 4.6. It is immersed in a 2 T solenoidal magnetic field oriented parallel to the z-axis, which is generated by a superconducting cylindrical coil. The ID allows for the reconstruction of charged particle trajectories,

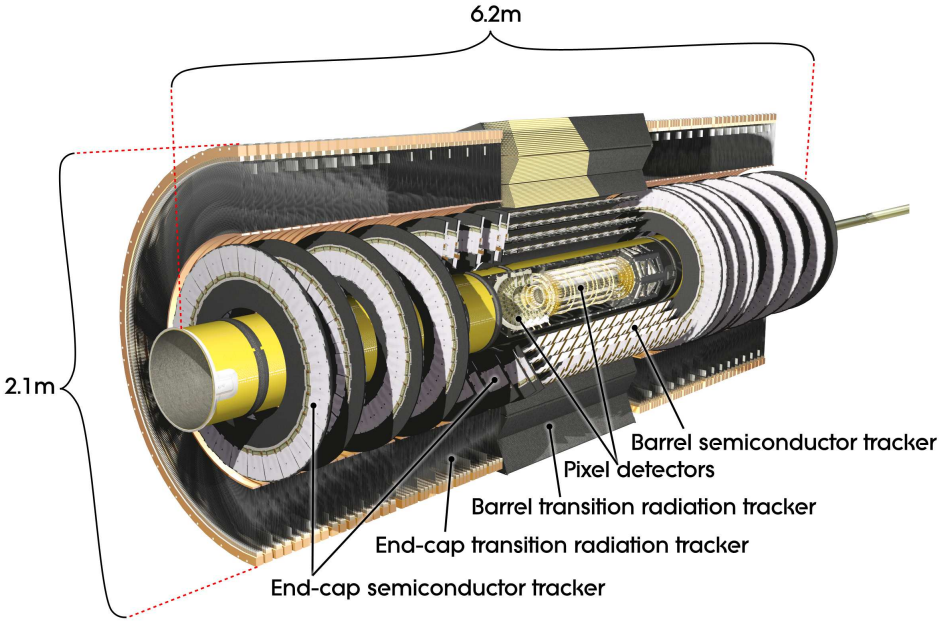

Figure 4.6: Cut-away view of the ATLAS Inner Detector including the pixel, semiconductor and as closest the radiation tracker [49].

so-called tracks, and to measure their momenta. The reconstructed tracks are then extrapolated to common points of origin, identifying the interaction vertex and the decay vertices of secondary particles. The latter are important for the identification of longer-lived particles, such as b-hadrons or τ-leptons. The ID consists of three sub-systems: the pixel detector, the Semiconductor Tracker (SCT) and the Transition Radiation Tracker (TRT), covering a pseudorapidity range of $|\eta| < 2.5$.

The innermost sub-detector surrounding the beam pipe is the pixel detector. It is a silicon-based detector arranged in three layers of concentric cylinders in the barrel region and three pixel discs in both end-cap regions. The cylinders are positioned at radii of 51 mm, 89 mm and 123 mm, while the discs are placed orthogonal to the z-axis at distances $\pm$495 mm, $\pm$580 mm and $\pm$650 mm from the collision point. The spatial resolution provided by the pixel detector is 10 µm in the transverse plane and 115 µm in the longitudinal direction.
In order to improve the impact parameter resolution and thus to increase the vertexing and b-tagging performance, an Insertable B-Layer (IBL) has been added as the innermost pixel layer of a 33 mm distance to the beam pipe during the last shutdown of the LHC [54]. It is made of 14 pixel sensor staves with a length of 640 mm and a width of 20 mm and covers a pseudorapidity range of $|\eta| < 2.9$.

The second high resolution detector of the ID, following directly after the pixel detector, is the SCT. It is arranged in four concentric layers of silicon micro-strip sensors in the barrel and nine discs in the end-region. In order to measure the second coordinate a set of strips with small stereo-angle is placed in each barrel layer parallel to the beam axis. A resolution of 17 μm and of 580 μm is achieved in the R-ϕ plane and in z-direction, respectively.

The last and outermost component is the TRT. In contrast to the other sub-detectors it covers only a pseudorapidity range of $|\eta| < 2.0$. It is composed of straw tubes with a diameter of 4 mm, which are filled with a $Xe/CO_2/O_2$ gas mixture (70%/27%/3%). The dominant component of the gas mixture is Xe, which allows to detect transition-radiation photons created in a radiator between the straws by traversing charged particles. The charged particle tracks are measured with a resolution in the R-ϕ plane of 130 μm per straw.

4.2.3 The Calorimeter System

The second layer of the ATLAS detector is the calorimeter system, shown in Figure 4.7, consisting of the electromagnetic and the hadronic calorimeters [55, 56]. Both are sampling calorimeters employed to measure the energy and trace of the electrons, photons and hadrons, which are absorbed in high density absorber plates. Their deposited energy is measured in active material between. The entire calorimeter system covers a pseudorapidity range of $|\eta| < 4.9$.

The highly granulated electromagnetic calorimeter (ECAL) is surrounding the ID. Its active material is liquid Argon (LAr) filled between alternating layers of accordion-shaped kapton electrodes and lead absorber plates. The ECAL is divided into three concentric layers of different readout granularity. The total thickness is more than 22 interaction lengths, X_0, in the barrel region ($|\eta| < 1.475$) and in the end-caps ($1.375 < |\eta| < 3.2$) more than 24. In order to correct for the energy loss by electrons and photons due to passive material between the ID and the ECAL, a presampler LAr detector is used in the central region $|\eta| < 1.8$. The energy resolution of the ECAL is $\sigma_E/E = 10\%/\sqrt{E}$.

The hadronic calorimeter (HCAL), surrounding the ECAL consists of three parts. The central region ($|\eta| < 1.7$) is covered by a tile calorimeter while a LAr hadronic calorimeter (HEC) is placed to each end-cap ($1.5 < |\eta| < 3.2$). In order to increase the detector hermeticity a LAr forward calorimeter (FCal) is installed in the pseudorapidity region of $3.1 < |\eta| < 4.9$. The total depth of the HCAL is approximately 10 hadronic interaction lengths.

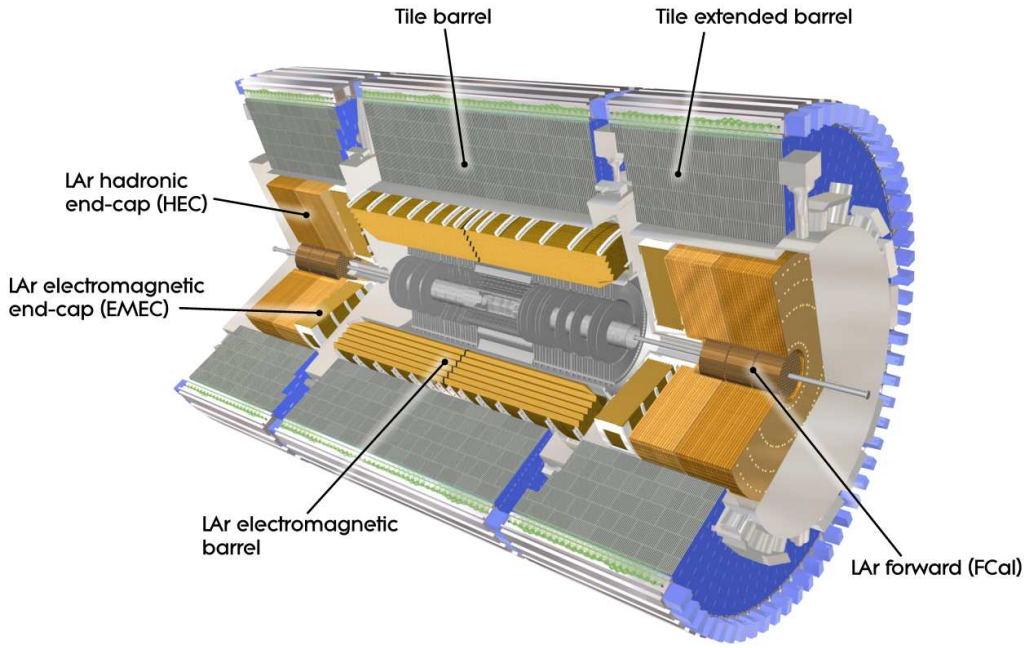

Figure 4.7: Cut-away view of the ATLAS calorimeter system, with the electromagnetic (ECAL) and the hadronic calorimeter (HCAL) [49].

The tile sampling calorimeter with a steel absorber and scintillating tiles as an active material is dedicated into a central part ($|\eta| < 1.0$) and two extended barrels in the range $0.8 < |\eta| < 1.7$. Similarly as the ECAL it is also sub-divided into three layers of different readout granularity with an energy resolution of $\sigma_E/E = 50\%/\sqrt{E}$.
The HEC is located behind the ECAL end-caps and covers a range of $1.5 < |\eta| < 3.2$. The absorbing material is copper interleaved by LAr gaps with read out cells.
The FCal which covers a pseudorapidity range of $3.1 < |\eta| < 4.9$ also employs LAr as active material, while different absorber materials are used. The first layer consists of copper and is optimised for electromagnetic measurements. The other two layers are made out of tungsten to measure the energy of the hadronic interactions. The HEC and the FCal provide an energy resolution of $\sigma_E/E = 100\%/\sqrt{E}$.

4.2.4 The Muon Spectrometer

The outermost and largest part of the ATLAS detector is the Muon Spectrometer (MS) [57], shown in Figure 4.8. It provides the muon triggering, as well as stand-alone precision muon tracking. The MS is embedded in a toroidal magnetic field provided by eight superconducting coils in the barrel region ($\eta < 1.7$) and two further magnet systems in the end-cap region. The generated field strength ranges between 0.5 and 1 T.

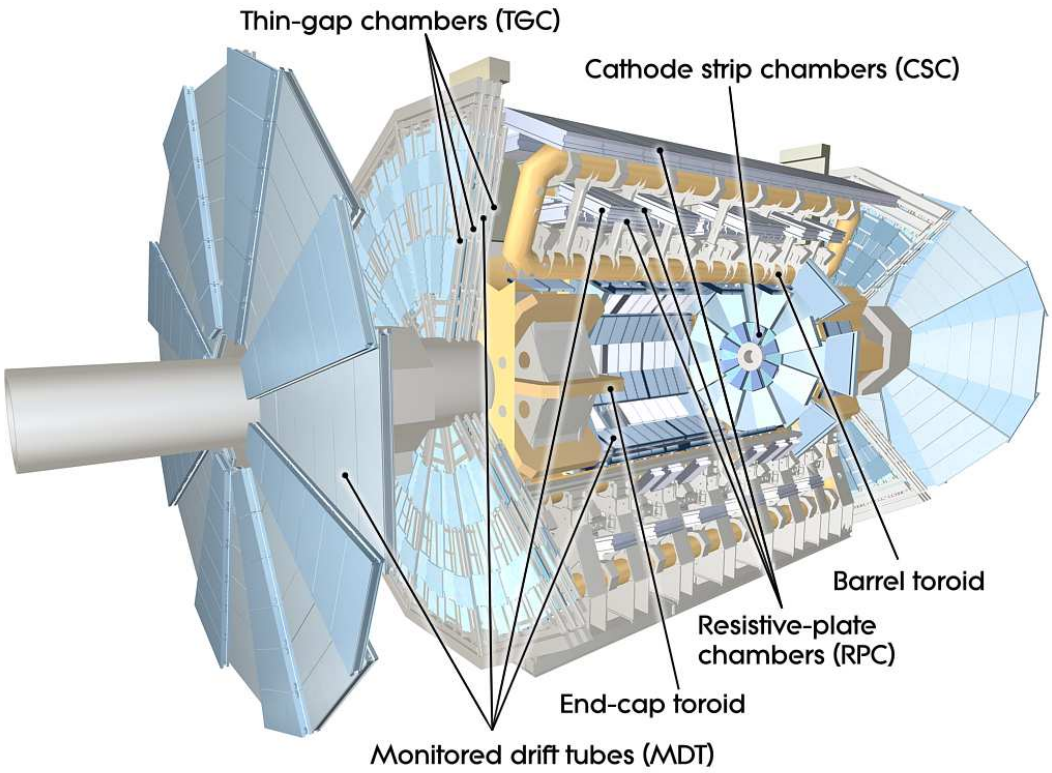

Figure 4.8: Cut-away view of the ATLAS muon spectrometer [49].

Muon candidates are tracked by three layers of high precision tracking detectors, Monitor Drift Tube (MDT) chambers and Cathode Strip Chambers (CSC). The MDT chambers, covering a pseudorapidity range of $|\eta| < 2.7$, consist of six to eight layers of aluminium drift tubes of 30 mm diameter and a wire placed in the centre of each tube. They are filled with a Ar/CO_2 (93%/7%) gas mixture. In the innermost MS end-cap layer ($2.0 < |\eta| < 2.7$), the CSC chambers are installed to cope with the high event background rates. These are multi-wire proportional chambers with

a cathode strip read out. With these precision chambers a spatial resolution of 80 µm in track bending direction is reached, which leads to a transverse momentum resolution of 3-4% at $p_T \approx 100$ GeV and about 10% at $p_T \approx 1$ TeV [58].

The triggering is done by two types of fast triggering chambers, Resistive Plate Chambers (RPC) in the barrel region ($|\eta| < 1.05$) and Thin Gap Chambers (TGC) in the end-cap region ($1.05 < |\eta| < 2.7$). In addition to triggering, they also provide the ϕ coordinate of the muon track and are used for bunch crossing assignment. The time resolution is better than 4 ns.

4.3 Particle Reconstruction and Identification with the ATLAS Detector

Each particle produced in pp collisions leaves a unique fingerprint in one or more of the ATLAS detector sub-systems, as illustrated in Figure 4.9.

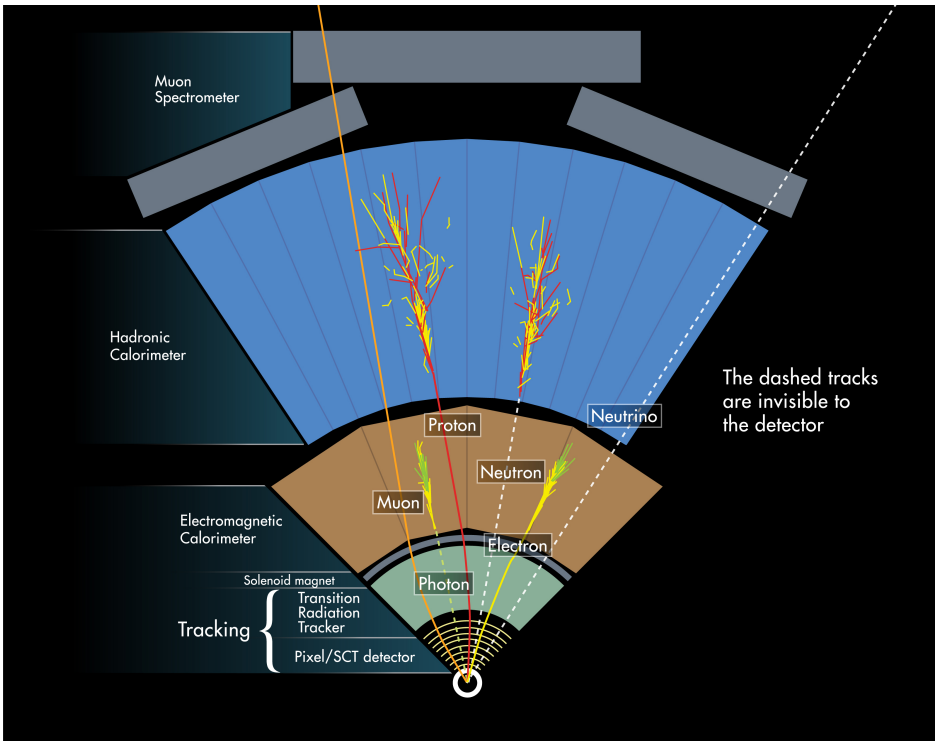

Figure 4.9: Illustration of the particle identification and reconstruction with the ATLAS detector [59]. Each particle leaves an unique fingerprint in one or more of the detector sub-systems.

The trajectories of all charged particles are measured in the ID. The direction of the curvature allows to distinguish between positively and negatively charged particles. The electromagnetically interacting particles, such as electrons or photons deposit most of their energy in the ECAL. The electrons are identified as electromagnetic showers which are matched to a corresponding track in the ID. If there is no such track found in the ID the shower is rather assigned to a photon. Hadrons saturate the ECAL and are stopped in the HCAL producing a hadronic shower. Charged hadrons, such as protons are identified by matching the hadronic shower with a track in the ID and a small energy deposit in the ECAL. Neutrons only produce a shower in the HCAL. Muons, which are minimum ionising particles, typically leave only a small amount of energy in the calorimeter system and can be identified in the muon spectrometer. Particles that interact only weakly with the detector material e.g. neutrinos, can be reconstructed as a missing transverse energy [60], i.e. the negative of the total sum of energies of all visible particles in the transverse plane.

In this thesis Higgs boson decays $H \to ZZ^* \to 4\ell$ are studied with electrons and muons in the final state. In addition, due to different production mechanism also jets from quark and gluon hadronization can be present in the final state. The reconstruction and identification of these particles is discussed in more detail in the following.

4.3.1 Electron Reconstruction and Identification

Electrons are reconstructed within $|\eta| < 2.47$ using a dedicated algorithm [61] by means of the trace information from the ID and the energy deposit in the ECAL. First the energy clusters are reconstructed from the ECAL energy deposit using a dedicated clustering algorithm [62]. The clusters are required from a shower shape consistent with an electromagnetic shower and have an energy above the threshold of 4 GeV. These showers are then loosely matched to reconstructed tracks in the ID. To improve the reconstruction specific energy losses due to electron Bremsstrahlung are taken into account [63].

The background originating from hadrons or converted photons is rejected by the electron identification algorithm [64] which calculates the signal likelihood by means of a multivariate approach with several discriminating variables e.g. requirements of a hit in the IBL, variables describing the longitudinal and transverse shapes of the electromagnetic showers, track-cluster matching conditions and informations from the TRT. With the likelihood method an overall probability is calculated for the object to originate from an electron. Three working points, “Loose”, “Medium” and “Tight” are defined based on this discriminator, providing efficiencies of 95, 92 and 87%, respectively. In the $H \to ZZ^* \to 4\ell$ analysis, the “Loose” working point with

a 95% signal efficiency is chosen. The performance of the electron reconstruction is measured with $Z \to ee$, $J/\psi \to ee$ and dijet events and compared to the simulated values. The identification efficiency in simulation is defined as the ratio of identified relative to the true number of generated electrons. The identification efficiency from simulated $Z \to ee$ events is shown in Figure 4.10(a) as a function of the transverse energy for "Loose", "Medium" and "Tight" electrons. The efficiency for "Loose" electrons increases from 78% to 97% with increasing transverse energy.

The identification efficiency is also determined from calibration data using the tag-and-probe method in $Z \to ee$ ($E_T > 15$ GeV) and $J/\psi \to ee$ (7 GeV $< E_T <$ 20 GeV) events [61]. The combined reconstruction and identification efficiency for "Loose", "Medium" and "Tight" electrons in data and simulation is shown in Figure 4.10(b) as a function of pseudorapidity η. The efficiencies obtained from data are higher for each of the three working points. Thus the corresponding correction factors are applied in simulation. The efficiency for "Loose" electrons ranges between 90% and 95% over the entire η range except for the region of $|\eta| \approx 1.5$ where two calorimeter sub-systems overlap. In this transition region, the efficiency of only about 85% is reached.

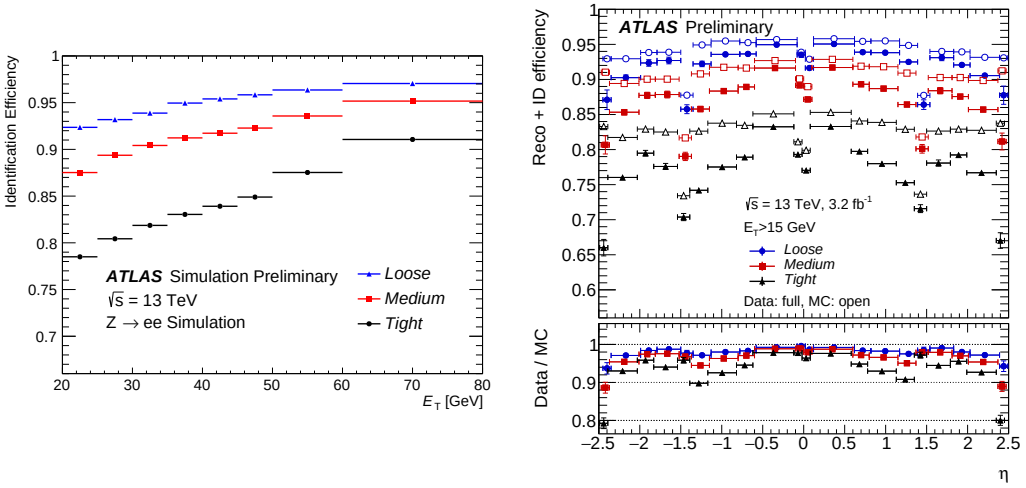

(a) (b)

Figure 4.10: (a) Electron identification efficiency determined from simulated $Z \to ee$ events as a function of the transverse energy E_T for "Loose", "Medium" and "Tight" electrons. (b) Combined reconstruction and identification efficiency for "Loose", "Medium" and "Tight" working points measured in $Z \to ee$ and $J/\psi \to ee$ data and compared to simulation as a function of pseudorapidity η [61].

4.3.2 Muon Reconstruction and Identification

The muon trajectories are first independently reconstructed in the ID and in the MS and then combined using various algorithms [58]. This results in four different types of reconstructed muons.

Combined muon(CB): This is the most frequently reconstructed muon type. The MS track is extrapolated to the interaction point and the corresponding ID track is searched in a nearby cone. A combined track is then obtained from a global refit using the hits in the ID, the energy loss in the calorimeter and the track properties in the MS.

Segment-tagged muons (ST): Muons with low momenta sometimes do not reach all MS layers. If at least one local MS track segment (from the MS layer) can be associated with an extrapolated track from the ID, then this ID track is still identified as a muon. The track parameters are given by the measurement in the ID alone.

Calorimeter tagged muons (CT): This muon type is reconstructed in the region $|\eta| < 0.1$ where the MS is only partially instrumented. A track in the ID is identified as muon if it can be matched to a calorimeter energy deposit compatible with a minimal ionising particle.

Extrapolated muons (ME): The ME muons are used in order to extend the η-acceptance from 2.5 to 2.7. The reconstruction is based on the MS track alone, within a loose requirement on the distance of the extrapolated track to the interaction point and the energy loss in the calorimeter.

A set of quality requirements is applied for the muon identification in order to suppress the background from in-flight decays of pions and kaons. In order to guarantee a robust momentum measurement, all types of muons have to satisfy the following requirements:

- ≥ 1 Pixel hit,
- ≥ 5 SCT hits,
- ≤ 3 Pixel or SCT hole, where a hole is defined as an active sensor traversed by the track but containing no hits,
- at least 10% of TRT hits originally assigned to the track ($0.1 < |\eta| < 1.9$).

The muon identification working point optimised for the $H \to ZZ^* \to 4\ell$ analysis, is the so-called "Loose" selection, maximising the reconstruction efficiency while

keeping a good quality of the muon track. This working point contains all four types of reconstructed muons. The CT and ST muons are limited to the $|\eta| < 0.1$ region and ME tracks are required to have at least three hits in each of three layers of MDT or CSC in $2.5 < |\eta| < 2.7$. A tighter, so-called "Medium" working point contains only CB and ME muons satisfying the following criteria:

- ≥ 3 hits in at least two MDT layers (for $|\eta| < 0.1$ at least one layer),
- ≥ 3 hits in each of three layers of MDT or CSC (in $2.5 < |\eta| < 2.7$),
- q/p significance $= \frac{|q/p_{ID} - q/p_{MS}|}{\sqrt{\sigma_{ID}^2 + \sigma_{ME}^2}} < 7$ to suppress the background from misidentified hadrons as muons from in-flight decays. $q/p_{ID(MS)}$ corresponds to the q/p measurement in the ID (MS) and $\sigma_{ID(MS)}$ are the corresponding uncertainties.

The muon reconstruction efficiency is determined in $Z \to \mu\mu$ and $J/\psi \to \mu\mu$ events using the tag-and-probe method [58]. Figure 4.11(a) shows the muon efficiency as a function of the pseudorapidity η measured in $Z \to \mu\mu$ events ($p_T^\mu > 10$ GeV) for the "Medium" and "Loose" working points. The lowest determined efficiency in $Z \to \mu\mu$ decays in the range $0.1 < |\eta| < 2.5$ is 98%. The loose selection improves the efficiency in $|\eta| < 0.1$ from approximately 62% to 97%. Discrepancies between the data and simulation are corrected with a scale factor applied in the simulation. The p_T dependence of the reconstruction efficiency for "Loose" muons for $J/\psi \to \mu\mu$ and $Z \to \mu\mu$ events is shown in Figure 4.11(b). The scale factors (SF) i.e. the ratio of efficiencies in data and MC is constant and slightly above 99% for $p_T > 6$ GeV.

The corrections of the simulated transverse momentum p_T of reconstructed ID and MS muon tracks are determined using CB muons from $J/\psi \to \mu\mu$ and $Z \to \mu\mu$ decays. Relating to the detector technology and performance the correction factors are calculated separately in 18 pseudorapidity regions in the ID and MS and in case of the MS additional in two ϕ regions. The corrected transverse momentum $p_T^{\text{Cor,Det}}$ (Det=ID,MS) is given by

$$p_T^{\text{Cor,Det}} = \frac{p_T^{\text{MC,Det}} + \sum_{n=0}^{1} s_n^{\text{Det}}(\eta,\phi)\left(p_T^{\text{MC,Det}}\right)^n}{1 + \sum_{m=0}^{2} \Delta r_m^{\text{Det}}(\eta,\phi)\left(p_T^{\text{MC,Det}}\right)^{m-1} g_m}. \tag{4.7}$$

The numerator characterises the momentum scale. The uncorrected transverse momentum in simulation $p_T^{\text{MC,Det}}$ is scaled with correction terms. $s_0^{\text{Det}}(\eta,\phi)$ describes the impact on the transverse momentum due muon energy losses in the detector material and $s_1^{\text{Det}}(\eta,\phi)$ accounts for the imprecision in the description of the magnetic

field integral. The denominator accounts for the additional momentum smearing. It is assumed that the relative p_T resolution in simulation can be described as

$$\frac{\sigma(p_T)}{p_T} = \frac{r_0}{p_T} \oplus r_1 \oplus r_2 \cdot p_T, \tag{4.8}$$

corresponding to the three last terms in the denominator of Equation 4.7. The first term of Equation 4.8 corrects for fluctuations of energy losses in the traversed material and the second for multiple scattering, local magnetic field inhomogeneities and local radial displacement of hits. Intrinsic resolution effects due to spatial resolution of the hit measurement and residual misalignment of the MS are taken into account in the third term. In order to describe the smearing of the momentum correctly, the particular terms of the relative p_T resolution are multiplied with normally distributed random variables g_m with zero mean and unit width.
The described corrections are validated by measuring the peak position of the distribution of the invariant mass $m_{\mu\mu}$ and the resolution $\sigma_{\mu\mu}$ for the two final state muons in J/ψ and Z decays. The ratio is directly proportional to the relative muon momentum resolution

$$\frac{\sigma_{\mu\mu}}{m_{\mu\mu}} = \frac{1}{\sqrt{2}} \frac{\sigma_{p_\mu}}{p_\mu}. \tag{4.9}$$

The relative dimuon mass resolution as a function of the average momentum $\langle p_T \rangle = \frac{1}{2}(p_{T,1} + p_{T,2})$ in case of $J/\psi \rightarrow \mu\mu$ decays and as a function of $p^* = m_Z \sqrt{\frac{\sin\theta_1 \sin\theta_2}{2(1-\cos\alpha_{12})}}$ in case of $Z \rightarrow \mu\mu$ decays is shown in Figure 4.11(c). Here, α_{12} is the opening angle between the two muons. The relative mass resolution determined in data is in a good agreement with the corrected simulation.

4.3.3 Jet Reconstruction and Identification

The products of hadronized partons which shower in the calorimeters are reconstructed as jets of hadronic showers using the anti-k_T-algorithm with a distance parameter $R = 0.4$ [65]. This jet finding algorithm collects the soft QCD-radiation and adds it to the high energy hadrons emerging from the primary hard process. The input to the algorithm are tree-dimensional clusters from topologically connected energy deposits in calorimeter cells. Due to effects of calorimeter non-compensation and inactive material the simulated jet energy is corrected with calibration factors obtained from the comparison of dijet events in collision-data and MC simulations [66].

Several selection criteria are applied in order to distinguish high transverse momentum jets produced in the hard scatter from beam induced background or calorimeter noise. The following set of quality criteria is used:

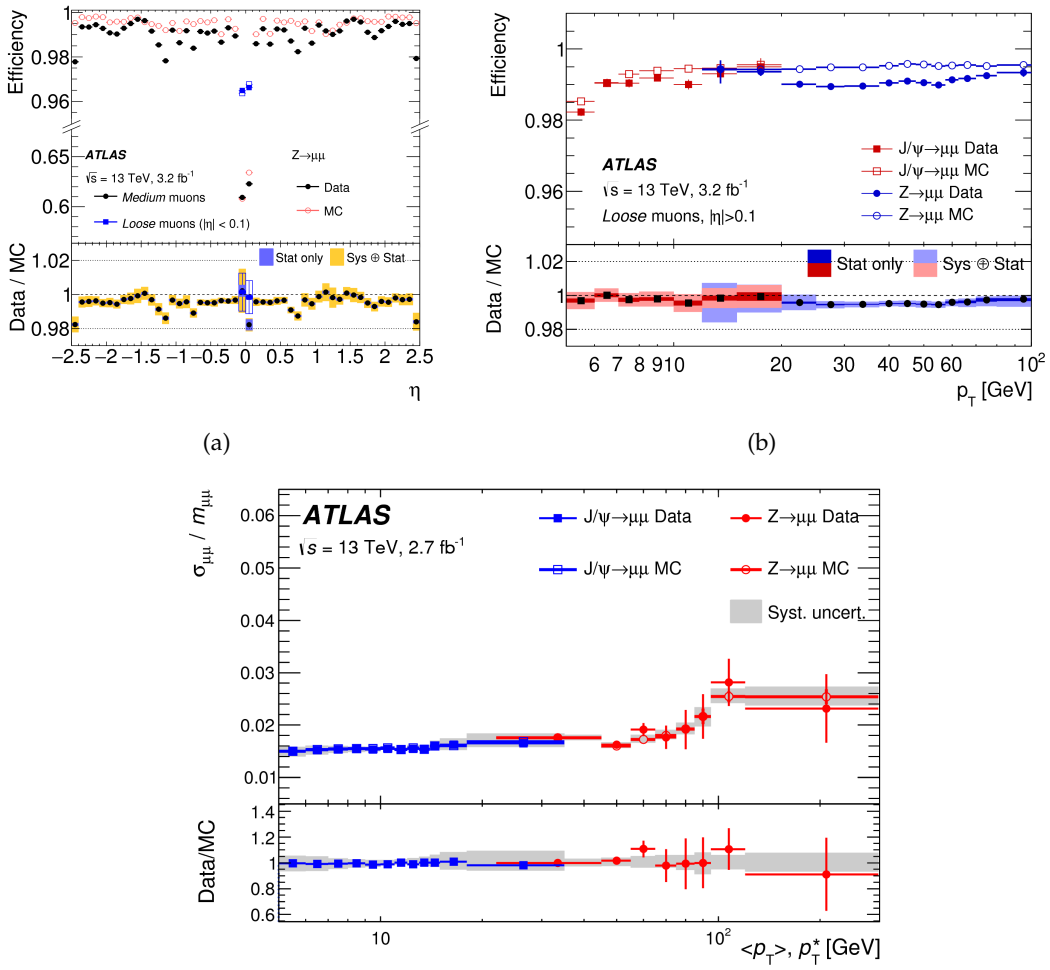

Figure 4.11: (a) Muon reconstruction and identification efficiency as a function of η determined in $Z \to \mu\mu$ events for "Medium" and "Loose" muons with $p_T > 10$ GeV. (b) Measured and simulated reconstruction efficiency for "Loose" muons in $J/\psi \to \mu\mu$ and $Z \to \mu\mu$ decays as a function of the muon p_T. The lower panel shows the ratio of measured and expected efficiencies including the statistical and systematic uncertainties. (c) Relative mass resolution $\frac{\sigma_{\mu\mu}}{m_{\mu\mu}}$ for CB muons as a function of $\langle p_T \rangle = \frac{1}{2}(p_{T,1} + p_{T,2})$ and $p^* = m_Z \sqrt{\frac{\sin\theta_1 \sin\theta_2}{2(1-\cos\alpha_{12})}}$ in $J/\psi \to \mu\mu$ and $Z \to \mu\mu$ events, respectively. The error bars indicate the statistical and the bands the systematic uncertainty [58].

- $Q_{\text{Cell}}^{\text{LAr}}$: Quadratic difference between the actual pulse shape and expected one from simulation, referred as jet quality,
- $\langle Q \rangle$: average jet quality,
- $f_{\text{Q}}^{\text{LAr(HEC)}}$: fraction of energy in the LAr (HEC) calorimeter cells with $Q_{\text{Cell}}^{\text{LAr}} > 4000$,
- E_{neg}: total energy in all cells with negative energy,
- f_{max}: maximum of energy fractions in each calorimeter layer,
- $f_{\text{EM(HEC)}}$: fraction of the total energy deposited in the ECAL (HEC), and
- f_{ch}: transverse momenta p_T of all tracks originating from the primary vertex divided by the jet p_T.

The jets selected at the "Loose" working point, which is used for the $H \to ZZ^* \to 4\ell$ analysis, are rejected if they fulfil at least one of the following criteria

- $f_{\text{HEC}} > 0.5$, $|f_{\text{Q}}^{\text{HEC}}| > 0.5$ and $\langle Q \rangle > 0.8$,
- $|E_{\text{neg}}| > 60$ GeV,
- $f_{\text{EM}} > 0.95$, $f_{\text{Q}}^{\text{LAr}} > 0.8$, $\langle Q \rangle > 0.8$ and $|\eta| < 2.8$,
- $f_{\text{max}} > 0.99$ and $|\eta| < 2$,
- $f_{\text{EM}} < 0.05$, $f_{\text{ch}} < 0.05$ and $|\eta| < 2$, or
- $f_{\text{EM}} < 0.05$, $|\eta| \geq 2$.

Another selection is the "Tight" working point. It is designed for a higher fake jet rejection with an inefficiency for good jets of up to a few percent.

The selection efficiency is studied in dijet events using the tag-and-probe method [66]. Figure 4.12(a) shows the selection efficiency in collision-data for both working points "Tight" and "Loose" as a function of the pseudorapidity η. It is measured to be nearly 1 for "Loose" selected jets except in one bin at very high η. The lower panel shows the ratio of the selection efficiency in data and MC simulation, which are for both working points in a very good agreement.
The jet energy is corrected with a scale factor delivered from simulated dijet events after correcting for the position of the hard-scatter vertex and pile-up [67]. In Run II there are on average 20 additional soft pp collisions occurring in each proton bunch crossing. The impact of these so-called pile-up events is taken into account with the

pile-up correction. The scale factor is the ratio of the reconstructed and the simulated jet energy. Figure 4.12(b) shows the average energy response, which is the inverse of the scale factor, at various jet energies as a function of the pseudorapidity η. The inverse of the scale factor increases with increasing energy. Gaps and transitions between the sub-detectors of the calorimeter result in a lower energy response.

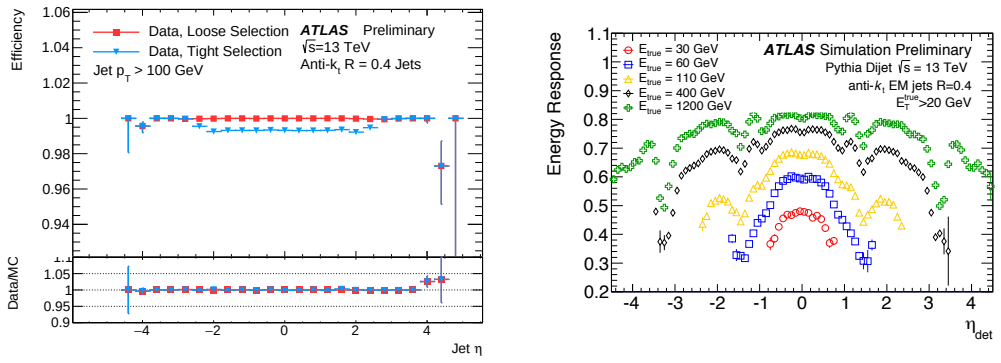

(a) (b)

Figure 4.12: (a) Jet selection efficiency in collision-data for jets reconstructed with the anti-k_T-algorithm with a distance parameter $R = 0.4$ for the working point "Tight" and "Loose" as a function of pseudorapidity η. The lower panel shows the ratio of the selection efficiency in data and MC simulation [66]. (b) Energy response for various jet energies as a function of the pseudorapidity η for jets reconstructed with the anti-k_T-algorithm with a distance parameter $R = 0.4$ [67].

Chapter 5

Measurement of the Higgs Boson Decay Process $H \to ZZ^* \to 4\ell$

5.1 The $H \to ZZ^* \to 4\ell$ Decay Channel

The main focus of the LHC physics program after the discovery of the Higgs boson in 2012 [2, 3] is to study its properties. The measurement of the Higgs boson decays into Z bosons allows for the study of Higgs boson coupling properties.
The branching ratio (BR) for the decay of the SM Higgs boson with a mass of 125 GeV into a Z boson pair is approximately 2.5% (Section 3.3). One of the two Z bosons is produced off-shell since the mass of the Higgs boson is below the threshold of 180 GeV for two real Z bosons. The Z bosons subsequently decay either hadronically or leptonically [27], resulting in several possible final state configurations. Hadronic Z boson decays with the BR of about 70% are dominant, but rather difficult to distinguish from the large QCD multijet background. The most probable leptonic decay of the Z boson is the decay into neutrinos with a BR of 20%. Since the neutrinos escape the ATLAS detector without being detected, they can only be identified via the total missing transverse energy. Therefore, the most promising decay mode, with a branching ratio of 0.0124% [36], is the decay in which the two Z bosons decay into a pair of electrons or muons, $H \to ZZ^* \to 4\ell$, shown in Figure 5.1.

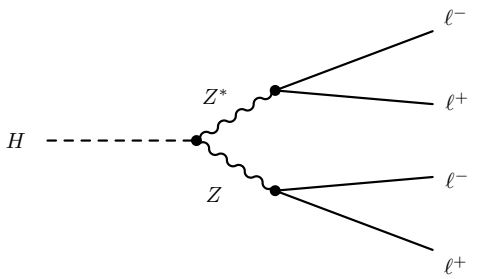

Figure 5.1: Tree-level diagram of a Higgs boson decay into two Z bosons which subsequently decay into a pair of oppositely charged leptons.

This decay channel provides a very clean signature with a high signal to background ratio and fully reconstructed four-momenta of all decay products.
There are four possible final states with slightly different background compositions: $4e$ and 4μ state, in which both Z bosons decay into electrons or muons, and $2e2\mu$ ($2\mu 2e$) final states in which the on-shell Z boson decays into a pair of electrons (muons) and the off-shell into muons (electrons). The requirement of isolated leptons with small impact parameter efficiently rejects the background from QCD processes. The high lepton reconstruction efficiency and the high energy and momentum resolution (Section 4.3) allows for a very good invariant mass resolution of about 1-2%.

5.2 Background Processes

In order to study the properties of the Higgs boson decay $H \rightarrow ZZ^* \rightarrow 4\ell$, a good understanding of the corresponding background processes is needed. These can be divided into irreducible and reducible background contributions, as discussed in the following.

5.2.1 Irreducible Background Processes

The dominant background contribution in the $H \rightarrow ZZ^* \rightarrow 4\ell$ decay channel originates from the continuum SM $\left(Z^{(*)}/\gamma^{(*)}\right)\left(Z^{(*)}/\gamma^{(*)}\right)$ pair production, referred to as ZZ^* in the following, in which the Z bosons or photons decay into a pair of leptons.
The dominant ZZ^* production mode with a total production cross section of 1267 fb^{-1} [68], is the production via quark-antiquark annihilation. Additional, much smaller contribution with a production cross section of 11 fb^{-1} originates from the gluon induced ZZ^* production [68]. The latter process is only possible via a quark loop, because Z bosons do not couple directly to gluons. The corresponding lowest-order Feynman diagrams are shown in Figure 5.2.
As this background results in the same event topology as the signal, it is denoted as irreducible background. The number of expected events originating from the ZZ^* background is estimated by means of Monte Carlo (MC) simulation.

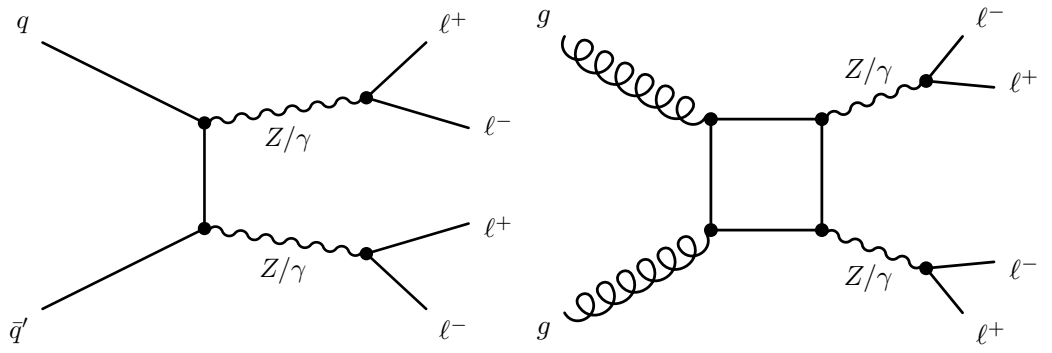

Figure 5.2: The lowest-order Feynman diagrams for the SM ZZ^* background production (a) via quark-antiquark annihilation and (b) gluon induced processes.

5.2.2 Reducible Background Processes

In contrast to the large background contribution from the ZZ^* production, the reducible background contribution is very small. The contributing processes, shown in Figure 5.3, are Z+jets, $t\bar{t}$ and WZ. At least one of the four identified leptons in these processes originates from a gluon or quark induced jet. The lepton isolation criteria therefore allows for the discrimination from the signal process. The reducible background is estimated using control data as described in Section 5.5.
The dominant contribution of the reducible background originates from the Z+jets production. One pair of same-flavour leptons ($\ell\ell$) with opposite charge and an invariant mass closest to the Z boson mass is assigned to the Z boson decay. The flavour of leptons in the secondary lepton pair distinguishes between $\ell\ell + \mu\mu$ (muon) and $\ell\ell + ee$ (electron) final states, whose contribution is separately determined from control data. The former final state originates mainly from semileptonic b- and c-quark decays (Z+ heavy flavour jets) and in-flight π and K decays (Z+ light flavour jets). Also the $t\bar{t}$ production with leptons from W bosons and b-quarks contributes to the reducible background with non-isolated muons. The WZ production on the other hand is very rare. The $\ell\ell + ee$ final state mostly originates from photon conversion of light flavour jets misidentified as electrons. A small $\ell\ell + ee$ contribution originates from semi-leptonic decays of heavy flavour hadrons.
Other reducible background processes considered in this analysis are $t\bar{t}V$ and triboson processes. Their contribution is very small and the expected number of events are taken from simulation.

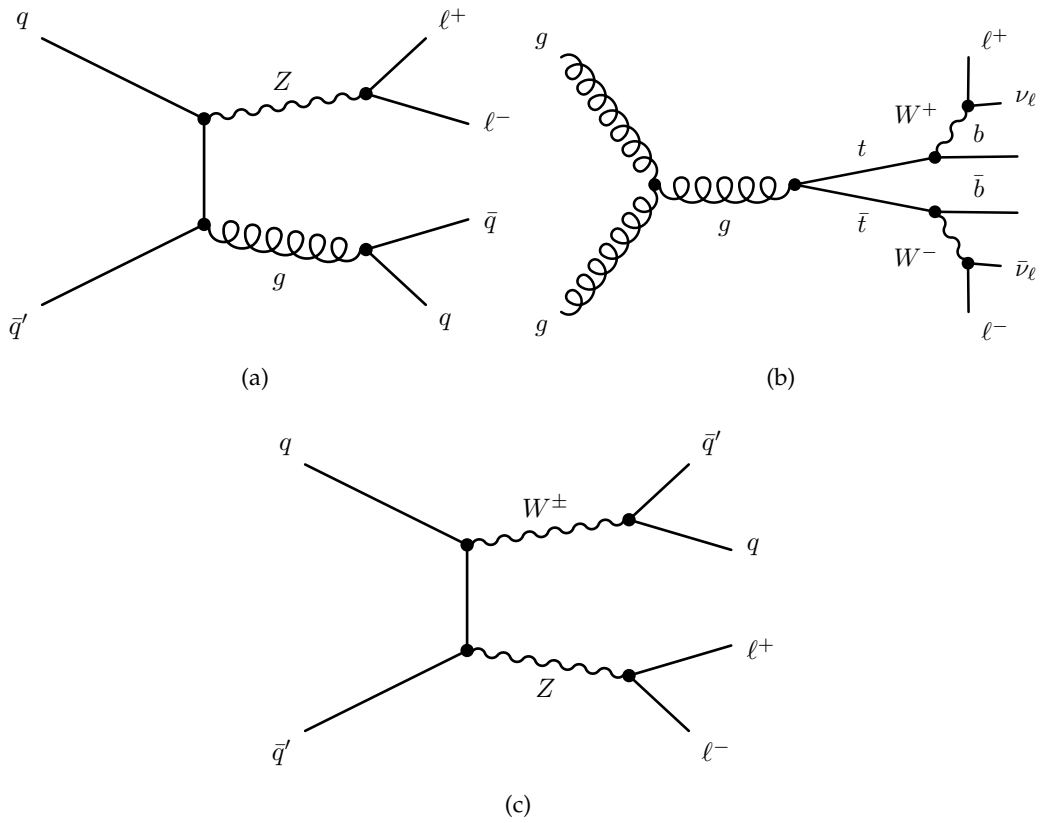

Figure 5.3: Example of the tree-level Feynman diagrams for the dominant reducible background processes in the $H \to ZZ^* \to 4\ell$ decay channel: (a) Z+jets, (b) $t\bar{t}$ and (c) WZ.

5.3 Data and Monte Carlo Samples

This analysis is based on the LHC pp collision data at a centre-of-mass energy of $\sqrt{s} = 13$ TeV collected in 2015 and 2016 with the ATLAS detector. The integrated luminosity of the analysed dataset is 14.78 fb^{-1}.

The signal and the background processes are modelled using MC simulation. The ggF and VBF SM Higgs boson production is simulated with the MC event generator POWHEG-BOX v2 [69, 70], accounting for QCD corrections up to next-to-leading order (NLO). The showering and the hadronization is performed with PYTHIA8 [71] which is interfaced in EvtGen v1.2.0 [72] in order to simulate b- and c-hadron decays. Since no samples are produced for b$\bar{\text{b}}$H the ggF cross section is scaled

to account for this process. For the modelling of the Higgs boson production in association with a W or Z boson PYTHIA8 is used. The $t\bar{t}H$ production is simulated with MADGRAPH5_AMC@NLO generator [73] interfaced with HERWIG++ [74] for showering and hadronization. The generated signal MC samples are normalised to the most accurate currently available production cross section and branching ratios [36].

The irreducible ZZ^* background produced via quark-antiquark annihilation is simulated with POWHEG-BOX v2, the parton showering and hadronization is done with PYTHIA8 and for b- and c-hadron decays EVTGEN v1.2.0 is used. The modelling of non-perturbative effects is done with AZNLO [75]. In addition next-to-next-to leading (NNLO) QCD and NLO EW corrections are taken into account [76–78]. Gluon induced ZZ^* production is also simulated with POWHEG-BOX v2. In order to account for interference effects between the final state and background the parton-level integrator and event generator GG2VV [79] is used in addition. Higher order QCD effects, calculated for massless top-quark loops [80, 81] in the heavy top-quark approximation [82], are included by applying a k-factor.
The WZ samples are produced with POWHEG-BOX v2 interfaced to PYTHIA8 and EVTGEN v1.2.0. The background from $t\bar{t}$ decays is simulated in the same way, but PYTHIA6 is used instead of PYTHIA8. The Z+ jets background is modelled with the SHERPA generator [83], which is also used for the tri-boson background (ZZZ, WZZ, WWZ). The fully leptonic $t\bar{t} + Z$ background is generated with MADGRAPH5_AMC@NLO.
The generated events are processed by the ATLAS detector simulation [84] within the GEANT4 framework [85] in order to account for the interaction of generated particles (truth particles) with the detector material. Additional pp collisions taking place in the same or neighbouring bunch crossings (pile-up events) are simulated and superimposed in a separate step during the digitalisation.

The complete list of MC samples used in this analysis can be found in Appendix A.

5.4 Event Selection

In the first stage of the event selection, so-called preselection, events are required to fulfil certain data quality criteria. Events are rejected if any of the relevant detector components was not operating correctly during the data taking. Furthermore, only events with at least one reconstructed vertex containing two or more associated tracks are considered. The tracks are required to have $p_T^{\text{track}} > 400$ MeV. The vertex with largest $\sum_{\text{i}\in\text{track}} \left(p_{T,i}^{\text{track}}\right)^2$ is chosen as the primary vertex.

Single-lepton, di-lepton, tri-lepton and mixed electron-muon trigger are used in order to select the four-lepton events. Events are accepted by the trigger if certain muon (electron) identification criteria and p_T (E_T) thresholds are fulfilled. In the case of the single-muon trigger additional isolation requirements are imposed. A summary of different trigger thresholds used during the data taking periods in 2015 and 2016 is given in Appendix B.

The four lepton events are classified according to the lepton flavour into 4μ, $2e2\mu$, $2\mu2e$ and $4e$ Higgs boson candidates. The following selection criteria are imposed. Only electrons with $E_T > 7$ GeV and $|\eta| < 2.47$ and muons with $p_T > 5$ GeV and $|\eta| < 2.7$ are selected. CT muons are additionally required to have $p_T >$15 GeV to compensate for the MS acceptance gap in $|\eta| < 0.1$. As the four leptons should emerge from the primary vertex, leptons with a longitudinal impact parameter of $z_0 \cdot \sin(\theta) > 5$ mm are not accepted. This requirement reduces also background from hadronized b-quarks. The cosmic background is suppressed by the cut on the absolute value of the muon transverse impact parameter ($|d_0| < 1$ mm).

Two same-flavour and opposite-charged lepton pairs are combined into a lepton quadruplet, referred to as Higgs candidate. The highest-p_T lepton is required to have $p_T > 20$ GeV, the next $p_T > 15$ GeV and the third one $p_T > 10$ GeV. In addition, the selected leptons should be well separated in space. Therefore, the distance $\Delta R = \sqrt{\Delta\eta^2 + \Delta\phi^2}$ between same- (different-) flavour leptons is required to be larger than 0.10 (0.20). Leptons from $J/\psi \to \ell^+\ell^-$ decays are rejected by the requirement of $m_{\ell\ell} > 5$ GeV for same-flavour opposite-charge di-lepton pairs.
The two di-lepton pairs in the quadruplet are assigned to the two Z bosons from the Higgs boson decay by means of their invariant masses. The di-lepton pair with an invariant mass m_{12} closest to the Z boson mass [27], called the leading di-lepton pair, is required to have 50 GeV $< m_{12} <$ 106 GeV. The sub-leading di-lepton pair, which is associated with the off-shell Z boson, is required to have an invariant mass $m_{\text{threshold}} < m_{34} <$ 115 GeV. The value $m_{\text{threshold}}$ is a function of the four-lepton invariant mass $m_{4\ell}$. For $m_{4\ell} <$ 140 GeV this is 12 GeV, rising linearly to a maximum value of 50 GeV for $m_{4\ell} \geq$ 190 GeV. In the case that more than one lepton quadruplet survive the kinematic selection, the one with m_{12} and m_{34} closest the Z boson mass is retained.

The contribution from the Z+jets and $t\bar{t}$ production can be reduced by the requirement of isolated leptons. Leptons pass the isolation cut if the size of track-based isolation variable is smaller than 0.15. For muons and electrons it is defined as

$$I_{\mu}^{track} = \frac{\sum_i p_{T,i}^{\text{track}} \, (\Delta R \leq 0.3)}{p_T^{\mu}} \quad \text{and} \tag{5.1}$$

$$I_{e}^{track} = \frac{\sum_i p_{T,i}^{\text{track}} \, (\Delta R \leq 0.2)}{E_T^{e}}, \quad \text{respectively,} \tag{5.2}$$

where $p_{T,i}^{track}(\Delta R)$ is the transverse momentum of a track i in a cone of the size ΔR around a muon or an electron. Additional calorimeter-based isolation is required with $I_{\mu(e)}^{calo} < 0.3(0.2)$ where

$$I_{\mu}^{calo} = \frac{\sum_i E_{T,i}^{\text{Cluster}} \, (\Delta R \leq 0.2)}{p_T^{\mu}}, \tag{5.3}$$

$$I_{e}^{calo} = \frac{\sum E_{T,i}^{\text{Cluster}} \, (\Delta R \leq 0.2)}{E_T^{e}}. \tag{5.4}$$

Reducible background from b- and c-hadron decays is further suppressed by a cut on the transverse impact parameter significance $|d_0/\sigma_{d_0}|$, where σ_{d_0} is the uncertainty of the d_0 measurement. All muons (electrons) are required to have $|d_0/\sigma_{d_0}| < 3$ (5).

A so-called 4ℓ-vertex cut is performed to insure that the leptons originate from the same vertex and thus to further suppress the reducible background. The track parameters of the four lepton candidates are fitted under the assumption that the leptons emerge from the same vertex point [86]. The 4μ (other 4ℓ) candidates are accepted if the fit quality, i.e. χ^2 divided by the number of degrees of freedom (N_{dof}) is less than 6(9).

The requirements on the lepton kinematic properties, the Higgs boson candidate selection as well as the lepton isolation criteria and the 4ℓ-vertex selection are summarised in Table 5.1.

5.5 Estimation of the Reducible Background

As mentioned in Section 5.2.2, the contribution of the reducible background from Z+jets and $t\bar{t}$ production is estimated using a data-driven approach, e.g. by means of control regions (CR) of data with enhanced background and suppressed signal contributions. The number of events in such regions is much higher than in the signal region (SR) defined by the event selection in Section 5.4. This allows for a

Table 5.1: Event selection criteria applied in the $H \to ZZ^* \to 4\ell$ analysis [87].

LEPTON REQUIREMENTS	
Electrons	$E_T > 7$ GeV and $\lvert\eta\rvert < 2.47$
	$z_0 \cdot \sin(\theta) < 5$ mm
Muons	$p_T > 5$ GeV and $\lvert\eta\rvert < 2.7$
	$p_T > 15$ GeV and $\lvert\eta\rvert < 0.1$ (CT muons)
	$z_0 \cdot \sin(\theta) < 5$ mm
	$\lvert d_0\rvert < 1$ mm
EVENT SELECTION	
Higgs Boson Candidate	Two lepton pairs of same-flavour and opposite-charge
	$p_T > 20, 15, 10$ GeV for the three highest-p_T leptons
	$\Delta R(\ell, \ell') > 0.10$ (0.20) for same- (different-) flavour leptons
	$m_{\ell\ell} > 5$ GeV for same-flavour opposite-charge di-lepton pairs
	50 GeV $< m_{12} <$ 106 GeV
	$m_{\text{threshold}} < m_{12} <$ 115 GeV
Lepton Isolation	Muon track isolation ($\Delta R \leq 0.3$): $I_\mu^{track} < 0.15$
	Muon calorimeter isolation ($\Delta R = 0.2$): $I_\mu^{calo} < 0.30$
	Electron track isolation ($\Delta R \leq 0.2$): $I_e^{track} < 0.15$
	Electron calorimeter isolation ($\Delta R = 0.2$): $I_e^{calo} < 0.20$
	$\lvert d_0/\sigma_{d_0}\rvert < 3(5)$ for muons (electrons)
Vertex Selection	$\chi^2/N_{\text{dof}} < 6$ for 4μ candidates
	$\chi^2/N_{\text{dof}} < 9$ for $2e2\mu$, $2\mu2e$, $4e$ candidates

thorough comparison of the simulated and observed background. The CR are built by relaxing or inverting the lepton selection criteria for two of the four leptons. For each background component there is a dedicated separate CR enriched by the corresponding background events.
The expected yields of the different background components are obtained from a simultaneous fit of all CR. The yields obtained from CR are extrapolated to the SR by multiplying the yield determined in the given CR with the so-called fake factor. The fake factor is the average per-event probability of a given background process in CR to pass the additional final selection which has been relaxed or inverted for that CR. The fake factors are determined from MC simulation, with additional cross checks of the single lepton selection efficiencies determined in dedicated validation data. In this validation data the efficiency of the additional lepton passing the relaxed or inverted selection is calculated for both, data and MC simulation. The difference

between the lepton selection efficiencies is applied as a systematic uncertainties on the corresponding fake factor [87].
Since the dominant background contribution is dependent on the flavour of the sub-leading di-lepton pair, the reducible background is estimated separately for $\ell\ell + \mu\mu$ and $\ell\ell + ee$ final states. This thesis concentrate on the former one.

5.5.1 Estimation of the Reducible $\ell\ell + \mu\mu$ Background

The main contribution to the reducible $\ell\ell + \mu\mu$ background originates from the Z boson production with additional muons from semi-leptonic decays of b- and c-hadrons, referred to as Z+heavy flavour jets (Z + HF). This contribution can be enhanced by inverting the d_0 significance cut for at least one of the leptons in the sub-leading di-lepton pair. In addition, both leptons in that pair have to fail the isolation selection criteria. The corresponding CR is called *"inverted d_0 CR"*.
The smaller contribution from the $t\bar{t}$ production process is studied in the so-called *"$e\mu + \mu\mu$ CR"*. The leptons in the leading di-lepton pair are required to have opposite-charge and different-flavour. For the leptons in the sub-leading di-lepton pair there is no cut applied on the d_0 significance and lepton isolation. All other selection criteria are as described in Section 5.4.
The third and last CR which is enriched in Z boson production accompanied by leptons from in-flight decays of π and K in light flavour jets, denoted as Z + LF. At least one of the muons of the sub-leading muon pair is required to fail the isolation selection, hence the so-called *"inverted isolation CR"*. In order to suppress the remaining Z + HF component in this control region, muons are required to pass the d_0 significance cut.
Table 5.2 summarises the definition and the fake factors of the three CR. The efficiencies used to calculate the fake factors are obtained from MC simulation.

Table 5.2: Definition of *"inverted d_0 CR"*, *"$e\mu + \mu\mu$ CR"* and *"inverted isolation CR"* for the background components Z + HF, $t\bar{t}$ and Z + LF and corresponding fake factors.

Background component	Control region		Fake factor
Z + HF	*"inverted d_0 CR"*	inverted $\lvert d_0/\sigma_{d_0}\rvert$ cut inverted $I_\mu^{track\ \&\ calo}$ criteria	$\frac{\epsilon_{iso\ \&\ d_0}^{\mu\mu}}{1-\epsilon_{iso\ \&\ d_0}^{\mu\mu}}$
$t\bar{t}$	*"$e\mu + \mu\mu$ CR"*	no $\lvert d_0/\sigma_{d_0}\rvert$ cut no $I_\mu^{track\ \&\ calo}$ criteria	$\epsilon_{iso\ \&\ d_0}^{\mu\mu} \cdot \left(\frac{\epsilon_{\ell\ell}}{\epsilon_{e\mu}}\right)$
Z + LF	*"inverted isolation CR"*	inverted $I_\mu^{track\ \&\ calo}$ criteria $\lvert d_0/\sigma_{d_0}\rvert$ cut	$\frac{\epsilon_{iso}^{\mu\mu}}{1-\epsilon_{iso}^{\mu\mu}}$

The contribution of the WZ process to the reducible background is very small. Hence, no CR region is built and it is estimated from MC simulation.

The expected Z + HF and $t\bar{t}$ event yields in the CRs are determined by means of an unbinned maximum-likelihood fit of the invariant mass m_{12} spectrum simultaneously in the first two CR. The m_{12} distribution of the Z + HF component is modelled by a Breit-Wigner distribution quadratically added to a Crystal Ball function, while for the $t\bar{t}$ component a second-order Chebyshev polynomial is used. The *"inverted isolation CR"*, enriched in Z + LF, is not included into the simultaneous fit, due to a very small number of simulated events in that region. In order to determine the expected yield for the Z + LF component the fit is first performed with the *"inverted d_0 CR"* and *"$e\mu + \mu\mu$ CR*. The event yields obtained from the above fit are fixed and the fit to the *"inverted isolation CR"* is applied to estimate the yield of the remaining Z + LF contribution.
The fake factor extrapolating the contribution of the $\ell\ell + \mu\mu$ event from CRs with relaxed muon impact parameter and isolation criteria into the SR is calculated from the simulated Z+jet events containing heavy flavour jets. As the number of simulated events with light flavour jets is limited, an assumption is made that the isolation efficiency from Z + HF jet applies also for events with light flavour jets. This assumption, as well as the agreement of the fake factors determined in simulation with those in data can be tested in a dedicated $Z + \mu$ validation sample. Instead of two muons with relaxed selection criteria, only one such muon is required in the final state in addition to the di-lepton pair associated with the Z boson [87].

The total muon background estimation in the CR and in the SR, as well as the determined fake factors are given in Table 5.3. The uncertainties of the fake factors are based on the validation studies described in Section 5.5.2.

Table 5.3: Fitted $\ell\ell + \mu\mu$ event yields at $\mathcal{L} = 14.78$ fb^{-1} in the *"inverted d_0 CR"* for the Z + HF component, the *"$e\mu + \mu\mu$ CR"* for the $t\bar{t}$ component the *"inverted isolation CR"* for the Z + LF component. The corresponding fake factors and the expected event yields in the SR are also shown. The statistical and in SR also the systematic uncertainties are given [87].

Background	Fit yield in CR	Fake factor [%]	Yield in SR
Z + HF	348 ± 29	0.60 ± 0.04	$2.10 \pm 0.17 \pm 0.13$
$t\bar{t}$	351 ± 14	0.21 ± 0.03	$0.74 \pm 0.03 \pm 0.00$
Z + LF	10 ± 15	2.30 ± 0.30	$0.24 \pm 0.35 \pm 0.03$
WZ	(MC based estimation)		0.63 ± 0.31

In the following, the validation of the muon fake factors, which was one of the thesis goals, will be described in more detail.

5.5.2 Validation with $Z + \mu$ Events

In order to verify the simulation-based fake factors for a di-muon with inverted isolation and d_0 significance cut, the single muon isolation and d_0 significance is additionally studied in the so-called $Z + \mu$ validation data.
The $Z + \mu$ events are selected by the single- and di-lepton trigger. The Z boson di-lepton candidate is selected by requiring an opposite-charge muon or electron pair passing the nominal lepton identification, isolation- and d_0 selection. Furthermore, the two leptons in the leading pair have to satisfy $p_T > 20$ GeV and 15 GeV, respectively. The invariant mass of the two leptons is required to be in the range $76\,\text{GeV} < m_{\ell\ell} < 106\,\text{GeV}$ and the two leptons are required to pass the d_0 significance, the calorimeter and track isolation selection. In addition they have to be well separated from each other ($\Delta R > 0.1$). To such a leading lepton pair, exactly one additional CB muon with $p_T > 5$ GeV is required. No cut on the d_0 significance and no isolation criteria are applied on this additional muon. Moreover, the muon has to be separated by $\Delta R > 0.1$ (0.2) from the $\mu\mu(ee)$ Z boson candidate. To reject events from $J/\psi \to \mu\mu$ decays, leptons of same-flavour and opposite-charge have to satisfy $m_{\ell\ell} > 5$ GeV.
Figure 5.4 shows the observed and expected reconstructed invariant mass m_{12} of the Z boson candidates from the $Z + \mu$ validation sample. The expected and observed number of events are given in Table 5.4.

Table 5.4: Expected and observed number of events in the $Z + \mu$ validation sample with the corresponding MC statistical uncertainties at an integrated luminosity of 14.78 fb^{-1}.

Sample	Events	Contribution [%]
$Z + \text{HF}$	72101.8 $\pm$ 229.4	61.8
$Z + \text{LF}$	36151.8 $\pm$ 654.2	31.0
$t\bar{t}$	5934.0 $\pm$ 23.5	5.1
WZ	2070.4 $\pm$ 15.8	1.8
ZZ^*	413.8 $\pm$ 1.8	0.4
Total MC	116671.8 $\pm$ 924.6	
Data	126614	

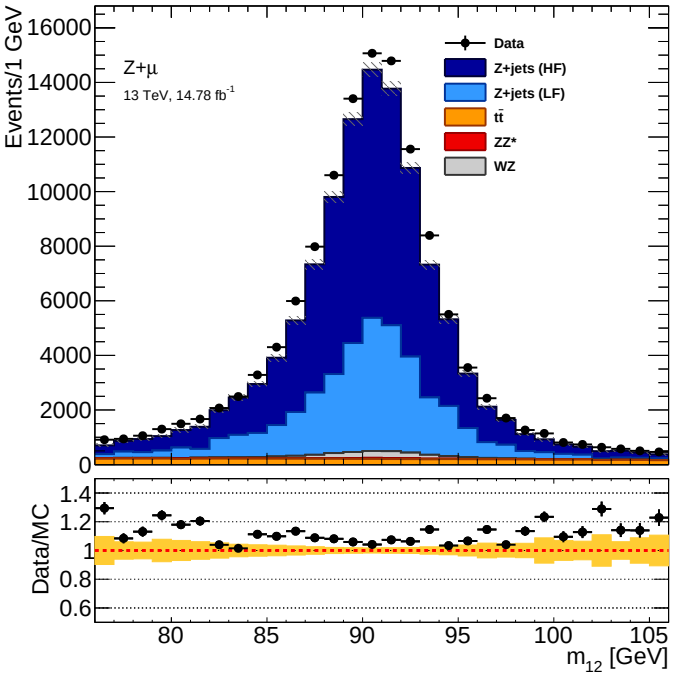

Figure 5.4: The expected and observed invariant mass (m_{12}) distribution of the Z boson candidates selected in $Z + \mu$ events at an integrated luminosity of 14.78 fb^{-1}. The lower panel shows the ratio between data and MC expectation. The total statistical MC uncertainty is shown as a yellow band while error bars are the observed statistical errors.

As expected, the main contribution originates from the Z + HF production (62%) and Z + LF (31%). A much smaller contribution ($\approx$ 5%) originates from $t\bar{t}$ events. The diboson WZ production contributes with only about 1.8% and the contribution of the irreducible ZZ^* background is below 1%.
The numbers of expected events is underestimated by about 8% with respect to the data. Since the shapes of the expected and observed m_{12} distributions are in a good agreement, the discrepancy can be associated to the background normalisation. Thus, the observed difference should have no direct impact on the comparison of the isolation and d_0 significance selection efficiencies between data and MC simulation. The efficiencies, ϵ^{μ}, of the additional muon to pass the d_0 significance and/or the lepton isolation cut is given as

$$\epsilon^{\mu} = \frac{N_{\mu}^{total}(\text{after cut}) - N_{\mu}^{MC}(\text{after cut})}{N_{\mu}^{total}(\text{before cut}) - N_{\mu}^{MC}(\text{before cut})}, \tag{5.5}$$

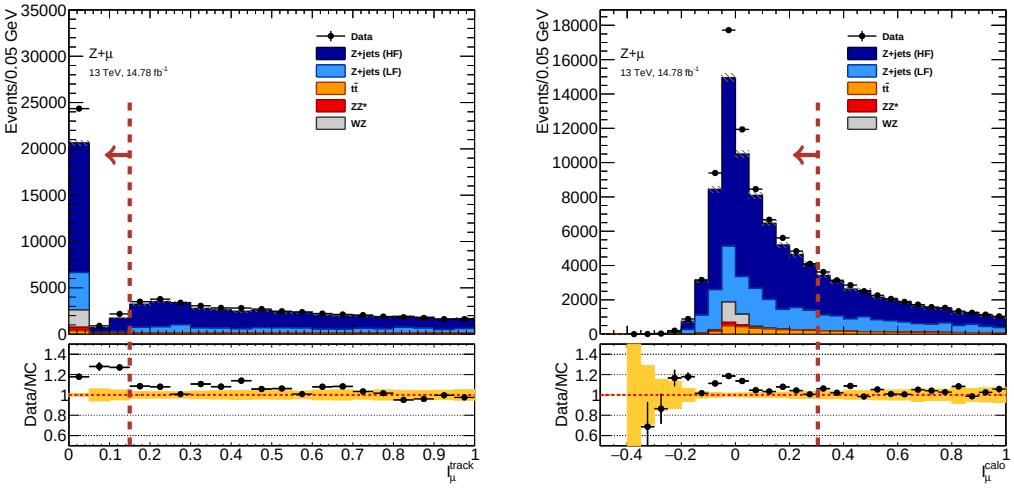

(a) (b)

Figure 5.5: Distribution of (a) the track and (b) calorimeter isolation variables for the additional muon in $Z + \mu$ events at an integrated luminosity of 14.78 fb^{-1}. The lower panel shows the ratio between data and MC expectation. The total statistical MC uncertainty is shown as a yellow band while error bars are the observed statistical errors.

where N_{μ}^{total} is the total number of $Z + \mu$ events. The ZZ^* and WZ contribution, N_{μ}^{MC}, is determined from simulation and subtracted from the total number, since the additional muons in the in these processes originate from prompt W and Z decays, rather than from jets.
The distribution of the track and calorimeter isolation for the additional muon in $Z + \mu$ events is shown in Figure 5.5. Except for small discrepancies for track and calorimeter isolation values around zero, the data and the MC simulation agree within the statistical uncertainties. Table 5.5 shows the expected and observed number events after the cut on the d_0 significance and isolation variables. The cut values are the same as for signal selection (Section 5.4).
The efficiencies are given in Table 5.6. According to the definition of the fake factors for the extrapolation from the *"inverted isolation CR"*, the muon isolation efficiencies are calculated with respect to the number of expected events after the d_0 significance cut, i.e. N_{μ}^{total}(before cut) corresponds to the first column and N_{μ}^{total}(after cut) to the last column of Table 5.5.

Table 5.5: The expected and observed number of $Z + \mu$ events at an integrated luminosity of 14.78 fb^{-1} after applying the d_0 significance and isolation cuts on the additional muon. The errors represent the statistical uncertainties.

Selection applied	d_0 significance		Isolation		d_0 significance+ isolation	
Z + HF	39643.4	± 171.1	14003.7	± 105.6	8132.0	± 80.3
Z + LF	31939.6	± 630.2	3746.7	± 197.6	3321.1	± 193.2
$t\bar{t}$	2421.9	± 15.2	426.3	± 6.3	260.6	± 5.0
WZ	1990.3	± 15.4	1691.6	± 15.3	1895.8	± 15.0
ZZ^*	328.1	± 1.7	372.3	± 1.7	346.0	± 1.7
Total MC	76323.3	± 833.7	20240.5	± 326.6	13955.4	± 295.1
Data	80046		24423		16693	

Table 5.6: Efficiency of muon selection after the d_0 significance and isolation cuts for an additional muon in $Z + \mu$ events.

Selection applied	Data [%]	MC [%]
d_0 significance	63.5 ± 0.4	65.2 ± 1.4
isolation	18.7 ± 0.2	15.8 ± 0.5
d_0 significance + isolation	11.8 ± 0.2	10.3 ± 0.3

The measured efficiency of the d_0 significance cut is in good agreement with simulation, while for the isolation cut a difference of more than 10% is observed between data and simulation. In order to study this discrepancy in more detail the $Z + \mu$ components with muons from heavy and light flavour jets are studied separately, while the heavy flavour jet region also includes the contribution of $t\bar{t}$ production.

5.5.2.1 Selection Efficiency for Muons from Heavy Flavour Jets

The fake factors applied to the $\ell\ell + \mu\mu$ reducible background are determined from simulated Z+jet events with muons from two or more heavy flavour jets. The $Z + \mu$ events with one muon from heavy flavour jets (Z + HF) can be used to validate the simulation against data.

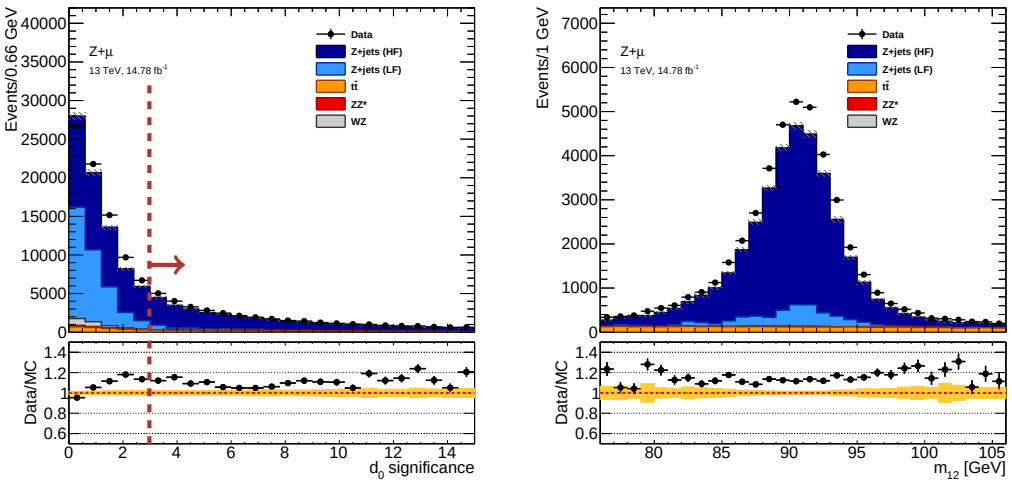

(a) (b)

Figure 5.6: Distribution of the (a) d_0 significance of the additional muon in $Z + \mu$ events and (b) invariant mass of the Z boson candidate requiring $|d_0/\sigma_{d_0}| > 3$ at an integrated luminosity of 14.78 fb^{-1}. The lower panel shows the ratio between data and MC expectation. The total statistical MC uncertainty is shown as a yellow band while error bars are the observed statistical errors.

The muon tracks emerging from heavy hadron decays are characterised by a large d_0 significance. Figure 5.6(a) shows the distribution of the d_0 significance of the additional muon track in the selected $Z + \mu$ events. The cut $|d_0/\sigma_{d_0}| > 3$ selects predominately the $Z +$ HF component, as also be seen from the distribution of the di-lepton invariant mass of the Z boson candidates (Figure 5.6(b)).
After the d_0 significance cut, the $Z + \mu$ events are composed of 90% $Z +$ HF and only 10% $Z +$ LF events. The ZZ^* and WZ contributions are almost negligible. Similarly as in Figure 5.4, the MC simulation underestimates data, while the shapes of the distribution are in a good agreement.

In Figure 5.7 the distribution of the track and calorimeter isolation variables are shown for the additional muons in heavy flavour enriched ($|d_0/\sigma_{d_0}| > 3$) $Z + \mu$ sample. The shapes of the simulated the distributions are in a good agreement with data except for the track and calorimeter isolation values around zero, as also seen in Figure 5.5.
The expected and observed number of events in the heavy flavour enriched $Z + \mu$ sample and events remaining after applying the isolation requirement are shown in Table 5.7. The by far most dominant process in this samples is the $Z +$ HF, allowing

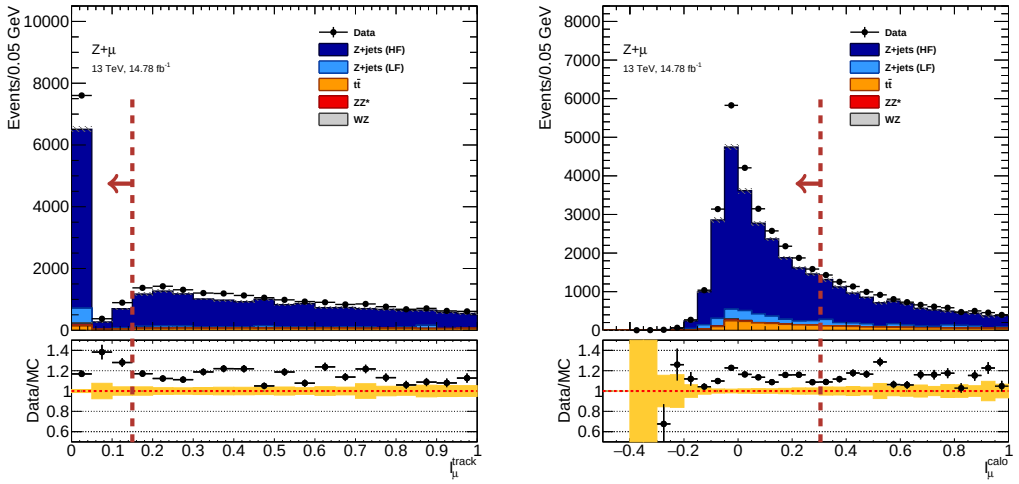

(a) (b)

Figure 5.7: Distribution of (a) the track and (b) calorimeter isolation variables for the additional muon in heavy flavour $Z + \mu$ events at an integrated luminosity of 14.78 fb^{-1}. The lower panel shows the ratio between data and MC expectation. The total statistical MC uncertainty is shown as a yellow band while error bars are the observed statistical errors.

Table 5.7: Expected and observed number of events for $\mathcal{L} = 14.78$ fb^{-1} in the heavy flavour enriched $Z + \mu$ sample ($|d_0/\sigma_{d_0}| > 3$) before and after the isolation cut on the additional muon. The errors are statistical uncertainties only.

Selection applied	$\|d_0/\sigma_{d_0}\| > 3$		Isolation	
$Z + \mathrm{HF}$	32398.4	$\pm$ 152.1	5871.7	$\pm$ 68.6
$Z + \mathrm{LF}$	3545.6	$\pm$ 157.4	425.6	$\pm$ 41.5
$t\bar{t}$	3498.5	$\pm$ 18.0	165.7	$\pm$ 4.0
WZ	79.8	$\pm$ 3.1	65.8	$\pm$ 2.8
ZZ^*	31.4	$\pm$ 0.5	26.3	$\pm$ 0.4
Total MC	39553.3	$\pm$ 331.1	6555.0	$\pm$ 117.4
Data	44925		7730	

for the study of muon properties for muon produced in decays of *b*- and *c*-hadrons. In Table 5.8 the corresponding isolation efficiencies are shown after subtracting the ZZ^* and WZ contribution based in MC prediction.

Table 5.8: Isolation efficiencies for the additional muon in the heavy flavour enriched $Z + \mu$ sample.

Selection applied	Data [%]	MC [%]
isolation	17.0 ± 0.2	16.4 ± 0.3

There is a good agreement of the simulated and measured isolation efficiencies for muons from heavy flavour jets with a relative discrepancy below 4%.

5.5.2.2 Selection Efficiencies for Muons from Light Flavour Jets

The isolation efficiencies determined from simulated Z + HF are also assumed for the extrapolation of the Z + LF contribution of the *"inverted isolation CR"* into the signal region. The assumption that the isolation efficiency is the same for muons from heavy flavour and light flavour jets can be tested with $Z + \mu$ events which are enriched with light flavour jets, i.e. with muons from π and K decays.

The light flavour enriched sample is obtained by means of the so-called momentum balance requirement. The momentum balance of a given muon track is defined as a difference between the muon p_T measured in the ID and in the MS, relative to the former muon p_T value,

$$\delta = \frac{p_T^{\mathrm{ID}} - p_T^{\mathrm{MS}}}{p_T^{\mathrm{ID}}}. \tag{5.6}$$

Since the muons from in-flight decays of π and K are detected only in the MS, while the original π or K is detected in the ID, the corresponding muon momentum balance of such muons is expected to be on average larger than zero, as opposed to the muons detected in both sub-detectors. This can be seen in Figure 5.8(a).
For $\delta > 0.1$, the Z + LF process has the dominate contribution. Figure 5.8(b) shows the di-lepton invariant mass distribution of the Z boson candidates after the cut $\delta > 0.1$ on the momentum balance. The data and the MC simulation are in a good agreement within relatively large uncertainties caused by the low number of MC events in that region.

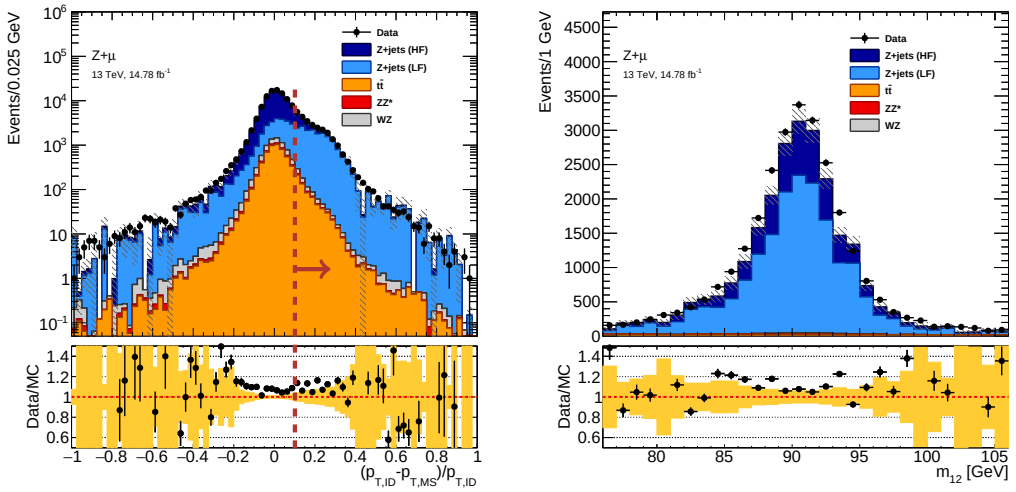

(a) (b)

Figure 5.8: (a) Momentum balance $\delta = \left(p_T^{\mathrm{ID}} - p_T^{\mathrm{MS}}\right) / p_T^{\mathrm{ID}}$ for the additional muon in $Z + \mu$ events and (b) the invariant di-lepton mass of the Z boson candidates in events with additional muons satisfying $\delta > 0.1$ at an integrated luminosity of 14.78 fb^{-1}. The lower panel shows the ratio between data and MC expectation. The total statistical MC uncertainty is shown as a yellow band while error bars are the observed statistical errors.

Table 5.9 shows the number of observed and expected events in the light flavour enriched $Z + \mu$ sample.

Table 5.9: Expected and observed number of events for $\mathcal{L} = 14.78$ fb^{-1} in the light flavour jet enriched $Z + \mu$ sample. Errors are the statistical uncertainties only.

Sample	Events			Contribution [%]
$Z + \mathrm{HF}$	6257.4	$\pm$	67.98	25.3
$Z + \mathrm{LF}$	17586.8	$\pm$	474.46	71.1
$t\bar{t}$	673.3	$\pm$	8.20	2.8
WZ	188.0	$\pm$	4.69	0.8
ZZ^*	38.2	$\pm$	0.54	0.2
Total MC	24743.7	$\pm$	555.9	
Data	27388			

The purity of 71% is reached in the Z + LF component, with a Z + HF (including $t\bar{t}$) contribution of 21%. Contributions from WZ and ZZ^* processes are below 1%.

The distribution of the track and calorimeter isolation variables in these events are shown in Figure 5.9.

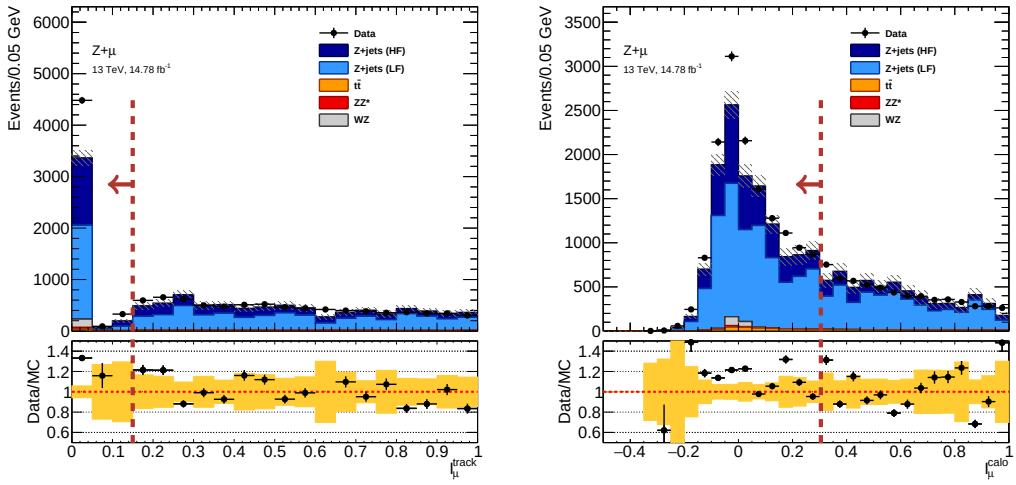

(a) (b)

Figure 5.9: Distribution of the (a) track and (b) calorimeter isolation variables for the additional muon in light flavour enriched $Z + \mu$ events at an integrated luminosity of 14.78 fb^{-1}. The lower panel shows the ratio between data and MC expectation. The total statistical MC uncertainty is shown as a yellow band while error bars are the observed statistical errors.

Data and MC simulation agree well, except for the track and calorimeter isolation values around zero, where the MC simulation underestimates the data.
The expected and observed number of events after the d_0 significance and the isolation cut on the additional muon are given in Table 5.10.
The corresponding cut efficiencies are shown in Table 5.11. Since the isolation efficiencies for muons from Z + LF and Z + HF should be compared, the isolation efficiency is calculated with respect to the number of events after the d_0 significance cut, i.e. N_μ^{total}(before cut) corresponds to the first column and N_μ^{total}(after cut) to the last column in Table 5.10.

Table 5.10: Expected and observed number of events for $\mathcal{L} = 14.78$ fb^{-1} in the light flavour jet enriched $Z + \mu$ sample after applying the d_0 significance and isolation cuts on the additional muon. Errors show the statistical uncertainties of the MC simulation.

Selection applied	d_0 significance	Isolation	d_0 significance+ isolation
$Z +$ HF	3550.8 $\pm$ 51.1	1268.3 $\pm$ 32.1	759.0 $\pm$ 24.6
$Z +$ LF	16553.4 $\pm$ 466.2	1649.1 $\pm$ 133.1	1590.6 $\pm$ 132.1
$t\bar{t}$	330.0 $\pm$ 5.8	39.3 $\pm$ 2.0	25.0 $\pm$ 1.8
WZ	181.4 $\pm$ 4.6	169.7 $\pm$ 4.5	165.35 $\pm$ 4.4
ZZ^*	35.5 $\pm$ 0.5	32.8 $\pm$ 0.5	30.75 $\pm$ 0.5
Total MC	20651.1 $\pm$ 528.3	3159.2 $\pm$ 172.2	2570.6 $\pm$ 163.1
Data	22311	4338	3538

Table 5.11: The efficiency of the d_0 significance and isolation cuts on the additional muons in the light flavour enriched $Z + \mu$ events.

Selection applied	Data [%]	MC [%]
d_0 significance	81.4 ± 0.7	83.4 ± 2.8
isolation	15.1 ± 0.3	11.6 ± 0.9
d_0 significance + isolation	12.3 ± 0.2	9.70 ± 0.7

The efficiency of the d_0 significance cut are comparable in data and MC simulation, but the measured isolation efficiency in data is more than 30% higher than the one determined in simulation. The number of simulated $Z +$ LF events is low, resulting in a rather large statistical uncertainties.

The comparison of the isolation efficiencies for muons from light and heavy jets are summarised in Table 5.12.

Table 5.12: Comparison of the isolation efficiencies for the additional muon in the light flavour enriched and heavy flavour enriched $Z + \mu$ sample.

Selection applied	Data [%]	MC [%]
isolation ($Z +$ LF)	15.1 ± 0.3	11.6 ± 0.9
isolation ($Z +$ HF)	17.0 ± 0.2	16.4 ± 0.3

The measured isolation efficiencies agree with 10% between the light and heavy flavour component. The difference is of the same order as the difference between data and MC simulation in the heavy flavour enriched $Z + \mu$ sample. This justifies the assumption that the $Z +$ HF fake factors can be applied to the $Z +$ LF component. The discrepancy between the data and MC simulation is assigned as a systematic uncertainty for the fake factors.

5.5.3 Estimation of the Reducible $\ell\ell + ee$ Background

The estimation of the reducible $\ell\ell + ee$ background is performed in a similar way as for $\ell\ell + \mu\mu$ background. A detailed description can be found in Ref. [87].
Two CR are built, one for light flavour jets misidentified as electrons (denoted as *"CR_f"*) and one for photon conversions (denoted as *"CR_γ"*). The background from semi-leptonic decays of heavy flavour hadrons (denoted as *"CR_q"*) is estimated from MC simulation. In contrast to the $\ell\ell + \mu\mu$ background estimation, the WZ component is not negligible anymore and its normalisation is therefore left as free parameter in the combined fit. Table 5.13 shows the fitted event yields in the CR, and the corresponding fake factors and the yields in the SR.

Table 5.13: Fitted $\ell\ell + ee$ event yields at $\mathcal{L} = 14.78\,\text{fb}^{-1}$ in the *"CR_f"*, *"CR_γ"* and *"CR_q"* control regions. The corresponding fake factors and the expected event yields in the SR are shown in addition. The statistical and in SR also the systematic uncertainties are given. [87].

Background	Fitted yield in CR	Fake Factor [%]	Yield in SR
CR_f	1228 ± 35	0.23 ± 0.03	$2.62 \pm 0.08 \pm 0.36$
CR_γ	79 ± 10	0.76 ± 0.05	$0.55 \pm 0.08 \pm 0.04$
CR_q	(MC based estimation)		2.5 ± 0.77

5.6 Results of the $H \to ZZ^* \to 4\ell$ Event Selection

The observed and expected distribution of the four lepton invariant mass $m_{4\ell}$ after the full event selection is shown in Figure 5.10.

The expected SM Higgs boson signal with $m_H = 125$ GeV and the irreducible ZZ^* background as well as the background from $t\bar{t}V$ and tri-bosons are obtained from MC simulation. The yields of the reducible Z+jets and $t\bar{t}$ background components are determined from control data (Section 5.5). The total yield of the reducible

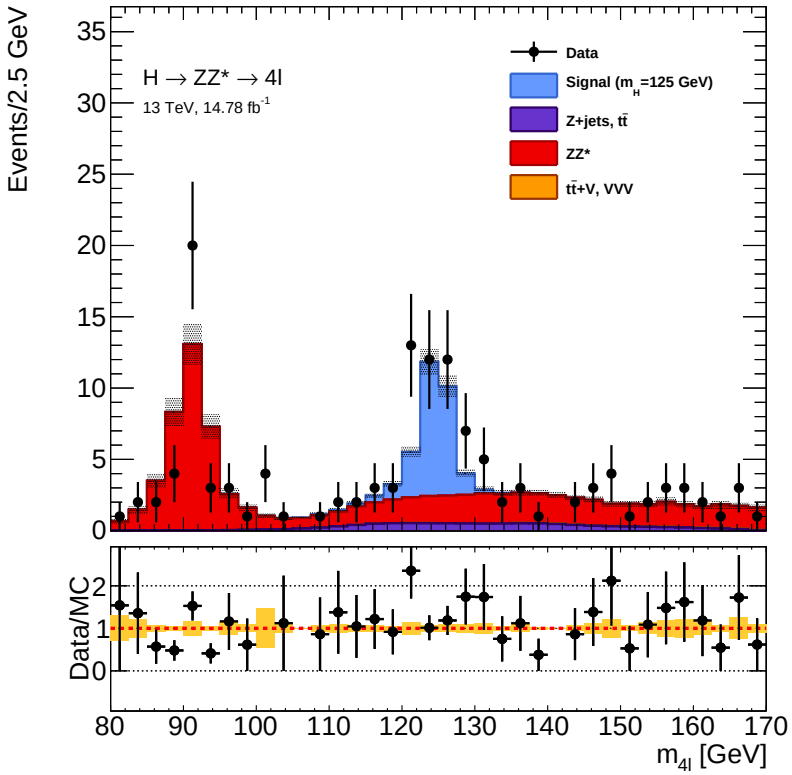

Figure 5.10: The expected and observed invariant mass distribution for the selected Higgs boson candidate four lepton events at an integrated luminosity of 14.78 fb^{-1}. The signal corresponds to the SM Higgs boson with $m_H = 125$ GeV. The lower panel shows the ratio between data and MC expectation. The statistical and systematically MC uncertainty are shown as a yellow band while error bars are the observed statistical errors.

Z+jets and $t\bar{t}$ background is scaled to account for small contributions from WZ events. The data and the MC simulation agree well, except at the Z boson peak, since the modelled di-lepton mass resolution underestimates the resolution in data. Figure 5.11 shows the invariant masses of the on- and off-shell Z boson, m_{12} and m_{34} in the mass window 118 GeV $< m_{4\ell} <$ 129 GeV.

The expected and observed number of events in the $m_{4\ell}$ window between 118 and 129 GeV for the all final states (4μ, $2e2\mu$, $2\mu2e$ and $4e$) are given in Table 5.14.

Table 5.14: Expected and observed number of events at $\mathcal{L} = 14.78$ fb^{-1} after the full event selection in the four-lepton final states (4μ, $2e2\mu$, $2\mu2e$ and $4e$). Only events in the mass range 118 GeV $< m_{4\ell} <$ 129 GeV are considered. In addition, the signal to background ratios (S/B) are shown.

Final state	Signal	ZZ^*	Z+jets, $t\bar{t}$ $t\bar{t}V, VVV, WZ$	S/B	Total expected	Total observed
4μ	8.2 ± 0.8	3.11 ± 0.28	0.31 ± 0.04	2.4	11.6 ± 1.1	16
$2e2\mu$	5.5 ± 0.5	2.19 ± 0.21	0.30 ± 0.04	2.0	8.0 ± 0.8	12
$2\mu2e$	4.4 ± 0.4	1.39 ± 0.13	0.46 ± 0.05	2.4	6.3 ± 0.6	10
$4e$	4.2 ± 0.4	1.46 ± 0.18	0.47 ± 0.07	2.2	6.1 ± 0.7	6
Sum (4ℓ)	22.3 ± 2.1	8.15 ± 0.80	1.54 ± 0.20	2.3	32.0 ± 3.2	44

The uncertainties include the statistical error from MC simulation and the systematic uncertainties. The systematic uncertainties on the event yield due to the uncertainty on the measurement of the muon (electron) identification efficiency is estimated to be 1.2% (0.9%), while the uncertainty from the measurement of the lepton energy scale and resolution is negligible. The uncertainty on the integrated luminosity is 3.3% for the 2015 and 3.7% for the 2016 data. For the reducible background the systematical error is determined in the data-driven estimation and is found to be 14% for the muon and electron background. Theoretical systematic uncertainty on the ZZ^* background cross section is given by the uncertainty on the factorisation and renormalisation scale (5%) and on the PDF and α_s (5%). The largest theoretical systematic uncertainty of 8.1% is associated to the ggF production. Furthermore, the uncertainty on the Higgs boson branching ratio is 2.2% [87].

The signal to background (S/B) ratio is found to be approximately 2.2 in each 4ℓ category. In all categories, except $4e$, an excess of events above the expected background is observed. In total 44 Higgs boson candidates are observed while the prediction from simulation (including signal) is 32.0 ± 3.2. A detailed list of the observed four-lepton candidates can be found in Appendix C.

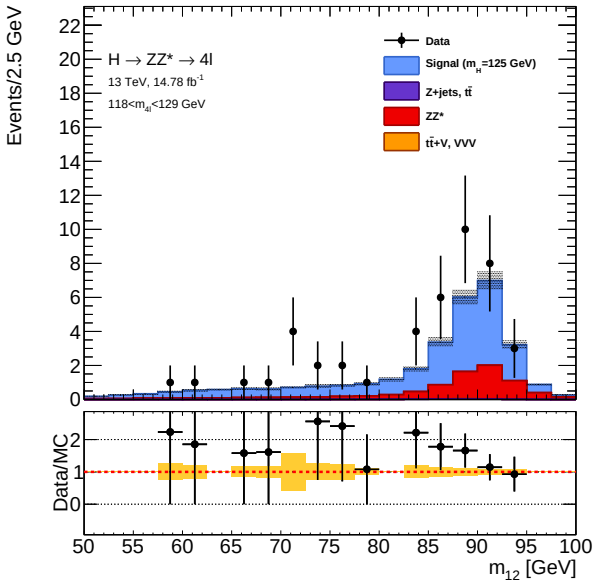

(a)

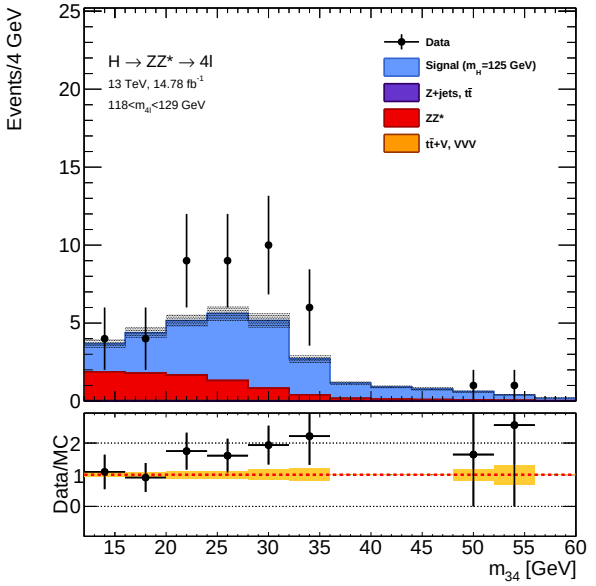

(b)

Figure 5.11: Invariant mass of the (a) leading and (b) sub-leading di-lepton pair for the four-lepton events in the mass window 118 GeV $< m_{4\ell} <$ 129 GeV at an integrated luminosity of 14.78 fb^{-1}. The lower panel shows the ratio between data and MC expectation. The statistical and systematically MC uncertainty are shown as a yellow band while error bars are the observed statistical errors.

The corresponding measured cross section is

$$\sigma_{\text{tot}}(pp \rightarrow H \rightarrow ZZ^* \rightarrow 4\ell) = 81^{+18}_{-16}\ \text{pb} \tag{5.7}$$

compared to the expected SM value of $\sigma^{SM}_{\text{tot}} = 55.5^{+3.8}_{-4.4}$ pb. The compatibility between the measured value and the SM predication is at the level of 1.6 standard derivations [87].

Chapter 6

Measurement of the Tensor Structure of the HZZ Tensor Coupling

6.1 Introduction

The $H \to ZZ^* \to 4\ell$ decay channel allows for the measurement of the Higgs boson spin and the tensor structure of the Higgs boson coupling to Z bosons (HZZ). Current experimental results [4, 5] indicate that the discovered Higgs boson is a spin-0 particle with the dominant tensor structure term corresponding to the SM CP-even HZZ coupling.
Furthermore, the tensor structure of the HZZ coupling can be probed for possible small admixtures of anomalous (BSM) contributions. Both the CP-even and CP-odd BSM coupling contributions can be considered. The existence of the latter ones would lead to a CP-violation in the Higgs sector.
First limits on BSM coupling parameters are set with Run I data, based on the kinematic properties of Higgs boson decay products in the $H \to ZZ^* \to 4\ell$ channel. In this thesis, the measurement is performed on Run II data, taking into account the BSM-sensitive Higgs boson production rates in different production modes.
The studies of BSM HZZ coupling contributions in this thesis are performed with the Higgs characterisation EFT model introduced in Section 3.5, assuming a spin-0 nature of the discovered Higgs boson. The CP-even (κ_{HZZ}) and CP-odd (κ_{AZZ}) BSM coupling parameters in Equation 3.3 are probed under the assumption that these are fully correlated to the corresponding couplings to W bosons (κ_{HWW}, κ_{AWW}).
In the following, the observables sensitive to BSM coupling contributions are introduced in Section 6.2. Subsequently, the modelling of the Higgs boson signal in dependence on the CP-even and CP-odd BSM coupling parameters is introduced and validated in Section 6.3. Based on the measurements of the event rates in each category, limits are set on the BSM coupling parameters (Section 6.4).

6.2 Observables Sensitive to BSM Contributions in the HZZ Vertex

6.2.1 Event Categorisation based on Production Modes

The presence of these BSM contributions strongly effects the production rates in different Higgs boson production modes. For the $H \to ZZ^* \to 4\ell$ channel, only the two most dominant production modes (ggF and VBF) can be measured with current data. The dependence of the corresponding production rates on the size of CP-even and CP-odd BSM coupling parameters is shown in Figure 6.1.

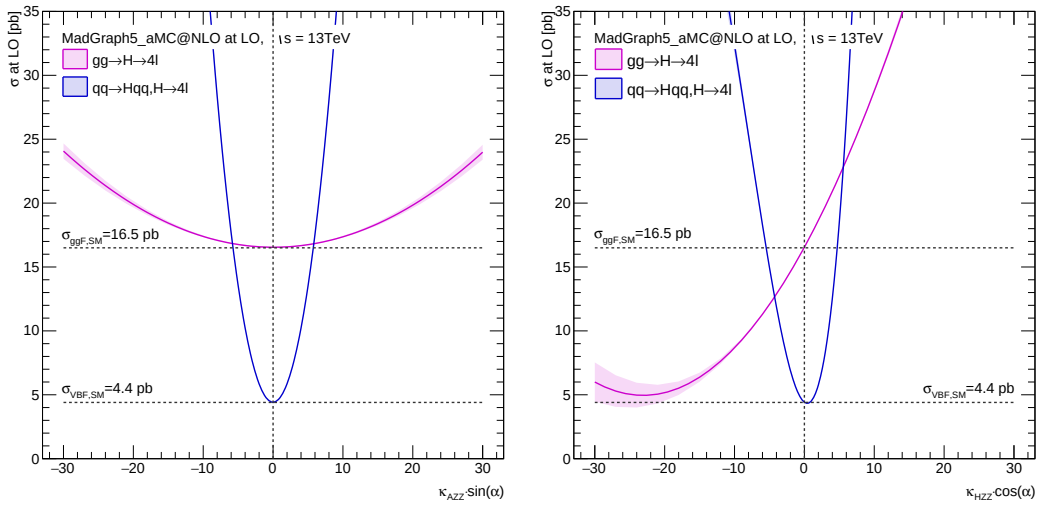

(a) (b)

Figure 6.1: Cross section for the ggF and VBF Higgs boson production mode in the $H \to ZZ^* \to 4\ell$ decay channel as a function of the BSM coupling parameters (a) $\kappa_{AZZ} \cdot \sin(\alpha)$ and(b) $\kappa_{HZZ} \cdot \cos(\alpha)$.

Both the ggF and VBF production rates increase with increasing absolute values of κ_{XZZ} parameters. The VBF rate increases much more steeply ($\propto \kappa^4_{XZZ}$) than the ggF rate ($\propto \kappa^2_{XZZ}$), because the HZZ BSM coupling contributes in both, VBF production and $H \to ZZ$ decay vertices.
In case of the CP-odd BSM coupling, the VBF and ggF production rates are distributed symmetrically around the SM point $\kappa_{SM} = 0$, and are thus not sensitive to the sign of the κ_{AZZ} parameter. In contrast, there is a sensitive to the sign of the higher-order CP-even contributions due to interference with the SM CP-even coupling term. Therefore, as can be seen in Figure 6.1(b), the cross sections are not symmetric, especially in the case of ggF production.

In order to use measure separately the signal production in different production modes, the selected events are classified into several categories based on the properties of final state products related to the production vertex. The events are selected following the standard $H \to ZZ^* \to 4\ell$ event selection, described in Section 5.4. Events in the four-lepton mass range 118 GeV $< m_{4\ell} <$ 129 GeV around the Higgs boson mass are considered [87]. These events are then categorised according to the number of jets and additional leptons. A schematic overview of the event categories is shown in Figure 6.2.

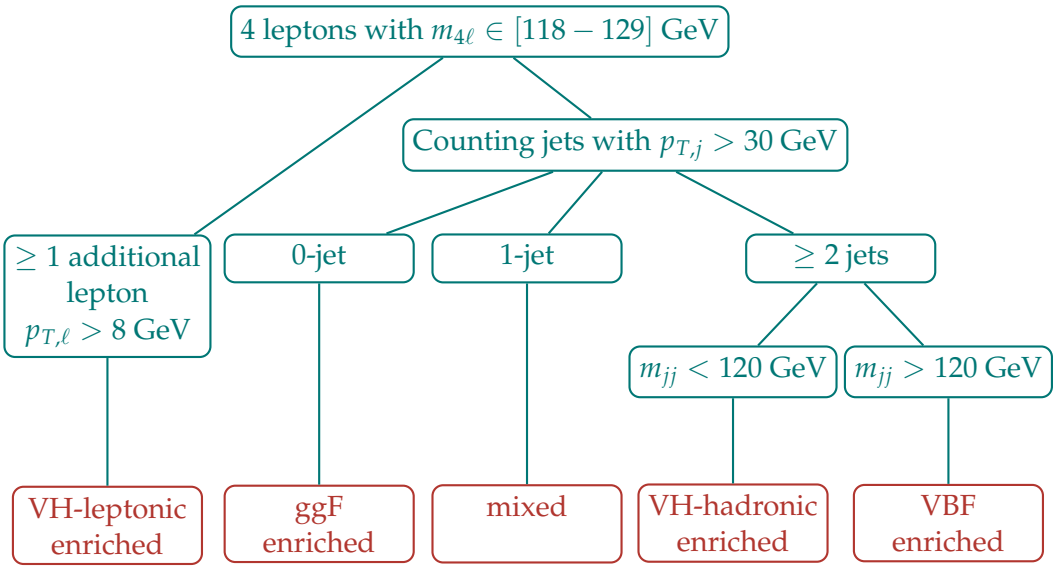

Figure 6.2: Schematic overview of the event categories sensitive to different Higgs boson production modes in the decay channel $H \to ZZ^* \to 4\ell$ [87].

At first, the events in a so-called *"VH-leptonic"* category are selected by requiring at least one isolated lepton with $p_{T,\ell} > 8$ GeV in addition to the four leptons originally selected as Higgs boson candidate quadruplet. Such leptons most likely originate from leptonic decays of Z or W bosons produced in the VH production mode (VH_{lep}). Thus the VH_{lep} production mode is expected to be enriched in this category. Events that do not fall into the *"VH-leptonic"* category are further sub-divided according to the number of jets, with $p_{T,j} > 30$ GeV in the final state.
The events with no jets most likely originate from the gluon-fusion production mode. This corresponds to the *"ggF enriched"* category.
The events with exactly one jet, the so-called *"mixed"* category, also most likely originate from the gluon-fusion process, but there are also larger contributions from all other production modes.

For events with two or more jets in the final state, there is a large fraction produced via VBF or VH mode, where the vector boson in the latter one decays hadronically (VH_{had}). In order to further separate the two, events are in addition separated according to the invariant mass m_{jj} of the two leading jets. To select the Higgs bosons that are predominantly produced in association with hadronically decaying vector bosons, one requires $m_{jj} < 120$ GeV, since the mass of the Z and W bosons are slightly below this value. This category is referred to as *"VH-hadronic"* category. As the Higgs boson production via vector boson fusion is characterised by two highly energetic jets (Section 3.2), this production mode can be enhanced requiring $m_{jj} > 120$ GeV. Events satisfying this requirement belong to the *"VBF enriched"* category.

The expected relative contributions of SM Higgs boson events from production mode is shown in every event category in Table 6.1.

Table 6.1: Contribution of Higgs boson production modes at the LHC at a centre-of-mass energy of $\sqrt{s} = 13$ TeV in the respective categories separating $H \to ZZ^* \to 4\ell$ events per production mode.

Event	Signal production mode				
category	ggF	VBF	WH	ZH	$\bar{t}tH$
ggF enriched	97.99%	1.06%	0.42%	0.53%	0.00%
mixed	87.28%	9.14%	2.13%	1.42%	0.01%
VH-hadronic	74.19%	6.14%	10.40%	7.40%	1.87%
VBF enriched	60.44%	31.79%	2.55%	1.79%	3.41%
VH-leptonic	7.68%	1.64%	50.19%	7.83%	32.66%
Total	87.94%	7.75%	2.12%	1.43%	0.77%

The gluon-fusion process is dominant in all categories except for the *"VH-leptonic"*, since it has the highest cross section and additional jets can be produced as the initial state radiation. The largest purity is reached in the *"ggF enriched"* category with the relative ggF contribution of about 98%. A high enrichment of the VH mode (about 58%) is also reached in the *"VH-leptonic"* category. In the *"VBF enriched"* the purity of the VBF contribution is about 32%, while in the *"VH-hadronic"* category the VH events are selected with a purity of 18%.

6.2.2 Kinematic Properties of Final State Products

The tensor structure of the HZZ coupling can also be studied via kinematic properties of Higgs boson decay products [39]. Due to the fully reconstructed four-lepton final state in the $H \to ZZ^* \to 4\ell$ decay channel, all production and decay angles can be measured, yielding CP-sensitive information.

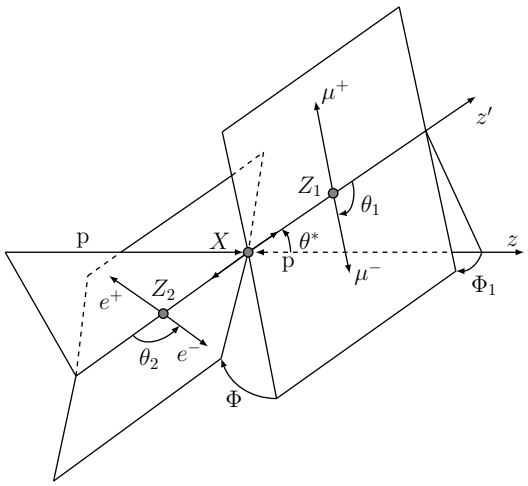

Figure 6.3: Illustration of the production and decay angles in the $H \to ZZ^* \to 4\ell$ decay channel [38].

These angles are illustrated in Figure 6.3, with the following definitions:

- θ_1 (θ_2) is the angle between the negatively charged lepton from the decay of the on-shell (off-shell) Z boson in the direction of flight of the respective Z boson,
- Φ is the angle between the two decay planes spanned by the di-lepton pairs in the four-lepton rest frame,
- Φ_1 is the angle between the direction of the momentum of the on-shell Z boson and the decay plane spanned by its decay products,
- and θ^* is the production angle of the on-shell Z boson.

Since the Higgs boson mass $m_H = 125$ GeV is below twice the mass of the Z boson, the distribution of the mass of each di-lepton pair, m_{12} and m_{34}, is also sensitive to parity.

6.3 Signal Model Construction

In order to study the tensor coupling of the Higgs boson to vector bosons a dedicated signal model is needed, describing the CP-sensitive observables in dependence on BSM coupling parameters. In the following, the so-called morphing signal modelling method is introduced (Section 6.3.1). The method allows for the signal prediction in each point on the BSM parameter space, based on a fixed number of input BSM Monte Carlo samples. The input samples are described in Section 6.3.2 and the validation of the modelling method is presented in Section 6.3.3.

6.3.1 Signal Modelling via the Morphing Method

The construction of the signal model is based on a morphing method [88], providing the modelling of event yields and distributions of the CP-sensitive observables continuously in a multidimensional space of coupling parameters $\vec{g} = (g_{SM}, g^1_{BSM}, \ldots, g^n_{BSM})$, where $g_{BSM} = f(\kappa_{XVV}, \alpha, \Lambda)$.
The event rate or distribution of a given observable, T_{target}, at an arbitrary point in the coupling parameter space $\vec{g}_{\text{target}}$ can be described as a linear combination of a fixed number of the corresponding input rates or distributions $T_{\text{i}}(\vec{g}_i)$ obtained from MC simulation

$$T_{\text{target}}\left(\vec{g}_{\text{target}}\right) = \sum_{i=1}^{N} w_i\left(\vec{g}_{\text{target}}; \vec{g}_i\right) T_{\text{i}}\left(\vec{g}_i\right). \tag{6.1}$$

The coupling configurations $\vec{g}_i$ have to be carefully chosen in order to span the full multidimensional parameter space. The input samples are normalised to their respective cross section. The contribution of each input sample is defined by a weight function $w_i\left(\vec{g}_{\text{target}}; \vec{g}_i\right)$, which depends on the input target values of coupling parameters, $\vec{g}_{\text{target}}$ and $\vec{g}_i$, respectively. The weight function is determined under the assumption, that the event rate or the kinematic distribution are proportional to the squared matrix element of the studied process,

$$T\left(\vec{g}\right) \propto \left|\mathcal{M}\left(\vec{g}\right)\right|^2. \tag{6.2}$$

The matrix element $|\mathcal{M}\left(\vec{g}\right)|$ can be factorised as a linear sum of the products of couplings parameters g_α and the corresponding operators $\mathcal{O}(g_\alpha)$,

$$|\mathcal{M}(\vec{g})|^2 = \underbrace{\left(\sum_{\alpha\in p,s} g_\alpha \mathcal{O}(g_\alpha)\right)^2}_{\text{production}} \cdot \underbrace{\left(\sum_{\alpha\in d,s} g_\alpha \mathcal{O}(g_\alpha)\right)^2}_{\text{decay}}, \tag{6.3}$$

where couplings appearing only in production, only in decay, and shared in production and decay, are denoted with p, d and s, respectively.
Therefore, the weights w_i are function of target couplings,

$$w_i = \sum_{\alpha,\beta,\gamma,\delta=1}^{N} C_{\alpha\beta\gamma\delta} g_\alpha g_\beta g_\gamma g_\delta, \tag{6.4}$$

where $(g_\alpha, g_\beta, g_\gamma, g_\delta) \in g_{\text{target}}$ and the values of coefficients $C_{\alpha\beta\gamma\delta}$ are determined by the values of input couplings $\vec{g}_i (i = 1, \ldots, N)$. By requiring that for each given input samples T_i the corresponding weight value,

$$w_i \left(\vec{g}_{\text{target}} = \vec{g}_i ; \vec{g}_i \right) = 1, \tag{6.5}$$

if $\vec{g}_{\text{target}} = \vec{g}_i$, and

$$w_{j \neq i} \left(\vec{g}_{\text{target}} = \vec{g}_i ; \vec{g}_j \right) = 0, \tag{6.6}$$

for all other input samples T_j, a linear system of equations, called morphing matrix, can be formed. By inverting the morphing matrix the coefficients $C_{\alpha\beta\gamma\delta}$ can be determined.
The number of input distributions N is dependent on the number of couplings in the production and decay vertices and is given as

$$\begin{aligned} N = & \frac{n_p \left(n_p + 1\right)}{2} \cdot \frac{n_d \left(n_d + 1\right)}{2} + \binom{4 + n_s - 1}{4} \\ & + \left(n_p \cdot n_s + \frac{n_s \left(n_s + 1\right)}{2} \right) \cdot \frac{n_d \left(n_d + 1\right)}{2} \\ & + \left(n_d \cdot n_s + \frac{n_s \left(n_s + 1\right)}{2} \right) \cdot \frac{n_p \left(n_p + 1\right)}{2} \\ & + \frac{n_s \left(n_s + 1\right)}{2} \cdot n_p \cdot n_d + \left(n_p + n_d\right) \binom{3 + n_s - 1}{3}, \end{aligned} \tag{6.7}$$

where n_s corresponds to the number of couplings that are shared in production and decay, while n_p (n_d) is the number of couplings only appearing in the production (decay) [88]. The number of input samples needed for the signal modelling in a given BSM coupling parameter space is shown in Table 6.2 for the case of the ggF, VBF or VH Higgs boson production mode and the subsequent $H \to ZZ$ decay. The SM and BSM coupling parameters for the Higgs boson coupling to W bosons are assumed to be fully correlated with corresponding couplings to Z bosons, i.e. $\kappa_{XZZ} = \kappa_{XWW} (X \equiv H, A)$.

Table 6.2: Number of input samples needed for the signal modelling in the BSM coupling parameter space in case of the ggF, VBF and VH Higgs boson production mode with subsequent $H \to ZZ$ decays. The coupling parameters are defined in Equation 3.3 with g_{Hgg} and g_{SM} corresponding to the SM couplings to gluon and vector bosons.

Production mode	Free parameters	production	decay	n_p	n_d	n_s	N
ggF	$\kappa_{AZZ}, \kappa_{HZZ}$	g_{Hgg}	$g_{SM}, \kappa_{AZZ}, \kappa_{HZZ}$	1	3	0	6
VBF+VH	κ_{AZZ}	g_{SM}, κ_{AZZ}	g_{SM}, κ_{AZZ}	0	0	2	5
	κ_{HZZ}	g_{SM}, κ_{HZZ}	g_{SM}, κ_{HZZ}	0	0	2	5

The complete set of N input samples can in general chosen arbitrarily, as long as is allows for an independent set of linear equations for a morphing matrix. However, the statistical accuracy of the target sample will depend on the size of the coupling parameter space covered by the input samples. The statistical uncertainty $\Delta T^{bin}_{\text{target}}$ of the output target distribution $\Delta T^{bin}_{\text{target}}$ in a given bin is given by

$$\Delta T^{bin}_{\text{target}} = \sqrt{\sum_i w_i^2 \left(\vec{g}_{target}; \vec{g}_i\right) N^{bin}_{MC,i}\left(\vec{g}_i\right) \cdot \left(\frac{\sigma_i\left(\vec{g}_i\right)\mathcal{L}}{N_{MC,i}}\right)^2}, \tag{6.8}$$

where $N^{bin}_{MC,i}$ is the number of MC events in a given bin of one input sample i, σ_i is the cross section times branching ratio of that input sample, $\mathcal{L}$ the total integrated luminosity and $N_{MC,i}$ the total number of MC events in the input sample i.

In the following, the generated input samples are introduced. Several complete sets of these samples are studied in order to select the one with minimal statistical uncertainty. Subsequently, the signal model based on this optimal input set is validated for typical BSM observables.

6.3.2 BSM Signal Samples

In order to construct the signal model, several signal samples with different configurations of BSM coupling parameters $\kappa_{AZZ} \cdot \sin(\alpha)$ and $\kappa_{HZZ} \cdot \cos(\alpha)$ have been produced for ggF, VBF and VH production modes. A part of these is to build a set of morphing input samples, while the remaining samples are used for validation purpose.
The samples for the ggF production mode are generated with MadGraph5_aMC@NLO (MG5) [73] at leading-order (NLO) in QCD. The VBF samples are generated with the same generator at leading-order (LO) in QCD. The contribution of the VH

production with hadronic W and Z boson decay is included in these samples. Additional samples are produced with the same generator at LO for the VH production mode with leptonic vector boson decays. The coupling parameters in each signal sample are defined by the Higgs characterisation model (Section 3.5). The parton-level generated events are then interfaced with PYTHIA8 [71] for showering and hadronization. For the simulation of heavy quark decays EVTGEN v1.2.0 [72] is used.

Eight different MC samples are generated for ggF, using configurations of $\{\kappa_{SM}, \kappa_{AZZ}, \kappa_{HZZ}\}$ coupling parameters: one pure SM sample, one pure BSM sample for each of the two BSM coupling parameters, κ_{AZZ} and κ_{HZZ}, with the SM coupling parameter κ_{SM} set to zero, two equivalent samples with $\kappa_{SM} = 1$ and two BSM samples with non-zero values for all three couplings. Summary of all ggF signal samples together with the corresponding coupling parameters is given in Table 6.3. In each of these samples, the value of the coupling parameter $\kappa_{Hgg} \cdot \cos(\alpha)$ for the effective SM coupling to gluons in the production vertex, is set to unity.

Table 6.3: BSM signal samples and the corresponding coupling parameters for the ggF Higgs boson production. The effective coupling at the production vertex is $\kappa_{Hgg} \cdot \cos(\alpha) = 1$. The next-to-leading-order cross sections are shown in the last column.

Sample name	κ_{HZZ}	κ_{AZZ}	κ_{SM}	$\cos(\alpha)$	σ_{ggF} [pb]
`G_kSM1`	0	0	1	1	32.910
`G_kHVV1_kSM0`	1	0	0	1	0.3732
`G_kHVV6_kSM1`	6	0	1	1	46.494
`G_kHVVm6_kSM1`	-6	0	1	1	22.436
`G_kAVV1_kSM0`	0	1	0	$1/\sqrt{2}$	0.0043
`G_kAVV6_kSM1`	0	6	1	$1/\sqrt{2}$	8.4040
`G_kAVVm6_kSM1`	0	-6	1	$1/\sqrt{2}$	8.3872
`G_kHVV6_kAVV6_kSM1`	6	6	1	$1/\sqrt{2}$	11.764
`G_kHVVm6_kAVVm6_kSM1`	-6	-6	1	$1/\sqrt{2}$	5.7936

The location of the coupling configuration in the (κ_{AZZ},κ_{HZZ}) parameter space is shown for each sample in Figure 6.4(a). Samples marked in blue are used as the morphing input for the construction of the signal model. Validation samples are shown in red.

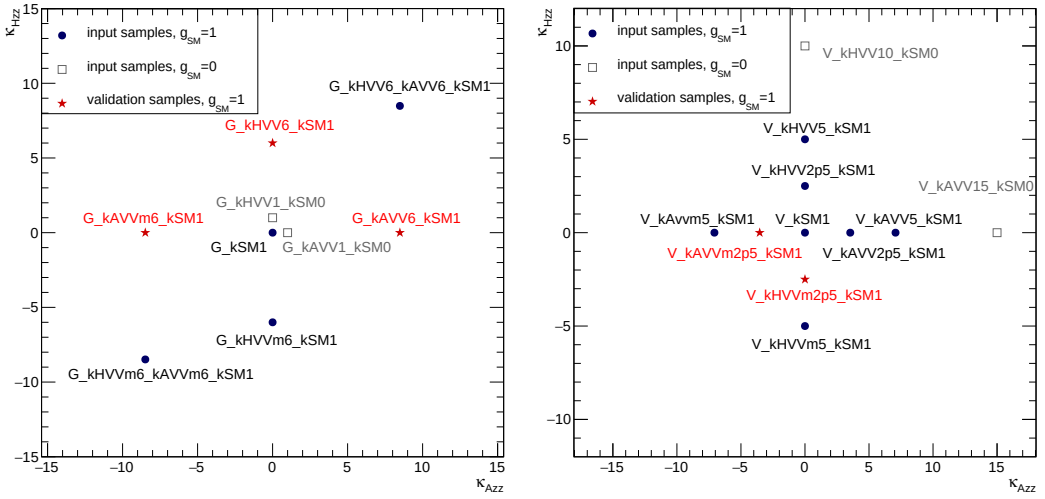

(a) (b)

Figure 6.4: Location of the coupling configurations of each generated sample in the two-dimensional parameter plane (κ_{AZZ},κ_{HZZ}), for samples produced via (a) gluon-fusion and (b) vector boson fusion and VH production.

Since VBF and VH production modes have the same coupling structure, i.e. the HVV coupling in both production and decay, the VBF production is combined with $\mathrm{VH_{had}}$ production into the same signal sample. An additional sample is produced for the $\mathrm{VH_{lep}}$ production. Same configurations of coupling parameters have been used for both types of samples. For each of the coupling parameters, κ_{AZZ} and κ_{HZZ}, five samples have been produced, out of which one is a pure BSM sample with $\kappa_{SM} = 0$. The summary of all VBF+VH signal samples together with the values of the corresponding coupling parameters is given in Table 6.4.
Figure 6.4(b) shows the location of the generated MC signal samples in the $(\kappa_{AZZ}, \kappa_{HZZ})$ parameter space.

In addition to the MG5 SM signal samples `G_kSM1` and `V_kSM1` generated at NLO and LO respectively, there are also corresponding SM samples produced by Powheg (Section 5.3). The latter are considered more accurate due to higher-order corrections. Therefore, the expected number of events in each bin of a given distribution or event category in the MG5 SM is scaled by a scale factor (SF) to the corresponding number of events expected from Powheg MC. The total number of expected events is scaled to the higher-order available prediction [36]. Since no separate BSM samples are produced for the $\mathrm{t\bar{t}H}$ and $\mathrm{b\bar{b}H}$ production mode, the ggF cross section is scaled according to account for these processes. It is assumed, that the same scale factors are also valid for all BSM samples.

Table 6.4: BSM signal samples and the corresponding coupling parameters for the VBF and VH Higgs boson production. The leading-order cross sections are shown in the last column.

Sample name	κ_{Hvv}	κ_{Avv}	κ_{SM}	$\cos(\alpha)$	σ_{VBF+VH} [pb]
`V_kSM1`	0	0	1	1	4.9392
`V_kHVV10_kSM0`	10	0	0	1	8.0489
`V_kHVV5_kSM1`	5	0	1	1	22.073
`V_kHVV2p5_kSM1`	2.5	0	1	1	7.3994
`V_kHVVm5_kSM1`	-5	0	1	1	20.501
`V_kHVVm2p5_kSM1`	-2.5	0	1	1	10.432
`V_kAVV15_kSM0`	0	15	0	$1/\sqrt{2}$	10.320
`V_kAVV5_kSM1`	0	5	1	$1/\sqrt{2}$	4.2259
`V_kAVV2p5_kSM1`	0	2.5	1	$1/\sqrt{2}$	1.9750
`V_kAVVm5_kSM1`	0	-5	1	$1/\sqrt{2}$	4.2366
`V_kAVVm2p5_kSM1`	0	-2.5	1	$1/\sqrt{2}$	1.9752

The scale factor for each bin j is therefor given as

$$\mathrm{SF}_j(\mathrm{ggF}) = \frac{N^{\mathrm{exp},j}_{\mathrm{Powheg,SM}}(\mathrm{ggF}) + N^{\mathrm{exp},j}_{\mathrm{Powheg,SM}}(\mathrm{t\bar{t}H}) + N^{\mathrm{exp},j}_{\mathrm{Powheg,SM}}(\mathrm{b\bar{b}H})}{N^{\mathrm{exp},j}_{\mathrm{MG5,SM}}(\mathrm{ggF})} \tag{6.9}$$

for the ggF production mode and

$$\mathrm{SF}_j(\mathrm{VBF+VH}) = \frac{N^{\mathrm{exp},j}_{\mathrm{Powheg,SM}}(\mathrm{VBF}) + N^{\mathrm{exp},j}_{\mathrm{Powheg,SM}}(\mathrm{WH}) + N^{\mathrm{exp},j}_{\mathrm{Powheg,SM}}(\mathrm{ZH})}{N^{\mathrm{exp},j}_{\mathrm{MG5,SM}}(\mathrm{VBF+VH_{had}}) + N^{\mathrm{exp},j}_{\mathrm{MG5,SM}}(\mathrm{VH_{lep}})} \tag{6.10}$$

for the VBF and VH production. The scale factors for each of the event categories introduced in Section 6.2.1 are summarised in Table 6.5.

Table 6.5: Higher-order correction scale factors for the different event categories in case of the ggF, VBF and VH production modes per production mode.

	Scale factor				
Sample	ggF enriched	mixed	VH-hadronic	VBF enriched	VH-leptonic
VBF+VH	1.16073	1.08693	1.01585	0.79225	1.31113
ggF+b$\bar{\mathrm{b}}$H+t$\bar{\mathrm{t}}$H	1.60186	1.44292	1.21405	1.25255	5.87204

6.3.3 Selection of Morphing Input Samples and Validation of the Signal Model

In this section, the selection of an optimal set of input samples for the signal model is described. The signal model constructed via morphing with these samples is validated against several simulated validation samples.
Given a particular Higgs production model, one signal model is constructed for each possible combination of input samples from Section 6.3.2. All signal models for this production mode should give the same predictions, but with possibly different statistical uncertainties. If available, an independent sample, which is not included in the set of morphing inputs is used for validation. The event yield obtained from the validation sample, N_{exp}^{val} is compared to the number N_{exp}^{model}, predicted by the given signal model at the validation point. The relative error is given as

$$\frac{\Delta N}{N_{\text{exp}}^{val}} = \frac{\left| N_{\text{exp}}^{val} - N_{\text{exp}}^{model} \right|}{N_{\text{exp}}^{val}}. \tag{6.11}$$

Input configurations with large error are discarded. As a next step, the statistical uncertainty of a given signal model is studied over a wide range of coupling parameters. This uncertainty is correlated with the size of weights w_i employed in the morphing function (Equation 6.3.1). The input samples with large weights introduce large statistical uncertainties for the predicted observables.

6.3.3.1 Signal Model Selection for the ggF Process

In order to build a complete set of inputs for the ggF process, there are six input samples needed (Table 6.2). Since there are nine samples generated in total, there are $\binom{9}{6} = 84$ possible sets of morphing input samples. Due to the large amount of possible combinations, a certain preselection is applied.

- In order to model the SM point ($\kappa_{SM} = 1, \kappa_{AZZ} = \kappa_{HZZ} = 0$) as precise as possible, the SM configuration, `G_kSM1`, is always included in the set of morphing inputs. This leads to $\binom{8}{5} = 56$ possible remaining combinations.
- The pure BSM signal configurations (`G_kHVV1_kSM0` and `G_kAVV1_kSM0`) should always be included. It has been shown that the relative error $\Delta N / N_{\text{exp}}^{val}$ is larger than 40% for at least one of the available validation points otherwise. Therefore $\binom{6}{3} = 20$ combinations remain.
- Eight further input combinations can be excluded, as the morphing matrix cannot be inverted for these. The rejected sets include in addition to the SM (`G_kSM1`) and the two pure BSM samples (`G_kHVV1_kSM0` and `G_kAVV1_kSM0`) combinations of (`G_kAVV6_kSM1` and `G_kAVVm6_kSM1`) or (`G_kHVV6_kSM1` and `G_kHVVm6_kSM1`).

The remaining 12 combinations, called morphing set S_1-S_{12}, are shown in Table 6.6. For each set a signal model is constructed and tested in the range $|\kappa_{AZZ} \cdot \sin\alpha| < 10$ and $|\kappa_{HZZ} \cdot \cos\alpha| < 10$, since this is the range not excluded by the Run I data (Section 3.6).

Table 6.6: Tested sets of morphing input samples used for the construction of ggF signal model. All sets include the simulated sample with SM configuration (`G_kSM1`), as well as the samples with pure BSM configurations, `G_kHVV1_kSM0` and `G_kAVV1_kSM0`.

Morphing set	Morphing input: `G_kSM1`, `G_kHVV1_kSM0`, `G_kAVV1_kSM0`,		
S_1	`G_kHVV6_kSM1`,	`G_kHVV6_kAVV6_kSM1`,	`G_kAVV6_kSM1`
S_2	`G_kHVV6_kSM1`,	`G_kHVVm6_kAVVm6_kSM1`,	`G_kAVV6_kSM1`
S_3	`G_kHVV6_kSM1`,	`G_kHVV6_kAVV6_kSM1`,	`G_kAVVm6_kSM1`
S_4	`G_kHVV6_kSM1`,	`G_kHVVm6_kAVVm6_kSM1`,	`G_kAVVm6_kSM1`
S_5	`G_kHVVm6_kSM1`,	`G_kHVV6_kAVV6_kSM1`,	`G_kAVV6_kSM1`
S_6	`G_kHVVm6_kSM1`,	`G_kHVVm6_kAVVm6_kSM1`,	`G_kAVV6_kSM1`
S_7	`G_kHVVm6_kSM1`,	`G_kHVV6_kAVV6_kSM1`,	`G_kAVVm6_kSM1`
S_8	`G_kHVVm6_kSM1`,	`G_kHVVm6_kAVVm6_kSM1`,	`G_kAVVm6_kSM1`
S_9	`G_kHVV6_kAVV6_kSM1`,	`G_kHVVm6_kAVVm6_kSM1`,	`G_kHVV6_kSM1`
S_{10}	`G_kHVV6_kAVV6_kSM1`,	`G_kHVVm6_kAVVm6_kSM1`,	`G_kHVVm6_kSM1`
S_{11}	`G_kHVV6_kAVV6_kSM1`,	`G_kHVVm6_kAVVm6_kSM1`,	`G_kAVV6_kSM1`
S_{12}	`G_kHVV6_kAVV6_kSM1`,	`G_kHVVm6_kAVVm6_kSM1`,	`G_kAVVm6_kSM1`

For each morphing set, there are three additional independent validation samples which are not included in the set itself. These samples are used for the validation of the corresponding signal model. In Table 6.7 and Table 6.8 a comparison of event yield at a validation point N_{exp}^{val} with the predicted event yield N_{exp}^{model} from a tested morphing set is given. The respective relative errors of the modelling prediction is also shown.

For a good signal modelling over a wide range of coupling parameters, the relative error $\Delta N / N_{\text{exp}}^{val}$ should be small and similar for all validation points. Therefore, morphing sets with relative errors larger than 5% at least one of the validation points are rejected. The remaining sets S_6, S_8, S_{10}, S_{11} and S_{12} provide predictions with relative errors better than 4%. For the morphing set S_{10}, the relative errors are of the same order for all three validation points. Other morphing sets have an acceptable error in two and one very small error in the third validation point.

As further optimisation criteria, the statistical uncertainty of the signal model predictions is studied over a wide coupling parameter range for the morphing sets S_6, S_8, S_{10}, S_{11} and S_{12}. The expected number of ggF events and the corresponding statistical uncertainty is shown in Figure 6.5.

Table 6.7: Number of expected ggF signal events in the mass window $m_{4\ell} \in [118, 129]$ GeV after the full selection from Section 5.4 at an integrated luminosity of $\mathcal{L} = 14.78$ fb^{-1}. Prediction from validation sample (N_{exp}^{val}) is compared to the prediction of a given signal model (S_1-S_6)

	Morphing set S_1		
Validation point	G_kHVVm6_kSM1	G_kAVVm6_kSM1	G_kHVVm6_kAVVm6_kSM1
N_{exp}^{val}	8.70 ± 0.12	3.40 ± 0.05	2.29 ± 0.03
N_{exp}^{model}	7.96 ± 0.38	3.39 ± 0.08	2.04 ± 0.22
$\Delta N / N_{\text{exp}}^{val}$ [%]	8.47	0.17	10.90

	Morphing set S_2		
Validation point	G_kHVVm6_kSM1	G_kAVVm6_kSM1	G_kHVV6_kAVV6_kSM1
N_{exp}^{val}	8.70 ± 0.12	3.40 ± 0.05	5.00 ± 0.07
N_{exp}^{model}	7.96 ± 0.38	3.39 ± 0.08	5.25 ± 0.21
$\Delta N / N_{\text{exp}}^{val}$ [%]	8.47	0.17	5.00

	Morphing set S_3		
Validation point	G_kHVVm6_kSM1	G_kAVV6_kSM1	G_kHVVm6_kAVVm6_kSM1
N_{exp}^{val}	8.70 ± 0.12	3.36 ± 0.05	2.29 ± 0.03
N_{exp}^{model}	7.96 ± 0.38	3.36 ± 0.08	2.05 ± 0.18
$\Delta N / N_{\text{exp}}^{val}$ [%]	8.47	0.17	10.40

	Morphing set S_4		
Validation point	G_kHVVm6_kSM1	G_kAVV6_kSM1	G_kHVV6_kAVV6_kSM1
N_{exp}^{val}	8.70 ± 0.12	3.36 ± 0.05	5.00 ± 0.07
N_{exp}^{model}	7.96 ± 0.38	3.36 ± 0.08	5.24 ± 1.67
$\Delta N / N_{\text{exp}}^{val}$ [%]	8.47	0.17	4.77

	Morphing set S_5		
Validation point	G_kHVV6_kSM1	G_kAVVm6_kSM1	G_kHVVm6_kAVVm6_kSM1
N_{exp}^{val}	19.88 ± 0.27	3.40 ± 0.05	2.29 ± 0.03
N_{exp}^{model}	19.14 ± 0.30	3.39 ± 0.08	2.41 ± 0.13
$\Delta N / N_{\text{exp}}^{val}$ [%]	3.71	0.17	5.17

	Morphing set S_6		
Validation point	G_kHVV6_kSM1	G_kAVVm6_kSM1	G_kHVV6_kAVV6_kSM1
N_{exp}^{val}	19.88 ± 0.27	3.40 ± 0.05	5.00 ± 0.07
N_{exp}^{model}	19.14 ± 0.30	3.39 ± 0.08	4.88 ± 0.12
$\Delta N / N_{\text{exp}}^{val}$ [%]	3.71	0.17	2.37

Table 6.8: Number of expected ggF signal events in the mass window $m_{4\ell} \in [118, 129]$ GeV after the full selection from Section 5.4 at an integrated luminosity of $\mathcal{L} = 14.78$ fb^{-1}. Prediction from validation sample (N_{exp}^{val}) is compared to the prediction of a given signal model (S_7-S_{12})

	Morphing set S_7		
Validation point	G_kHVV6_kSM1	G_kAVVm6_kSM1	G_kHVV6_kAVV6_kSM1
N_{exp}^{val}	19.88 ± 0.27	3.36 ± 0.05	2.29 ± 0.03
N_{exp}^{model}	19.14 ± 0.29	3.36 ± 0.08	2.42 ± 0.18
$\Delta N / N_{\text{exp}}^{val}$ [%]	3.71	0.17	5.67

	Morphing set S_8		
Validation point	G_kHVV6_kSM1	G_kAVV6_kSM1	G_kHVV6_kAVV6_kSM1
N_{exp}^{val}	19.88 ± 0.27	3.36 ± 0.05	5.00 ± 0.07
N_{exp}^{model}	19.14 ± 0.30	3.36 ± 0.08	4.87 ± 0.17
$\Delta N / N_{\text{exp}}^{val}$ [%]	3.71	0.17	2.6

	Morphing set S_9		
Validation point	G_kHVVm6_kSM1	G_kAVV6_kSM1	G_kAVVm6_kSM1
N_{exp}^{val}	8.70 ± 0.12	3.36 ± 0.05	3.40 ± 0.05
N_{exp}^{model}	7.96 ± 0.38	3.24 ± 0.10	3.51 ± 0.08
$\Delta N / N_{\text{exp}}^{val}$ [%]	8.47	3.72	3.52

	Morphing set S_{10}		
Validation point	G_kHVV6_kSM1	G_kAVV6_kSM1	G_kAVVm6_kSM1
N_{exp}^{val}	19.88 ± 0.27	3.36 ± 0.05	3.40 ± 0.05
N_{exp}^{model}	19.14 ± 0.29	3.42 ± 0.05	3.33 ± 0.08
$\Delta N / N_{\text{exp}}^{val}$ [%]	3.71	1.763	1.92

	Morphing set S_{11}		
Validation point	G_kHVV6_kSM1	G_kHVVm6_kSM1	G_kAVVm6_kSM1
N_{exp}^{val}	19.88 ± 0.27	8.70 ± 0.12	3.40 ± 0.05
N_{exp}^{model}	19.38 ± 0.36	8.46 ± 0.24	3.39 ± 0.08
$\Delta N / N_{\text{exp}}^{val}$ [%]	2.51	2.73	0.17

	Morphing set S_{12}		
Validation point	G_kHVV6_kSM1	G_kHVVm6_kSM1	G_kAVV6_kSM1
N_{exp}^{val}	19.88 ± 0.27	8.70 ± 0.12	3.36 ± 0.05
N_{exp}^{model}	19.40 ± 0.238805	8.44 ± 0.35	3.36 ± 0.08
$\Delta N / N_{\text{exp}}^{val}$ [%]	2.40	2.99	0.17

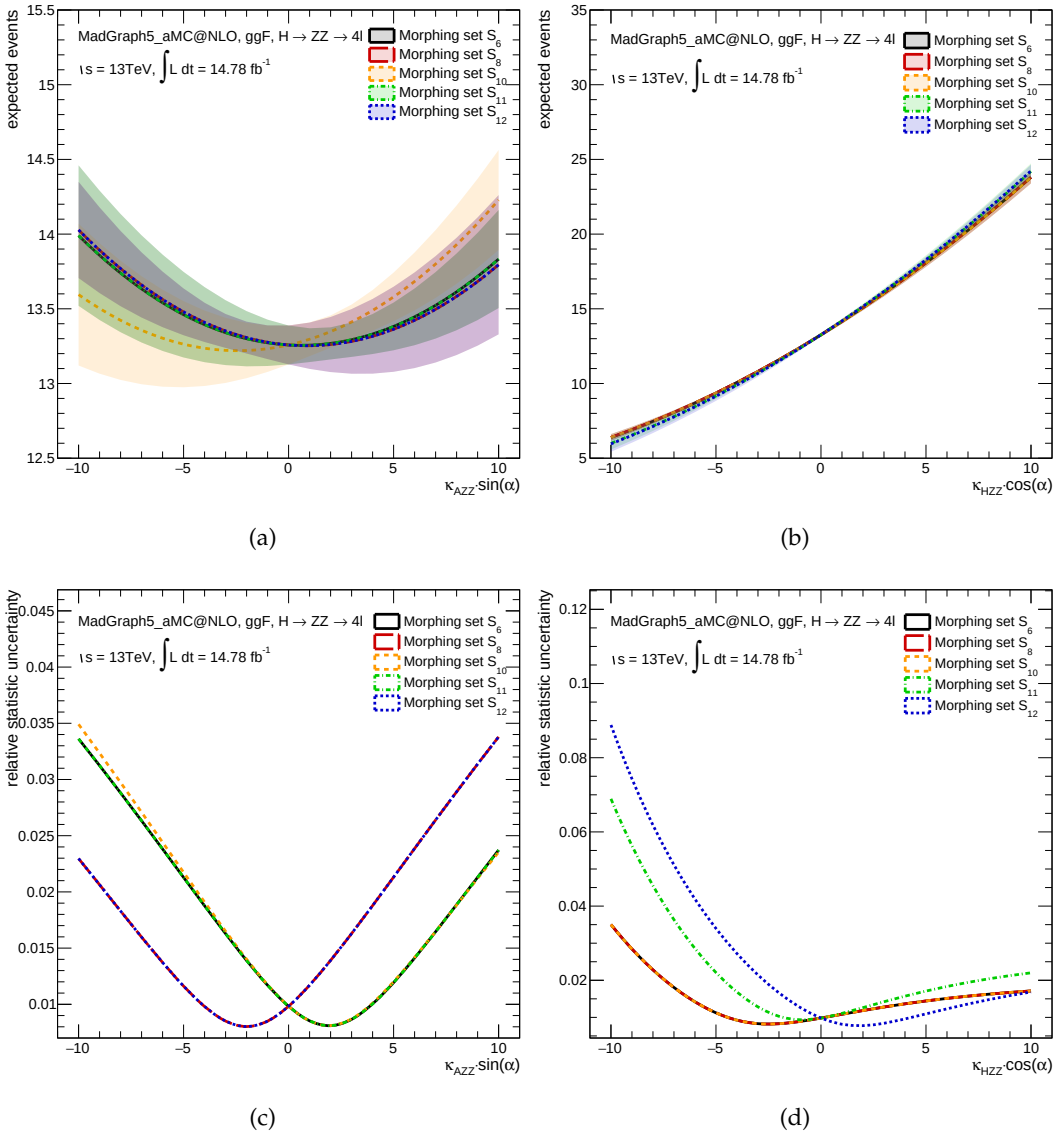

Figure 6.5: (a) and (b): Number of expected ggF events predicted by a given morphing set (S_6, S_8, S_{10}, S_{11} and S_{12}) as a function of the CP-odd and CP-even coupling parameter $\kappa_{AZZ} \cdot \sin\alpha$ and $\kappa_{HZZ} \cdot \cos\alpha$, respectively. (c) and (d): Relative statistical uncertainty as a function of the CP-odd and CP-even coupling parameter $\kappa_{AZZ} \cdot \sin\alpha$ and $\kappa_{HZZ} \cdot \cos\alpha$, respectively.

The relative statistical uncertainty for all tested sets of morphing inputs is symmetrically distributed around the minimum value of $\sim 0.8\%$ at the CP-odd coupling parameter $|\kappa_{AZZ} \cdot \sin\alpha| = 2$. Morphing sets S_6, S_{10} and S_{11} reach statistical uncertainties of 3.5% at the negative end of the modelled parameter range, $\kappa_{AZZ} \cdot \sin\alpha = -10$, while for the sets S_8 and S_{12} the same value at the positive end, $\kappa_{AZZ} \cdot \sin\alpha = 10$, is reached. All tested sets of morphing input samples have a similar performance. The smallest relative statistical uncertainty over a wide range of CP-even coupling parameter values are obtained for morphing sets S_6, S_8 and S_{10} and reaches the minimum value of $\sim 1\%$ at $\kappa_{HZZ} \cdot \cos\alpha = -3$.
The last optimisation criterion is the size of the weight w_i by which the input samples are weighted. The weight size depends on the coupling parameter value. For each tested set of morphing inputs the minimum and maximum weight value are evaluated by scanning the coupling values $\kappa_{AZZ} \cdot \sin(\alpha)$ and $\kappa_{HZZ} \cdot \cos(\alpha)$ and are summarised in Table 6.9.

Table 6.9: Range of weight values obtained with a given tested ggF morphing input set (S_6, S_8, S_{10}, S_{11} and S_{12}) from a scan in the $\kappa_{AZZ} \cdot \sin(\alpha)$ and $\kappa_{HZZ} \cdot \cos(\alpha)$ parameter space.

Morphing set	Weight for values $[w_i^{min}, w_i^{max}]$ for	
	$\kappa_{AZZ} \cdot \sin(\alpha) \in [-10, 10]$	$\kappa_{HZZ} \cdot \cos(\alpha) \in [-10, 10]$
S_6	$[-40, 640]$	$[-10, 160]$
S_8	$[-40, 640]$	$[-10, 160]$
S_{10}	$[-50, 400]$	$[-10, 160]$
S_{11}	$[-40, 640]$	$[-240, 240]$
S_{12}	$[-40, 640]$	$[-240, 240]$

The smallest range of weights indicates the morphing set with the best statistical performance. The smallest range of weights for $\kappa_{AZZ} \cdot \sin(\alpha) \in [-10, 10]$ is $[-50, 400]$ and for $\kappa_{HZZ} \cdot \cos(\alpha) \in [-10, 10]$ it is $[-10, 160]$ both obtained with the morphing set S_{10}. Thus, the set S_{10} provides the signal model with the lowest statistical uncertainty.
Since the morphing set S_{10} also providing predictions with relatively small deviations of about 2.5% from the true value given by validation samples this set has been chosen for the final construction of the ggF signal model.
In addition to the validation of event yield predictions, for the selected morphing set S_{10}, the modelling of CP-sensitive kinematic distributions (see Section 6.2) has been validated. Kinematic distributions obtained from two different validation samples `G_kHVV6_kSM1` and `G_kAVVm6_kSM1` are compared to the prediction by the signal

model built with the morphing set S_{10}. Following observables are tested: invariant mass of the leading lepton pair m_{12}, the invariant mass of the subleading lepton pair m_{34}, the angle between the leading Z boson and negative final state lepton $\cos(\theta_1)$, the angle between the subleading Z boson and negative final state lepton $\cos(\theta_2)$, the angle between decay plane of Z bosons ϕ and the four-lepton transverse momentum $p_{\mathrm{T},4\ell}$. This comparison is shown in Figure 6.6. All distributions are normalised to their respective cross sections. The distributions obtained by the signal model agree well with those from validation sample, therefore confirming the choice of the signal model.

6.3.3.2 Signal Model Selection for the VBF and VH Process

Similarly as the ggF production the signal model can be constructed and validated for the vector boson fusion and associated Higgs boson production with vector bosons. Since there are only six input samples generated for each of the two coupling parameters κ_{AZZ} and κ_{HZZ}, while five of these are needed to build a morphing set, there are in general six possible combinations to consider. By requiring that each set should contain the SM point (`V_kSM1`), five possible morphing sets remain. The signal model is optimised in the ranges $|\kappa_{AZZ} \cdot \sin\alpha| < 10$ and $|\kappa_{HZZ} \cdot \cos\alpha| < 10$. The signal model for the AZZ coupling is optimised separately from the model for the HZZ coupling.
The morphing sets S_1-S_5, tested for the modelling in dependence on the CP-odd coupling parameter κ_{AZZ} are shown in Table 6.10.

Table 6.10: Tested sets of morphing input samples used for the construction of the VBF and VH signal model for the AZZ coupling. All sets include the simulated sample with SM configuration (`V_kSM1`).

Morphing set	Morphing set: `V_kSM1`,
S_1	`V_kAVV5_kSM1, V_kAVV2p5_kSM1,V_kAVVm5_kSM1, V_kAVVm2p5_kSM1`
S_2	`V_kAVV15_kSM0,V_kAVV2p5_kSM1,V_kAVVm5_kSM1, V_kAVVm2p5_kSM1`
S_3	`V_kAVV15_kSM0,V_kAVV5_kSM1, V_kAVVm5_kSM1, V_kAVVm2p5_kSM1`
S_4	`V_kAVV15_kSM0,V_kAVV5_kSM1, V_kAVV2p5_kSM1,V_kAVVm2p5_kSM1`
S_5	`V_kAVV15_kSM0,V_kAVV5_kSM1, V_kAVV2p5_kSM1,V_kAVVm5_kSM1`

Only one validation sample is available for each of these morphing sets. The number of expected events at the validation point N_{exp}^{val}, the corresponding number obtained from the signal model N_{exp}^{model}, as well as the respective relative error $\Delta N / N_{\mathrm{exp}}^{val}$ are shown in Table 6.11.

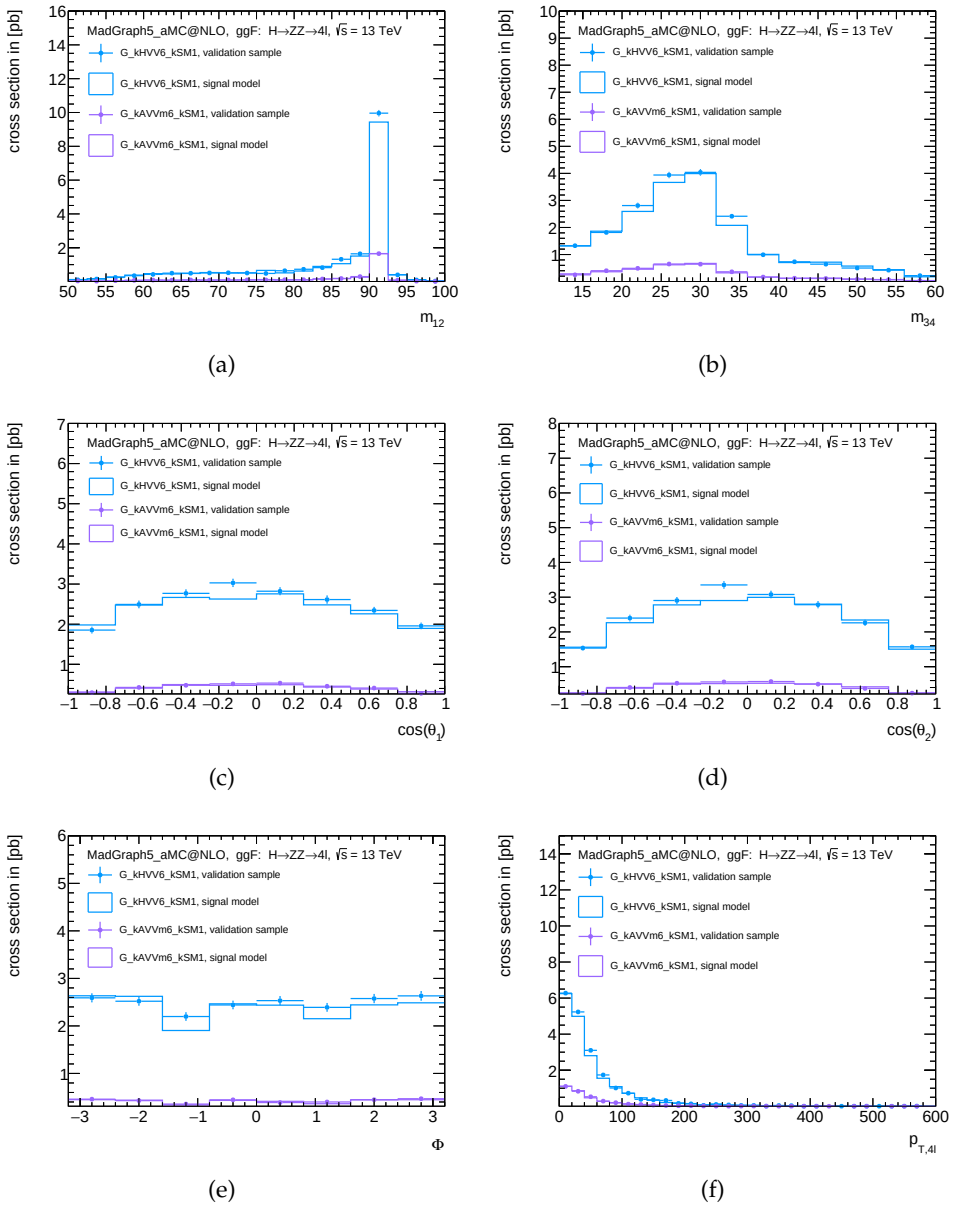

Figure 6.6: Comparison of the ggF signal model predictions with the morphing set S_{10} to the distributions from validation samples. Distributions of following observables sensitive to BSM coupling contributions are shown: (a) invariant mass of the leading lepton pair m_{12} (b) invariant mass of the subleading lepton pair m_{34} (c) angle between the leading Z boson and negative final state lepton $\cos(\theta_1)$ (d) angle between the subleading Z boson and negative final state lepton $\cos(\theta_2)$ (e) angle between decay plane of Z bosons ϕ and (f) four-lepton transverse momentum $p_{\mathrm{T},4\ell}$.

Table 6.11: Number of expected VBF and VH signal events for the AZZ coupling in the mass window $m_{4\ell} \in [118, 129]$ GeV after the full selection from Section 5.4 at an integrated luminosity of $\mathcal{L} = 14.78$ fb^{-1}. Prediction from validation sample (N_{exp}^{val}) is compared to the prediction of a given signal model (S_1-S_5).

Validation point	Morphing set S_1 `V_kAVV15_kSM0`	Morphing set S_2 `V_kAVV5_kSM1`	Morphing set S_3 `V_kAVV2p5_kSM1`
N_{exp}^{val}	5.91 ± 0.05	2.26 ± 0.02	1.07 ± 0.01
N_{exp}^{model}	14.01 ± 13.47	2.22 ± 0.06	1.08 ± 0.12
$\Delta N / N_{\text{exp}}^{val}$ [%]	137.0	1.66	0.88

Validation point	Morphing set S_4 `V_kAVVm5_kSM1`	Morphing set S_5 `V_kAVVm2p5_kSM1`
N_{exp}^{val}	2.34 ± 0.02	$1.06 \pm 0,01$
N_{exp}^{model}	2.31 ± 0.06	1.07 ± 0.01
$\Delta N / N_{\text{exp}}^{val}$ [%]	1.60	0.87

Based on the large relative error of 137%, morphing set S_1 is excluded. For all other input combinations, only small relative errors of about 1% are obtained.
Expected number of events and the relative statistical uncertainty for all morphing sets is shown as a function of the CP-odd coupling parameter $\kappa_{AZZ} \cdot \sin\alpha$ in Figure 6.7.

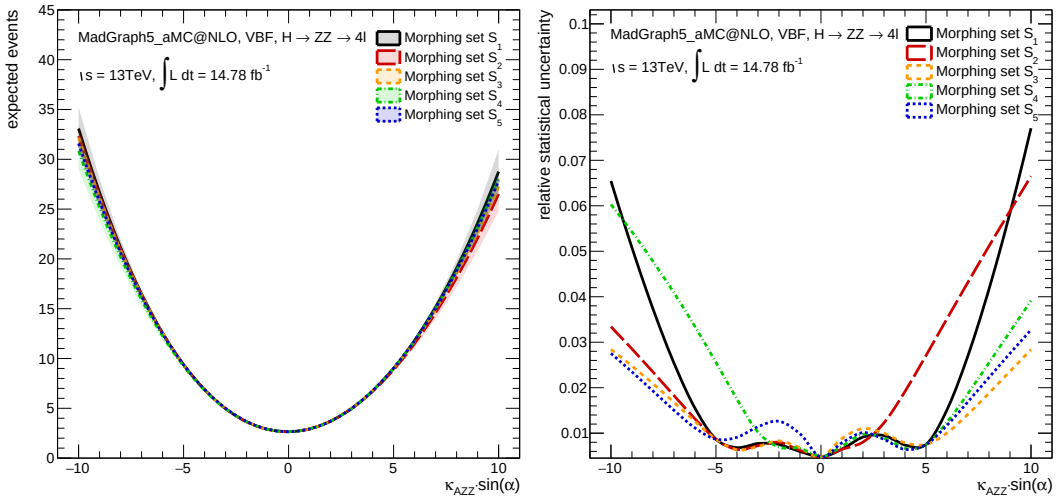

(a) (b)

Figure 6.7: (a) Number of expected VBF and VH events predicted by a given morphing set (S_1-S_5) and (b) relative statistical uncertainty as a function of the CP-odd coupling parameter $\kappa_{AZZ} \cdot \sin\alpha$.

All sets give very similar predictions of the event yields. The smallest statistical uncertainty over the whole parameter range is achieved for morphing sets S_3 and S_5. While the set S_3 has a smaller relative uncertainty for positive coupling values, the set S_5 gives smaller uncertainties for negative coupling parameter values.
The minimum and maximum value of morphing weights in the parameter range $\kappa_{AZZ} \cdot \sin(\alpha) \in [-10, 10]$ is given for each morphing set in Table 6.12.

Table 6.12: Range of weight values obtained with a given tested VBF and VH morphing input set (S_1-S_5) from a scan in the $\kappa_{AZZ} \cdot \sin(\alpha)$ parameter space.

Morphing set	Weight for values $[w_i^{min}, w_i^{max}]$ for $\kappa_{AZZ} \cdot \sin(\alpha) \in [-10, 10]$
S_1	$[-160, 60]$
S_2	$[-80, 140]$
S_3	$[-60, 60]$
S_4	$[-80, 140]$
S_5	$[-60, 60]$

The smallest range $[-60, 60]$ is obtained for morphing sets S_3 and S_5.
Due to the smallest relative errors with respect to the expected event yields at the validation point the morphing input set S_5 is chosen to model the dependence of the VBF and VH production on the CP-odd BSM coupling parameter.
Distributions of CP-sensitive observables m_{12}, m_{34}, $\cos(\theta_1)$, $\cos(\theta_2)$, ϕ and $p_{\mathrm{T},4\ell}$, from the validation sample are compared to those from the signal model, as shown in Figure 6.8. Good agreement is observed, confirming the choice of morphing set.

The morphing sets S_1-S_5 used for the modelling of VBF and VH in dependence of the higher-order CP-even coupling parameter κ_{HZZ} are shown in Table 6.13. The expected number of events N_{exp}^{val}, N_{exp}^{model} and the relative difference $\Delta N / N_{\mathrm{exp}}^{val}$ are given in Table 6.14.
As in the case of the CP-odd coupling parameter, the morphing set which does not include the simulated sample with pure BSM configuration, set S_1, gives the largest deviations from the validation point of about 8%. All other morphing sets result in relative errors $\Delta N / N_{\mathrm{exp}}^{val}$ of smaller than 0.4%. The smallest deviation of 0.17% is obtained with the morphing set S_5.
The expected number of events and the relative statistical uncertainty are shown as a function of the CP-even coupling parameter $\kappa_{HZZ} \cdot \cos\alpha$ for each morphing set in Figure 6.9.

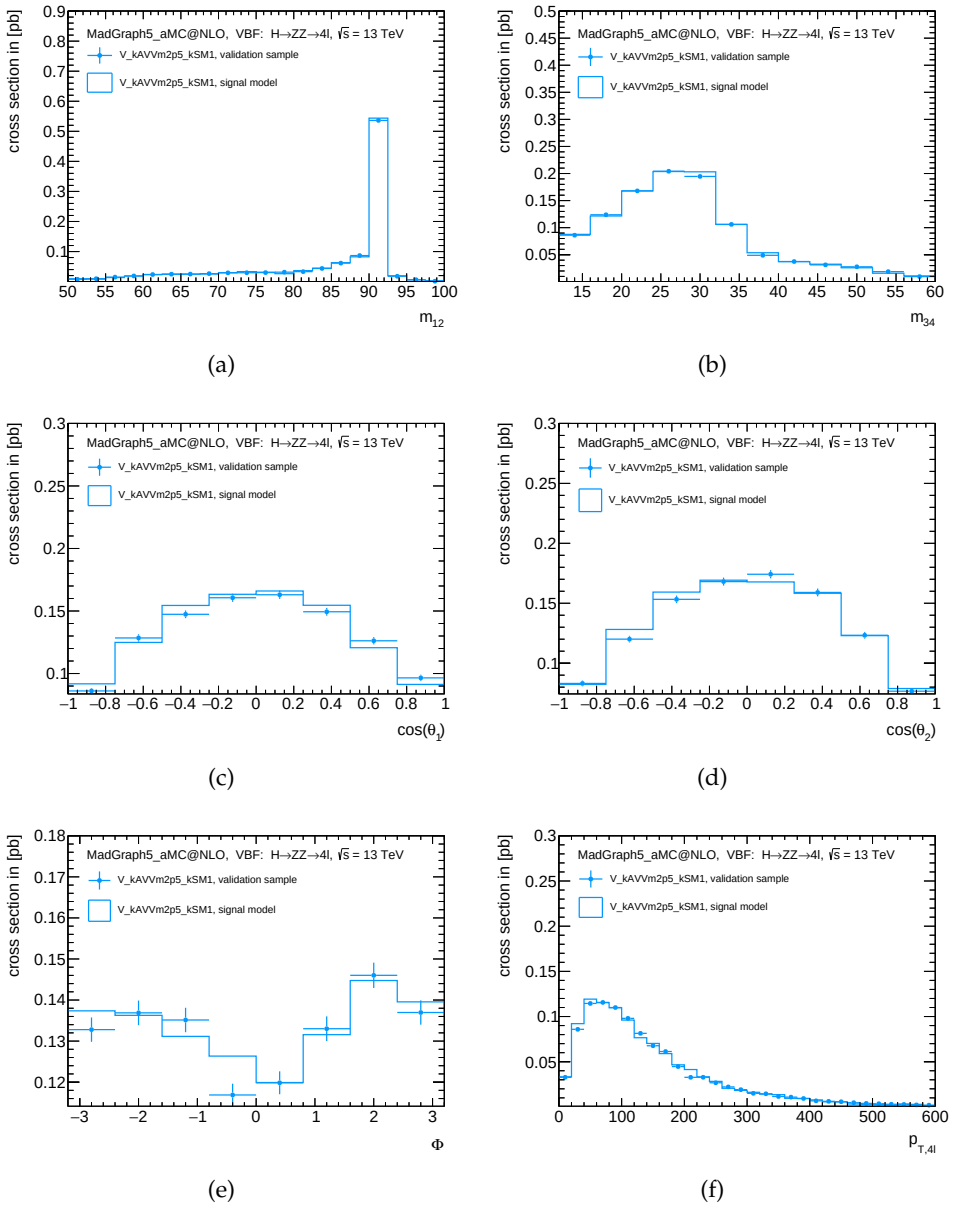

Figure 6.8: Comparison of the VBF and VH signal model predictions for AZZ coupling with the morphing set S_5 to the distributions from validation samples. Distributions of following observables sensitive to BSM coupling contributions are shown: (a) invariant mass of the leading lepton pair m_{12} (b) invariant mass of the subleading lepton pair m_{34} (c) angle between the leading Z boson and negative final state lepton $\cos(\theta_1)$ (d) angle between the subleading Z boson and negative final state lepton $\cos(\theta_2)$ (e) angle between decay plane of Z bosons ϕ and (f) four-lepton transverse momentum $p_{\mathrm{T},4\ell}$.

Table 6.13: Tested sets of morphing input samples used for the construction of the VBF and VH signal model for the HZZ coupling. All sets include the simulated sample with SM configuration (`V_kSM1`).

Morphing set	Morphing input: `V_kSM1`,
S_1	`V_kHVV5_kSM1, V_kHVV2p5_kSM1,V_kHVVm5_kSM1, V_kHVVm2p5_kSM1`
S_2	`V_kHVV10_kSM0,V_kHVV2p5_kSM1,V_kHVVm5_kSM1, V_kHVVm2p5_kSM1`
S_3	`V_kHVV10_kSM0,V_kHVV5_kSM1, V_kHVVm5_kSM1, V_kHVVm2p5_kSM1`
S_4	`V_kHVV10_kSM0,V_kHVV5_kSM1, V_kHVV2p5_kSM1,V_kHVVm2p5_kSM1`
S_5	`V_kHVV10_kSM0,V_kHVV5_kSM1, V_kHVV2p5_kSM1,V_kHVVm5_kSM1`

Table 6.14: Number of expected VBF and VH signal events for the HZZ coupling in the mass window $m_{4\ell} \in [118, 129]$ GeV after the full selection from Section 5.4 at an integrated luminosity of $\mathcal{L} = 14.78$ fb^{-1}. Prediction from validation sample (N_{exp}^{val}) is compared to the prediction of a given signal model (S_1-S_5).

Validation point	Morphing set S_1 `V_kHVV10_kSM0`	Morphing set S_2 `V_kHVV5_kSM1`	Morphing set S_3 `V_kHVV2p5_kSM1`
N_{exp}^{val}	4.80 ± 0.03	12.45 ± 0.10	4.26 ± 0.03
N_{exp}^{model}	5.18 ± 2.70	12.41 ± 0.23	0.29 ± 0.01
$\Delta N / N_{\text{exp}}^{val}$ [%]	7.98	0.29	0.21

Validation point	Morphing set S_4 `V_kHVVm5_kSM1`	Morphing set S_5 `V_kHVVm2p5_kSM1`	
N_{exp}^{val}	9.80 ± 0.07	5.15 ± 0.04	
N_{exp}^{model}	9.76 ± 0.24	5.16 ± 0.049	
$\Delta N / N_{\text{exp}}^{val}$ [%]	0.37	0.17	

The smallest uncertainties in the wide range of coupling values is obtained with the morphing set S_5.
The minimum and maximum weight values for the tested morphing sets in the range $\kappa_{HZZ} \cdot \cos(\alpha) \in [-10, 10]$ are shown in Table 6.15.
The smallest range of weights $[-15, 15]$ is obtained from morphing set S_3 and S_5.
In total, the best performance is obtained by morphing set S_5.
Distributions of CP-sensitive observables m_{12}, m_{34}, $\cos(\theta_1)$, $\cos(\theta_2)$, ϕ and $p_{\text{T},4\ell}$, from the validation sample and from the signal model with morphing set S_5 are shown in Figure 6.10. A good agreement of the two is observed.

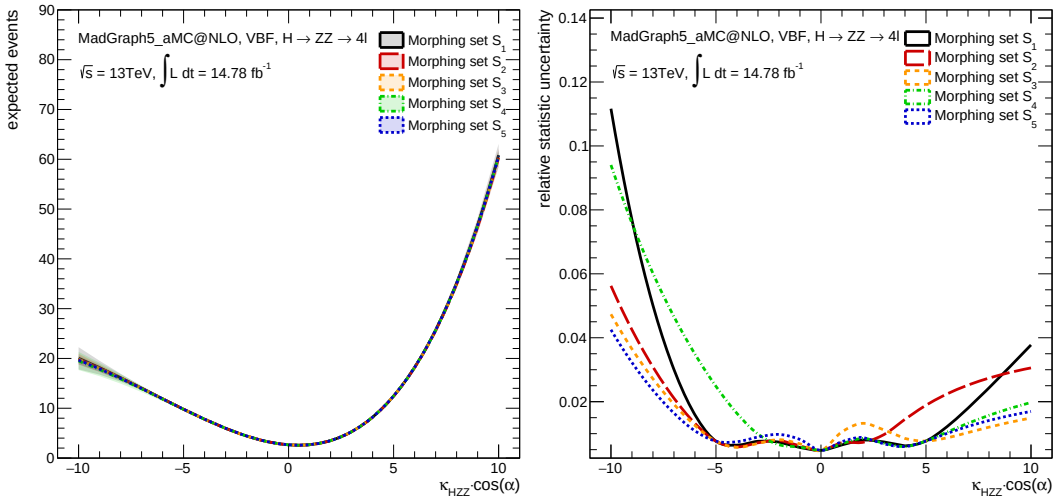

(a) (b)

Figure 6.9: (a) Number of expected VBF and VH events predicted by a given morphing set (S_1-S_5) and (b) relative statistical uncertainty as a function of the CP-even coupling parameter $\kappa_{HZZ} \cdot \cos\alpha$.

Table 6.15: Range of weight values obtained with a given tested VBF and VH morphing input set (S_1-S_5) from a scan in the $\kappa_{HZZ} \cdot \cos(\alpha)$ parameter space.

Morphing set	Weight for values $[w_i^{min}, w_i^{max}]$ for $\kappa_{HZZ} \cdot \cos(\alpha) \in [-10, 10]$
S_1	$[-40, 44]$
S_2	$[-44, 32]$
S_3	$[-15, 15]$
S_4	$[-44, 32]$
S_5	$[-15, 15]$

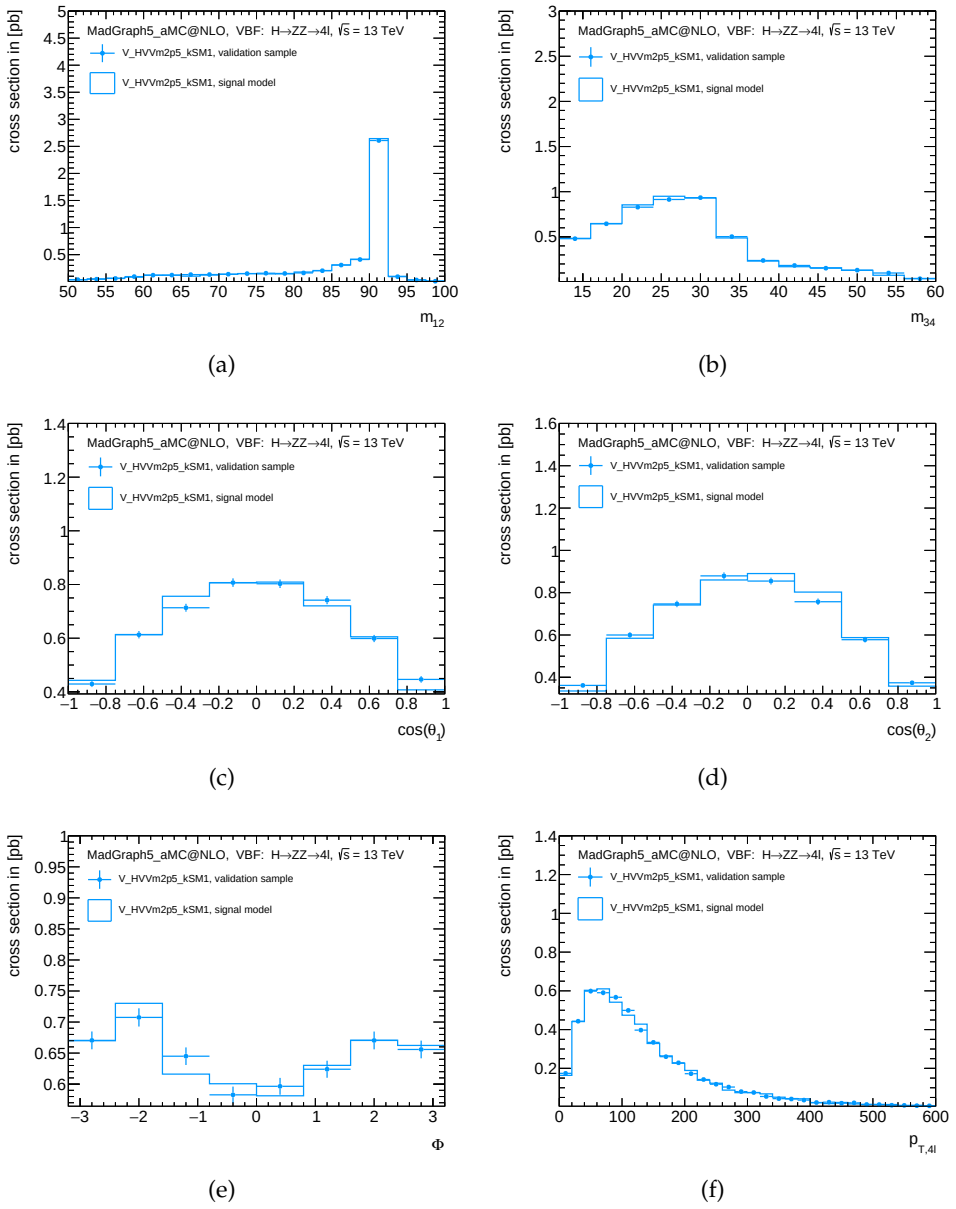

Figure 6.10: Comparison of the VBF and VH signal model predictions for HZZ coupling with the morphing set S_5 to the distributions from validation samples. Distributions of following observables sensitive to BSM coupling contributions are shown: (a) invariant mass of the leading lepton pair m_{12} (b) invariant mass of the subleading lepton pair m_{34} (c) angle between the leading Z boson and negative final state lepton $\cos(\theta_1)$ (d) angle between the subleading Z boson and negative final state lepton $\cos(\theta_2)$ (e) angle between decay plane of Z bosons ϕ and (f) four-lepton transverse momentum $p_{\mathrm{T},4\ell}$.

6.4 Results

The coupling parameters κ_{AZZ} and κ_{HZZ} are measured by comparing the signal model predictions to the number of events observed in each event category in data. The contribution of background processes, ZZ^*, Z+jets and $t\bar{t}$ are taken into account, as described in Section 5.2. The expected and observed number of events in the mass range 118 GeV $< m_{4\ell} <$ 129 GeV after the full $H \to ZZ^* \to 4\ell$ event selection is shown separately in each event category in Table 6.16. A SM Higgs boson is assumed.

Table 6.16: Expected and observed number of $H \to ZZ^* \to 4\ell$ events in the mass range 118 GeV $< m_{4\ell} <$ 129 GeV in each event category. The results are based on 14.78 fb^{-1} of data at a centre-of-mass energy of 13 TeV. The SM Higgs boson signal is assumed. Errors represent the statistical uncertainties only.

Event	Signal			
category	ggF+t$\bar{\text{t}}$H+ b$\bar{\text{b}}$H	VBF	WH	ZH
ggF enriched	11.16 ± 0.04	0.120 ± 0.002	0.047 ± 0.001	0.060 ± 0.001
mixed	5.67 ± 0.02	0.587 ± 0.003	0.137 ± 0.002	0.091 ± 0.001
VH-hadronic	1.05 ± 0.02	0.084 ± 0.001	0.143 ± 0.002	0.102 ± 0.001
VBF enriched	1.86 ± 0.02	0.919 ± 0.003	0.074 ± 0.002	0.052 ± 0.001
VH-leptonic	0.055 ± 0.002	0.002 ± 0.001	0.067 ± 0.001	0.011 ± 0.001
Total	19.8 ± 0.1	1.714 ± 0.005	0.469 ± 0.003	0.316 ± 0.006

Event	Background		Total	Observed
category	ZZ^*	Z+jets,$\bar{t}t$	expected	
ggF enriched	6.10 ± 0.02	0.84 ± 0.12	18.4 ± 0.4	21
mixed	1.63 ± 0.01	0.44 ± 0.07	8.6 ± 0.1	12
VH-hadronic	0.17 ± 0.01	0.088 ± 0.011	1.6 ± 0.1	2
VBF enriched	0.22 ± 0.01	0.24 ± 0.11	3.4 ± 0.1	9
VH-leptonic	0.02 ± 0.01	0.012 ± 0.010	0.17 ± 0.02	0
Total	8.14 ± 0.04	1.62 ± 0.07	32.2 ± 0.5	44

In all categories, except in the *"VH-hadronic"* event category, an excess of events is observed above the expectation. The largest excess with about three times more observed than expected events is seen in the *"VBF enriched'* category.

The event rates are sensitive to BSM coupling parameters. Separation into event categories increases this sensitivity as the contributions from different production modes can be distinguished.
In order to probe the BSM contribution to the HZZ tensor structure, the fit of the expected rates to the observed ones in each category is performed with the BSM couplings as free parameters of the fit. In this analysis the coupling parameter $g_{SM} = \kappa_{SM} \cdot \cos(\alpha)$ is set to unity in order to reduce the number of free fit parameters fitted to the relatively small amount of data.
The likelihood function $\mathcal{L}(\vec{\kappa}, \vec{\theta})$ that depends on the coupling parameters $\vec{\kappa}$ is constructed as a product of conditional probabilities in each event category j

$$\mathcal{L}(\text{data} \mid \vec{\kappa}, \vec{\theta}) = \prod_{j}^{N_{\text{channel}}} P\big(N_j \mid S_j^{(\vec{\kappa})}(\vec{\theta}) + B_j(\vec{\theta})\big) \times \mathcal{A}_j(\vec{\theta}) \,, \tag{6.12}$$

where $\vec{\theta}$ are all nuisance parameters accounting for signal and background systematic uncertainties. The likelihood function is a product of Poisson probabilities P to observe N_j events in the event category j, given the expectations for the signal, $S_j^{(\vec{\kappa})}(\vec{\theta})$, and for the background, $B_j(\vec{\theta})$. The functions $\mathcal{A}_j(\vec{\theta})$ take constraints coming from auxiliary measurements of systematic uncertainties into account. The signal rates are obtained from the signal model described in Section 6.3.
The exclusion limits on the BSM contributions are set using profile likelihood ratio method with a test statistic q [89], defined as the ratio of two profile likelihoods,

$$q^{\kappa} = -2 \ln \frac{\mathcal{L}(\kappa, \hat{\hat{\theta}})}{\mathcal{L}(\hat{\kappa}.\hat{\theta})} \,. \tag{6.13}$$

$\mathcal{L}(\hat{\kappa}, \hat{\theta})$ is the maximum likelihood estimator of an unconditional fit in which both κ and θ parameters are free parameters of the fit. $\mathcal{L}(\kappa, \hat{\hat{\theta}})$ is the likelihood estimator with profiled couplings κ, i.e. with coupling κ set to a fixed value.

Only one of the two BSM coupling parameters is fitted at the same time due to the low number of observed events. No systematic uncertainties are taken into account. The total number of observed and expected events, as well as the observed and expected scans of the test statistic q are shown in Figure 6.11 as a function of κ_{AZZ} and κ_{HZZ} coupling parameters. The expected curves are based on the assumption of the SM Higgs boson signal.

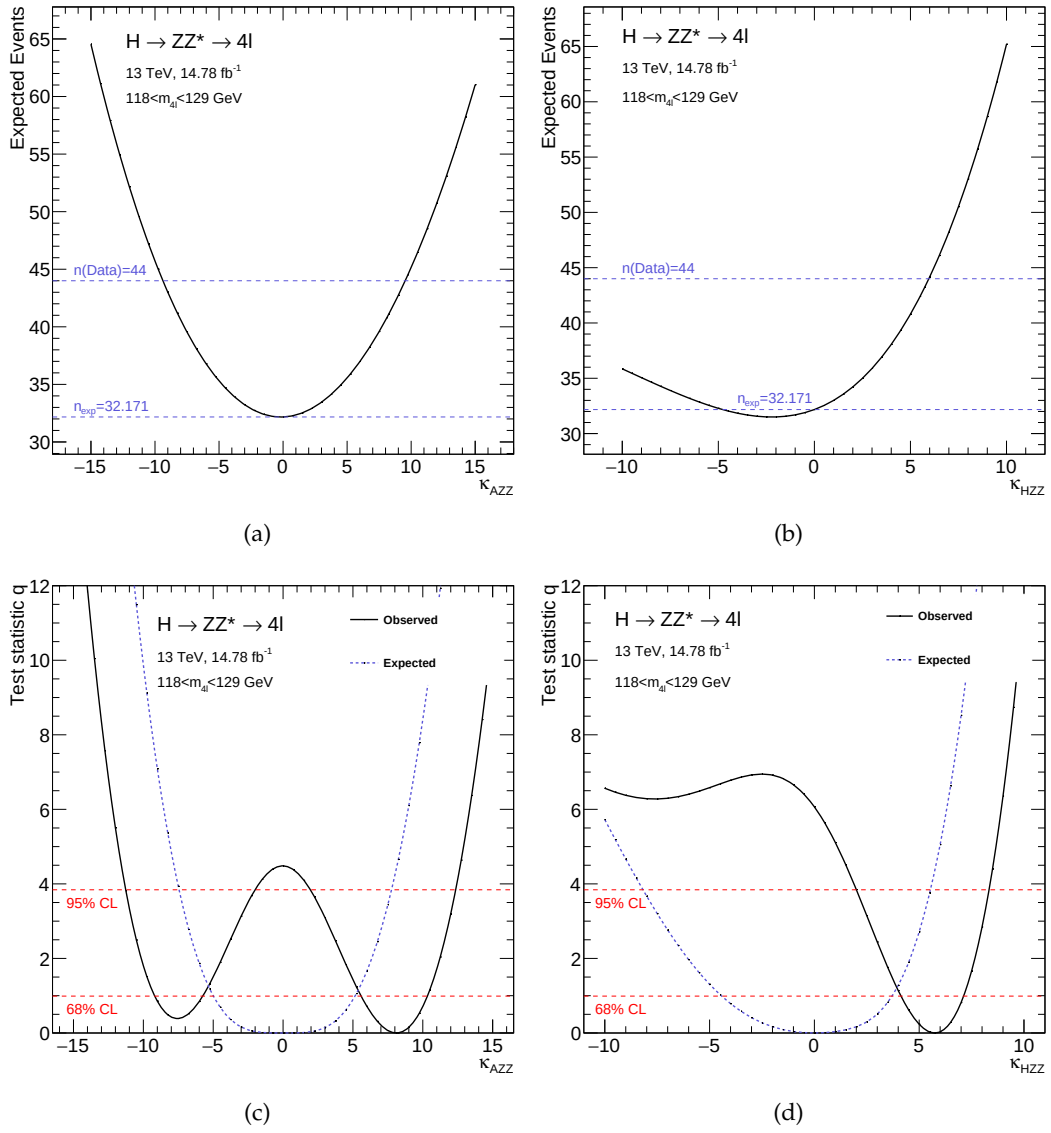

Figure 6.11: (a) and (b): Total number of expected events in all event categories as a function of the CP-odd and CP-even coupling parameter, κ_{AZZ} and κ_{HZZ}, respectively. The observed numbers and the expectation from SM signal are indicated with horizontal lines. (c) and (d): Expected and observed test statistic q as a function of κ_{AZZ} and κ_{HZZ}, respectively. Dashed horizontal lines indicate the thresholds corresponding to 68% and 95% confidence level (CL) intervals.

The coupling parameters with higher values of the test statistic q are excluded at a given confidence level. The observed and expected limits at 95% confidence Level (CL) for κ_{AZZ} and κ_{HZZ} obtained with asymptotic approximation [89] are shown in Table 6.17.

Table 6.17: Expected and observed 95% confidence level (CL) interval for the κ_{AZZ} and κ_{HZZ} coupling parameters.

BSM coupling parameter	95% confidence level (CL)	
	expected	observed
κ_{AZZ}	$[-7.4, 7.7]$	$[-11.3, -2.0] \cup [1.9, 12.3]$
κ_{HZZ}	$[-8.2, 5.5]$	$[2.0, 8.3]$

Due to a larger number of observed than expected events, the best fit values of the coupling parameters are not located at the SM expectation. The best fit values are $\kappa_{AZZ} = 8.1$ and $\kappa_{HZZ} = 5.7$. The values are compatible with the SM predictions within 2.2 and 2.5 standard deviations, respectively. The κ_{AZZ} values in the range of $(-\infty, -11.3) \cup (-2.0, 1.9) \cup (2.3, \infty)$ and κ_{HZZ} values in the range $(-\infty, 2.0) \cup (8.3, \infty)$ are excluded with 95% confidence level.
These limits do not change significantly after taking into account the systematic uncertainties [87]. The obtained exclusion limits are by a factor of 4 to 10 better than the ones obtained from Run I.

Chapter 7

Summary

The new particle discovered in 2012 by the ATLAS and CMS experiments is compatible with the Standard Model Higgs boson predicted by the Brout-Englert-Higgs mechanism. Measurements of the spin (J) and charge conjugation and parity (CP) properties of the discovered particle are compatible with the Standard Model prediction of a pure CP-state, $J^{CP} = 0^{++}$. However, small admixtures of anomalous CP-even or CP-odd contributions are still not excluded. Therefor, a precise measurement of the tensor structure of Higgs boson couplings to Standard Model particles is needed. The production cross sections of different Higgs boson production modes as well as the kinematic properties of the resulting final state products are sensitive to the exact tensor structure. In this thesis the structure of the Higgs boson coupling to Z bosons (HZZ coupling) is studied in the Higgs boson decay channel, $H \to ZZ^* \to 4\ell$, with $\ell = e, \mu$.

The study is performed on a Run II set of LHC proton-proton collision data recorded by the ATLAS detector at a centre-of-mass energy of $\sqrt{s} = 13$ TeV and the total integrated luminosity of 14.78 fb^{-1}.
The four-lepton Higgs boson candidates are discriminated from other background processes by rejecting leptons with large impact parameter and non-isolated leptons surrounded by large hadronic activity. Two of the four leptons are assigned to the on-shell (Z) and the remaining two to the off-shell (Z^*) boson. The event selection criteria define the so-called signal region. The observed number of Higgs boson candidates after the full event selection is compared to the expected signal and background contribution.
While signal and irreducible ZZ^* background contributions are estimated from MC simulation, Z+jets and $t\bar{t}$ background contributions are measured in signal-depleted control data. The so-called $Z + \mu\mu$ control regions with an enhanced contribution of Z+jets events are defined by inverting the impact parameter and isolation criteria of the two muons from the off-shell Z boson candidate. The background yields measured in these regions are extrapolated to the signal region. The extrapolation factors, related to the impact parameter and isolation cut efficiency, are obtained from the simulated Z+jets events originating from heavy flavour quarks. It is

assumed that these factors are also applicable on Z+jets events with jets from light flavour quarks, since the simulation of these events is limited by a large statistical uncertainty in the signal region.
In order to validate the simulated extrapolation factors with data and verify the above assumption, two additional so-called $Z + \mu$ validation regions are introduced. Both consist of events with one Z boson candidate and exactly one additional muon with relaxed impact parameter and isolation criteria. The first region is enriched with muons from heavy flavour hadron decays (heavy-flavour-enriched sample) and the other one with muons from in-flight decays of pions and kaons (light-flavour-enriched sample). In the heavy-flavour-enriched sample a good agreement is observed between the measured and simulated impact parameter and isolation cut efficiencies. This validates the extrapolation factor for the heavy flavour component. In the light-flavour-enriched sample, an about 10% lower isolation efficiency is measured compared to the one in the heavy-flavour-enriched sample. This difference is propagated as the statistical uncertainty of the extrapolation factors.
After the full event selection and the described background estimation there are 44 Higgs boson candidates observed, while 32.0 ± 3.2 are expected from signal and background processes. The observed data agree within two standard derivations with the Standard Model prediction.

All selected Higgs boson candidates are employed for the measurement of the tensor structure of the HZZ coupling. For this purpose, a dedicated signal model was introduced, validated and optimised in order to predict the number of Higgs boson signal events in the dependence on the anomalous (non-Standard Model) CP-even (κ_{HZZ}) and CP-odd (κ_{AZZ}) HZZ coupling parameters. The signal model is optimised to achieve the lowest possible statistical uncertainty. One common model is defined for both κ_{HZZ} and κ_{AZZ} parameters in case of Higgs boson production via gluon-fusion. In case of the vector boson fusion or an associated production with vector bosons, the signal contribution is modelled separately for the κ_{AZZ} ans κ_{HZZ} parameters.
In order to improve the sensitivity to anomalous couplings, the selected Higgs boson candidates are categorised according to the most probable Higgs boson production modes. The comparison of the expected and observed number of events simultaneously in each category sets constrains on the size of anomalous coupling parameters. In four out of the five categories, there are more observed than expected events.
For the CP-odd coupling parameter κ_{AZZ} the values in the range $(-\infty, -11.3) \cup (-2.0, 1.9) \cup (2.3, \infty)$ and for CP-even κ_{HZZ} parameter $(-\infty, 2.0) \cup (8.3, \infty)$ are excluded at the 95% confidence level, while the expected ranges were $(-\infty, -7.4) \cup (7.7, \infty)$ and $(-\infty, -8.4) \cup (5.5, \infty)$, respectively.
The allowed range is reduced by a factor of 4 to 10 compared to the exclusion limits from Run I data.

Appendix A

Monte Carlo Simulation Samples

A.1 Signal Samples

MC ID	Process	Generator
341505	SM Signal, ggF	Powheg+Pythia8+EvtGen
341518	SM Signal, VBF	Powheg+Pythia8+EvtGen
341964	SM Signal, WH	Pythia8+EvtGen
341947	SM Signal, ZH	Pythia8+EvtGen
342561	SM Signal, ttH	MadGraph5+Herwig+EvtGen

A.2 EFT Samples

A.2.1 ggF

MC ID	Process	Generator
344158	BSM Signal, `G_kSM1`	MadGraph5+Pythia8+EvtGen
344159	BSM Signal, `G_kHVV1_kSM0`	MadGraph5+Pythia8+EvtGen
344160	BSM Signal, `G_kHVV6_kSM1`	MadGraph5+Pythia8+EvtGen
344161	BSM Signal, `G_kHVVm6_kSM1`	MadGraph5+Pythia8+EvtGen
344162	BSM Signal, `G_kAVV1_kSM0`	MadGraph5+Pythia8+EvtGen
344163	BSM Signal, `G_kAVV6_kSM1`	MadGraph5+Pythia8+EvtGen
344164	BSM Signal, `G_kAVVm6_kSM1`	MadGraph5+Pythia8+EvtGen
344165	BSM Signal, `G_kHVV6_kAVV6_kSM1`	MadGraph5+Pythia8+EvtGen
344166	BSM Signal, `G_kHVVm6_kAVVm6_kSM1`	MadGraph5+Pythia8+EvtGen

A.2.2 VBF

MC ID	Process	Generator
343247	BSM Signal, `V_kSM1`	MadGraph5+Pythia8+EvtGen
343249	BSM Signal, `V_kHVV10_kSM0`	MadGraph5+Pythia8+EvtGen
343259	BSM Signal, `V_kHVV5_kSM1`	MadGraph5+Pythia8+EvtGen
343260	BSM Signal, `V_kHVV2p5_kSM1`	MadGraph5+Pythia8+EvtGen
343261	BSM Signal, `V_kHVVm5_kSM1`	MadGraph5+Pythia8+EvtGen
343262	BSM Signal, `V_kHVVm2p5_kSM1`	MadGraph5+Pythia8+EvtGen
343252	BSM Signal, `V_kAVV15_kSM0`	MadGraph5+Pythia8+EvtGen
343253	BSM Signal, `V_kAVV5_kSM1`	MadGraph5+Pythia8+EvtGen
343254	BSM Signal, `V_kAVV2p5_kSM1`	MadGraph5+Pythia8+EvtGen
343255	BSM Signal, `V_kAVVm5_kSM1`	MadGraph5+Pythia8+EvtGen
343256	BSM Signal, `V_kAVVm2p5_kSM1`	MadGraph5+Pythia8+EvtGen

A.2.3 VH

MC ID	Process	Generator
344135	BSM Signal, `V_kSM1`	MadGraph5+Pythia8+EvtGen
344140	BSM Signal, `V_kHVV10_kSM0`	MadGraph5+Pythia8+EvtGen
344136	BSM Signal, `V_kHVV5_kSM1`	MadGraph5+Pythia8+EvtGen
344138	BSM Signal, `V_kHVV2p5_kSM1`	MadGraph5+Pythia8+EvtGen
344137	BSM Signal, `V_kHVVm5_kSM1`	MadGraph5+Pythia8+EvtGen
344139	BSM Signal, `V_kHVVm2p5_kSM1`	MadGraph5+Pythia8+EvtGen
344145	BSM Signal, `V_kAVV15_kSM0`	MadGraph5+Pythia8+EvtGen
344141	BSM Signal, `V_kAVV5_kSM1`	MadGraph5+Pythia8+EvtGen
344143	BSM Signal, `V_kAVV2p5_kSM1`	MadGraph5+Pythia8+EvtGen
344142	BSM Signal, `V_kAVVm5_kSM1`	MadGraph5+Pythia8+EvtGen
344144	BSM Signal, `V_kAVVm2p5_kSM1`	MadGraph5+Pythia8+EvtGen

A.3 Irreducible ZZ^* Background

A.3.1 $q\bar{q}ZZ$

MC ID	Process	Generator
361603	$q\bar{q}ZZ$	Powheg+Pythia8+EvtGen
342556		Powheg+Pythia8+EvtGen

A.3.2 ggZZ

MC ID	Process	Generator
343212	ggZZ	Powheg+gg2vv+Pythia8+EvtGen
343213		Powheg+gg2vv+Pythia8+EvtGen

A.4 Reducible Background

A.4.1 $t\bar{t}$

MC ID	Process	Generator
410000	$t\bar{t}$	Powheg+Pythia6+EvtGen
410009		Powheg+Pythia6+EvtGen
344171		Powheg+Pythia6+EvtGen

A.4.2 WH

MC ID	Process	Generator
361601	WH	Powheg+Pythia8+EvtGen

A.4.3 Z+jets

MC ID	Process	Generator
361372	Zee, Pt0_70_CVetoBVeto	Sherpa
361373	Zee_Pt0_70_CFilterBVeto	Sherpa
361374	Zee_Pt0_70_BFilter	Sherpa
361375	Zee_Pt70_140_CVetoBVeto	Sherpa
361376	Zee_Pt70_140_CFilterBVeto	Sherpa
361377	Zee_Pt70_140_BFilter	Sherpa
361378	Zee_Pt140_280_CVetoBVeto	Sherpa
361379	Zee_Pt140_280_CFilterBVeto	Sherpa
361380	Zee_Pt140_280_BFilter	Sherpa
361381	Zee_Pt280_500_CVetoBVeto	Sherpa
361382	Zee_Pt280_500_CFilterBVeto	Sherpa
361383	Zee_Pt280_500_BFilter	Sherpa
361384	Zee_Pt500_700_CVetoBVeto	Sherpa
361385	Zee_Pt500_700_CFilterBVeto	Sherpa
361386	Zee_Pt500_700_BFilter	Sherpa
361387	Zee_Pt700_1000_CVetoBVeto	Sherpa
361388	Zee_Pt700_1000_CFilterBVeto	Sherpa
361389	Zee_Pt700_1000_BFilter	Sherpa
361390	Zee_Pt1000_2000_CVetoBVeto	Sherpa
361391	Zee_Pt1000_2000_CFilterBVeto	Sherpa
361392	Zee_Pt1000_2000_BFilter	Sherpa
361393	Zee_Pt2000_E_CMS_CVetoBVeto	Sherpa
361394	Zee_Pt2000_E_CMS_CFilterBVeto	Sherpa
361395	Zee_Pt2000_E_CMS_BFilter	Sherpa

MC ID	Process	Generator
361396	Zmumu_Pt0_70_CVetoBVeto	Sherpa
361397	Zmumu_Pt0_70_CFilterBVeto	Sherpa
361398	Zmumu_Pt0_70_BFilter	Sherpa
361399	Zmumu_Pt70_140_CVetoBVeto	Sherpa
361400	Zmumu_Pt70_140_CFilterBVeto	Sherpa
361401	Zmumu_Pt70_140_BFilter	Sherpa
361402	Zmumu_Pt140_280_CVetoBVeto	Sherpa
361403	Zmumu_Pt140_280_CFilterBVeto	Sherpa
361404	Zmumu_Pt140_280_BFilter	Sherpa
361405	Zmumu_Pt280_500_CVetoBVeto	Sherpa
361406	Zmumu_Pt280_500_CFilterBVeto	Sherpa
361407	Zmumu_Pt280_500_BFilter	Sherpa
361408	Zmumu_Pt500_700_CVetoBVeto	Sherpa
361409	Zmumu_Pt500_700_CFilterBVeto	Sherpa
361410	Zmumu_Pt500_700_BFilter	Sherpa
361411	Zmumu_Pt700_1000_CVetoBVeto	Sherpa
361412	Zmumu_Pt700_1000_CFilterBVeto	Sherpa
361413	Zmumu_Pt700_1000_BFilter	Sherpa
361414	Zmumu_Pt1000_2000_CVetoBVeto	Sherpa
361415	Zmumu_Pt1000_2000_CFilterBVeto	Sherpa
361416	Zmumu_Pt1000_2000_BFilter	Sherpa
361417	Zmumu_Pt2000_E_CMS_CVetoBVeto	Sherpa
361418	Zmumu_Pt2000_E_CMS_CFilterBVeto	Sherpa
361419	Zmumu_Pt2000_E_CMS_BFilter	Sherpa

MC ID	Process	Generator
361420	Ztautau_Pt0_70_CVetoBVeto	Sherpa
361421	Ztautau_Pt0_70_CFilterBVeto	Sherpa
361422	Ztautau_Pt0_70_BFilter	Sherpa
361423	Ztautau_Pt70_140_CVetoBVeto	Sherpa
361424	Ztautau_Pt70_140_CFilterBVeto	Sherpa
361425	Ztautau_Pt70_140_BFilter	Sherpa
361426	Ztautau_Pt140_280_CVetoBVeto	Sherpa
361427	Ztautau_Pt140_280_CFilterBVeto	Sherpa
361428	Ztautau_Pt140_280_BFilter	Sherpa
361429	Ztautau_Pt280_500_CVetoBVeto	Sherpa
361430	Ztautau_Pt280_500_CFilterBVeto	Sherpa
361431	Ztautau_Pt280_500_BFilter	Sherpa
361432	Ztautau_Pt500_700_CVetoBVeto	Sherpa
361433	Ztautau_Pt500_700_CFilterBVeto	Sherpa
361434	Ztautau_Pt500_700_BFilter	Sherpa
361435	Ztautau_Pt700_1000_CVetoBVeto	Sherpa
361436	Ztautau_Pt700_1000_CFilterBVeto	Sherpa
361437	Ztautau_Pt700_1000_BFilter	Sherpa
361438	Ztautau_Pt1000_2000_CVetoBVeto	Sherpa
361439	Ztautau_Pt1000_2000_CFilterBVeto	Sherpa
361440	Ztautau_Pt1000_2000_BFilter	Sherpa
361441	Ztautau_Pt2000_E_CMS_CVetoBVeto	Sherpa
361442	Ztautau_Pt2000_E_CMS_CFilterBVeto	Sherpa
361443	Ztautau_Pt2000_E_CMS_BFilter	Sherpa
361443	Ztautau_Pt2000_E_CMS_BFilter	Sherpa

filtered Sherpa v2.1 (to be combined using Overlap Removal with the above Sherpa):

MC ID	Process	Generator
341103	Zee_4lMassFilter40GeV8GeV	Sherpa
341104	Zmumu_4lMassFilter40GeV8GeV	Sherpa
341105	Zee_3lPtFilter4GeV_4lMassVeto40GeV8GeV	Sherpa
341106	Zmumu_3lPtFilter4GeV_4lMassVeto40GeV8GeV	Sherpa

A.4.4 Tribosons and $t\bar{t}$

MC ID	Process	Generator
361621	WWZ ($4\ell 2\nu$)	Sherpa
361623	WZZ ($5\ell 1\nu$)	Sherpa
361625	ZZZ ($6\ell 0\nu$)	Sherpa
361626	ZZZ ($4\ell 2\nu$)	Sherpa
410069	ttZ	MadGraph5+Pythia8+EvtGen
410069	ttZ	MadGraph5+Pythia8+EvtGen
410070	ttZ	MadGraph5+Pythia8+EvtGen

Appendix B

Trigger Details

Table B.1: Summary of electron trigger items used in Run II in different data taking periods in 2015 (D-J) and 2016 (A-F).

Data Period	Single-Electron	Di-Electron	Tri-Electron
2015 D-J	HLT_e24_lhmedium_L1EM18VH HLT_e24_lhmedium_L1EM20VH HLT_e60_lhmedium e120_lhloose	HLT_2e12_lhloose_L12EM10VH	HLT_e17_lhloose_2e9_lhloose
2016 A	HLT_e24_lhtight_nod0_ivarloose HLT_e60_lhmedium_nod0 HLT_e60_medium HLT_e140_lhloose_nod0 HLT_e300_etcut	HLT_2e15_lhvloose_nod0_L12EM13VH	HLT_e17_lhloose_nod0_2e9_lhloose_nod0
2016 B-D3	HLT_e24_lhtight_nod0_ivarloose HLT_e60_lhmedium_nod0 HLT_e60_medium HLT_e140_lhloose_nod0 HLT_e300_etcut	HLT_2e15_lhvloose_nod0_L12EM13VH	HLT_e17_lhloose_nod0_2e9_lhloose_nod0
2016 D4-E	HLT_e26_lhtight_nod0_ivarloose HLT_e60_lhmedium_nod0 HLT_e60_medium HLT_e140_lhloose_nod0	HLT_2e17_lhvloose_nod0	HLT_e17_lhmedium_nod0_2e9_lhmedium_nod0
2016 F	HLT_e26_lhtight_nod0_ivarloose HLT_e60_lhmedium_nod0 HLT_e60_medium HLT_e140_lhloose_nod0	HLT_2e17_lhvloose_nod0	HLT_e17_lhmedium_nod0_2e9_lhmedium_nod0

Table B.2: Summary of muon trigger items used in Run II in different data taking periods in 2015 (D-J) and 2016 (A-F).

Data Period	Single-Muon	Di-Muon	Tri-Muon
2015	HLT_mu20_iloose_L1MU15	HLT_2mu10	HLT_3mu6
D-J	HLT_mu40	HLT_mu18_mu8noL1	HLT_3mu6_msonly
	HLT_mu60_0eta105_msonly		HLT_mu18_2mu4noL1
2016	HLT_mu24_ivarloose_L1MU15	HLT_2mu10	HLT_mu20_2mu4noL1
A	HLT_mu24_iloose_L1MU15	HLT_2mu10_nomucomb	HLT_3mu4
	HLT_mu40	HLT_mu20_mu8noL1	HLT_mu6_2mu4
	HLT_mu50	HLT_mu20_nomucomb_mu6noL1_nscan03	HLT_mu11_nomucomb_2mu4noL1_nscan03 _L1MU11_2MU6
			HLT_mu20_msonly_mu10noL1_msonly_nscan05 _noComb
2016	HLT_mu24_ivarmedium	HLT_2mu14	HLT_mu20_2mu4noL1
B-D3	HLT_mu24_imedium	HLT_2mu14_nomucomb	HLT_3mu6
	HLT_mu50	HLT_mu20_mu8noL1	HLT_mu6_2mu4
		HLT_mu20_nomucomb_mu6noL1_nscan03	HLT_mu11_nomucomb_2mu4noL1_nscan03 _L1MU11_2MU6
			HLT_mu20_msonly_mu10noL1_msonly_nscan05 _noComb
2016	HLT_mu24_ivarmedium	HLT_2mu14	HLT_mu20_2mu4noL1
D4-E	HLT_mu24_imedium	HLT_mu20_mu8noL1	HLT_3mu6_msonly
	HLT_mu26_ivarmedium	HLT_mu22_mu8noL1	
	HLT_mu26_imedium		
	HLT_mu50		
2016	HLT_mu26_ivarmedium	HLT_2mu14	HLT_mu20_2mu4noL1
F	HLT_mu26_imedium	HLT_mu22_mu8noL1	HLT_3mu6_msonly
	HLT_mu50		

Table B.3: Summary of mixed-lepton-flavour trigger items used in Run II in different data taking periods in 2015 (D-J) and 2016 (A-F).

Data Period	Electron-Muon
2015	HLT_e17_lhloose_mu14
D-J	HLT_2e12_lhloose_mu10
	HLT_e12_lhloose_2mu10
	HLT_e24_medium_L1EM20VHI_mu8noL1
	HLT_e7_medium_mu24
2016	HLT_e17_lhloose_nod0_mu14
A	HLT_e24_lhmedium_nod0_L1EM20VHI_mu8noL1
	HLT_e7_lhmedium_nod0_mu24
	HLT_e12_lhloose_nod0_2mu10
	HLT_2e12_lhloose_nod0_mu10
2016	HLT_e17_lhloose_nod0_mu14
B-D3	HLT_e24_lhmedium_nod0_L1EM20VHI_mu8noL1
	HLT_e7_lhmedium_nod0_mu24
	HLT_e12_lhloose_nod0_2mu10
	HLT_2e12_lhloose_nod0_mu10
2016	HLT_e7_lhmedium_mu24
D4-E	HLT_e12_lhloose_2mu10
	HLT_2e12_lhloose_mu10
	HLT_e12_lhloose_nod0_2mu10
	HLT_2e12_lhloose_nod0_mu10
2016	HLT_e7_lhmedium_mu24
F	HLT_e12_lhloose_2mu10
	HLT_2e12_lhloose_mu10
	HLT_e12_lhloose_nod0_2mu10
	HLT_2e12_lhloose_nod0_mu10

Appendix C

List of Events with Higgs Boson Candidates

Table C.1: Four-lepton Higgs boson candidates in the Run II 13 TeV dataset recorded by the ATLAS detector and corresponding to a total integrated luminosity of 14.78 fb^{-1} (Run 280464 - 302919).

Run	Event	m_{12} [GeV]	m_{34} $[GeV]$	$m_{4\ell}$ [GeV]
280464	517140616	89.59	26.81	122.52
280977	495555764	71.84	23.83	122.2
280862	53564866	90.96	29.04	128.85
281411	1837138326	77.21	27.99	120.52
301932	159220602	89.82	13.01	128.34
301932	3390806694	84.30	29.70	118.51
302053	1949966353	72.34	28.46	121.13
302053	3271474931	84.09	19.04	119.65
302053	1248835918	93.00	31.16	123.45
302269	80338044	83.50	15.85	121.56
302300	2460399326	91.69	28.80	124.07
302300	3834964681	60.48	48.68	120.68
302300	1168124247	74.69	23.39	126.78
302347	1459480495	91.12	27.66	121.86
302347	608963300	89.96	33.83	126.52
302393	3342707940	92.79	14.69	120.06
302393	2746009326	91.00	24.03	127.82
302831	111950763	86.31	30.36	121.48
302919	131533062	85.82	24.72	123.81

Table C.2: Four-lepton Higgs boson candidates in the Run II 13 TeV dataset recorded by the ATLAS detector and corresponding to a total integrated luminosity of 14.78 fb^{-1} (Run 302956 - 300687).

Run	Event	m_{12} [GeV]	m_{34} $[GeV]$	$m_{4\ell}$ [GeV]
302956	2583903696	79.40	29.84	121.45
302956	3316963258	89.79	21.53	122.45
302956	452658230	73.76	18.22	122.19
302956	709427174	69.04	34.91	126.08
303208	4632160483	89.23	30.14	124.61
303266	431580697	89.04	27.64	124.34
303291	533861945	72.38	24.82	122.59
303304	1915090587	84.72	22.46	126.32
303338	1376431034	91.14	29.13	123.99
303338	2362445226	87.73	29.72	122.99
303338	1223367860	85.10	35.16	123.66
303338	1501598340	59.61	53.14	128.09
303421	4191506075	89.99	33.79	128.41
303421	607776288	93.33	13.75	122.98
303499	3344658393	75.94	22.92	126.52
303499	3299080424	87.18	24.23	125.09
303499	3522604915	87.43	24.72	126.65
303499	4831692265	87.60	18.58	127.47
303638	2204429224	66.72	19.78	120.96
303832	827833045	90.63	20.14	125.55
303846	4607651319	70.96	32.35	122.23
303892	5068951074	91.11	22.27	125.66
303892	3100819624	86.97	23.95	125.93
300600	480791607	89.53	32.55	123.73
300687	457104229	91.66	20.22	125.88

C List of Figures

Bibliography

[1] L. Evans and P. Bryant, *LHC Machine*, JINST **3** (2008) S08001.

[2] ATLAS Collaboration, *Observation of a new particle in the search for the Standard Model Higgs boson with the ATLAS detector at the LHC*, Phys. Lett. B **716** (2012) 1 – 29.

[3] C. Collaboration, *Observation of a new boson at a mass of 125 GeV with the CMS experiment at the LHC*, Phys. Lett. B **716** (2012) 30 – 61.

[4] ATLAS Collaboration, G. Aad et al., *Evidence for the spin-0 nature of the Higgs boson using ATLAS data*, Phys. Lett. **B726** (2013) 120–144, arXiv:1307.1432 [hep-ex].

[5] CMS Collaboration, V. Khachatryan et al., *Constraints on the spin-parity and anomalous HVV couplings of the Higgs boson in proton collisions at 7 and 8 TeV*, Phys. Rev. **D92** (2015) , arXiv:1411.3441 [hep-ex].

[6] ATLAS, CMS Collaboration, G. Aad et al., *Measurements of the Higgs boson production and decay rates and constraints on its couplings from a combined ATLAS and CMS analysis of the LHC pp collision data at $\sqrt{s} = 7$ and 8 TeV*, JHEP **08** (2016) 045, arXiv:1606.02266 [hep-ex].

[7] LHC Higgs Cross Section Working Group Collaboration, J. R. Andersen et al., *Handbook of LHC Higgs Cross Sections: 3. Higgs Properties*, arXiv:1307.1347 [hep-ph].

[8] M. E. Peskin and D. V. Schroeder, *An Introduction To Quantum Field Theory (Frontiers in Physics)*, Westview Press, 1995.

[9] M. Schwartz, *Quantum Field Theory and the Standard Model*, Cambridge University Press, 2014.

[10] M. Böhm, A. Denner, and H. Joos, *Gauge theories of strong and electroweak interactions; 3rd ed*, B. G. Teubner, Stuttgart, 2001.

[11] D. J. Griffiths, *Introduction to elementary particles; 2nd rev. version*, Physics textbook. Wiley, New York, NY, 2008.

[12] A. Einstein, *Die Grundlage der allgemeinen Relativitätstheorie*, Annalen der Physik **354** (1916) 769–822.

[13] F. Englert and R. Brout, *Broken Symmetry and the Mass of Gauge Vector Mesons*, Phys. Rev. Lett. **13** (August, 1964) 321–323.

[14] P. W. Higgs, *Broken Symmetries and the Masses of Gauge Bosons*, Phys. Rev. Lett. **13** (October, 1964) 508–509.

[15] A. Purcell, *Go on a particle quest at the first CERN webfest. Le premier webfest du CERN se lance à la conquête des particules*, BUL-NA-2012-269 (August, 2012) 10. `https://cds.cern.ch/record/1473657`.

[16] S. L. Glashow, *Partial Symmetries of Weak Interactions*, Nucl. Phys. **22** (1961) 579–588.

[17] A. Salam, *Weak and Electromagnetic Interactions*, Conf. Proc. **C680519** (1968) 367–377.

[18] S. Weinberg, *A Model of Leptons*, Phys. Rev. Lett. **19** (November, 1967) 1264–1266.

[19] P. W. Higgs, *Broken symmetries, massless particles and gauge fields*, Phys. Lett. **12** (1964) 132–133.

[20] P. W. Higgs, *Spontaneous Symmetry Breakdown without Massless Bosons*, Phys. Rev. **145** (May, 1966) 1156–1163.

[21] G. S. Guralnik, C. R. Hagen, and T. W. B. Kibble, *Global Conservation Laws and Massless Particles*, Phys. Rev. Lett. **13** (November, 1964) 585–587.

[22] T. W. B. Kibble, *Symmetry Breaking in Non-Abelian Gauge Theories*, Phys. Rev. **155** (March, 1967) 1554–1561.

[23] J. Bernstein, *Spontaneous symmetry breaking, gauge theories, the Higgs mechanism and all that*, Rev. Mod. Phys. **46** (January, 1974) 7–48.

[24] *Regularization and renormalization of gauge fields*, Nucl. Phys. B **44** (1972) 189 – 213.

[25] *Renormalization of massless Yang-Mills fields*, Nucl. Phys. B **33** (1971) 173 – 199.

[26] *Renormalizable Lagrangians for massive Yang-Mills fields*, Nucl. Phys. B **35** (1971) 167 – 188.

[27] *Particle data group Live*, Accessed on: 2016-10-08, `http://pdglive.lbl.gov/`.

[28] Y. Nambu and G. Jona-Lasinio, *Dynamical Model of Elementary Particles Based on an Analogy with Superconductivity. I*, Phys. Rev. **122** (April, 1961) 345–358.

[29] N. Cabibbo, *Unitary Symmetry and Leptonic Decays*, Phys. Rev. Lett. **10** (1963) 531–533.

[30] M. Kobayashi and T. Maskawa, *CP Violation in the Renormalizable Theory of Weak Interaction*, Prog. Theor. Phys. **49** (1973) 652–657.

[31] *Sherpa and Open Science Grid: Predicting the emergence of jets*, Accessed on: 2016-10-08, `https://sciencenode.org/feature/sherpa-and-open-science-grid-predicting-emergence-jets.php`.

[32] J. C. Collins and D. E. Soper, *The Theorems of Perturbative QCD*, Ann. Rev. Nucl. Part. Sci. **37** (1987) 383–409.

[33] *Deep inelastic electron scattering in perturbation theory*, Phys. Lett. B **37** (1971) 78 – 80.

[34] *Asymptotic freedom in parton language*, Nucl. Phys. B **126** (1977) 298 – 318.

[35] *The anatomy of electroweak symmetry breaking: Tome I: The Higgs boson in the Standard Model*, Phys. Rep. **457** (2008) 1 – 216.

[36] , Accessed on: 2016-08-08, *LHC Higgs Cross Section Working Group*, `https://twiki.cern.ch/twiki/bin/view/LHCPhysics/LHCHXSWG`.

[37] P. Langacker, *The Standard Model and Beyond*, Series in High Energy Physics, Cosmology and Gravitation. CRC Press, 2009.

[38] ATLAS Collaboration, G. Aad et al., *Study of the spin and parity of the Higgs boson in diboson decays with the ATLAS detector*, Eur. Phys. J. **C75** (2015) 476, `arXiv:1506.05669 [hep-ex]`.

[39] Y. Gao, A. V. Gritsan, Z. Guo, K. Melnikov, M. Schulze, and N. V. Tran, *Spin determination of single-produced resonances at hadron colliders*, Phys. Rev. **D81** (2010) 075022, `arXiv:1001.3396 [hep-ph]`.

[40] P. Artoisenet et al., *A framework for Higgs characterisation*, JHEP **11** (2013) 043, `arXiv:1306.6464 [hep-ph]`.

[41] CMS Collaboration, S. Chatrchyan et al., *Study of the Mass and Spin-Parity of the Higgs Boson Candidate Via Its Decays to Z Boson Pairs*, Phys. Rev. Lett. **110** (2013) 081803, `arXiv:1212.6639 [hep-ex]`.

[42] CMS Collaboration, V. Khachatryan et al., *Constraints on the spin-parity and anomalous HVV couplings of the Higgs boson in proton collisions at 7 and 8 TeV*, Phys. Rev. **D92** (2015) 012004, arXiv:1411.3441 [hep-ex].

[43] ATLAS, CMS Collaboration, G. Aad et al., *Combined Measurement of the Higgs Boson Mass in pp Collisions at $\sqrt{s} = 7$ and 8 TeV with the ATLAS and CMS Experiments*, Phys. Rev. Lett. **114** (2015) 191803, arXiv:1503.07589 [hep-ex].

[44] Y. Gao, A. V. Gritsan, Z. Guo, K. Melnikov, M. Schulze, and N. V. Tran, *Spin determination of single-produced resonances at hadron colliders*, Phys. Rev. D **81** (April, 2010) 075022.

[45] A. L. Read, *Presentation of search results: the CL s technique*, Journal of Physics G: Nuclear and Particle Physics **28** (2002) 2693. http://stacks.iop.org/0954-3899/28/i=10/a=313.

[46] C. De Melis, *The CERN accelerator complex, Complexe des accélérateurs du CERN*, https://cds.cern.ch/record/2197559.

[47] ATLAS Collaboration, G. Aad et al., *Improved luminosity determination in pp collisions at $\sqrt{s} = 7$ TeV using the ATLAS detector at the LHC*, Eur. Phys. J. **C73** (2013) 2518, arXiv:1302.4393 [hep-ex].

[48] ATLAS Collaboration, *Luminosity Public Results Run2*, Accessed on: 2016-09-27, https://twiki.cern.ch/twiki/bin/view/AtlasPublic/LuminosityPublicResultsRun2.

[49] T. A. Collaboration, *The ATLAS Experiment at the CERN Large Hadron Collider*, J INSTRUM **3** (2008) S08003. http://stacks.iop.org/1748-0221/3/i=08/a=S08003.

[50] ATLAS Collaboration, G. Aad et al., *Performance of the ATLAS Trigger System in 2010*, Eur. Phys. J. **C72** (2012) 1849, arXiv:1110.1530 [hep-ex].

[51] A. Collaboration, *2015 start-up trigger menu and initial performance assessment of the ATLAS trigger using Run-2 data*, ATL-DAQ-PUB-2016-001 (March, 2016) . https://cds.cern.ch/record/2136007.

[52] ATLAS Collaboration Collaboration, *ATLAS inner detector: Technical Design Report, 1*, Technical Design Report ATLAS (1997) . https://cds.cern.ch/record/331063.

[53] ATLAS Collaboration Collaboration, S. Haywood, L. Rossi, R. Nickerson, and A. Romaniouk, *ATLAS inner detector: Technical Design Report, 2*, Technical

Design Report ATLAS (1997).
https://cds.cern.ch/record/331064.

[54] M. Capeans, G. Darbo, K. Einsweiller, M. Elsing, T. Flick, M. Garcia-Sciveres, C. Gemme, H. Pernegger, O. Rohne, and R. Vuillermet, *ATLAS Insertable B-Layer Technical Design Report*.
https://cds.cern.ch/record/1291633.

[55] ATLAS Collaboration Collaboration, *ATLAS liquid-argon calorimeter: Technical Design Report*, Technical Design Report ATLAS (1996) .
https://cds.cern.ch/record/331061.

[56] ATLAS Collaboration Collaboration, *ATLAS tile calorimeter: Technical Design Report*, Technical Design Report ATLAS (1996) .
https://cds.cern.ch/record/331062.

[57] ATLAS Collaboration Collaboration, *ATLAS muon spectrometer: Technical Design Report*, Technical Design Report ATLAS (1997) .
https://cds.cern.ch/record/331068.

[58] ATLAS Collaboration, G. Aad et al., *Muon reconstruction performance of the ATLAS detector in proton–proton collision data at $\sqrt{s}$ =13 TeV*, Eur. Phys. J. **C76** (2016) 292, arXiv:1603.05598 [hep-ex].

[59] J. Pequenao and P. Schaffner, *An computer generated image representing how ATLAS detects particles*, https://cds.cern.ch/record/1505342.

[60] C. Grupen and B. Schwartz, *Particle detectors*, Cambridge University Press, 2008.

[61] ATLAS Collaboration Collaboration, *Electron efficiency measurements with the ATLAS detector using the 2015 LHC proton-proton collision data*, ATLAS-CONF-2016-024 (June, 2016).
http://cds.cern.ch/record/2157687.

[62] W. Lampl, S. Laplace, D. Lelas, P. Loch, H. Ma, S. Menke, S. Rajagopalan, D. Rousseau, S. Snyder, and G. Unal, *Calorimeter Clustering Algorithms: Description and Performance*, ATL-LARG-PUB-2008-002 (April, 2008) .
https://cds.cern.ch/record/1099735.

[63] ATLAS Collaboration Collaboration, *Improved electron reconstruction in ATLAS using the Gaussian Sum Filter-based model for bremsstrahlung*, ATLAS-CONF-2012-047 (May, 2012).
https://cds.cern.ch/record/1449796.

[64] ATLAS Collaboration, G. Aad et al., *Electron performance measurements with the ATLAS detector using the 2010 LHC proton-proton collision data*, Eur. Phys. J. **C72** (2012) 1909, arXiv:1110.3174 [hep-ex].

[65] M. Cacciari, G. P. Salam, and G. Soyez, *The Anti-k(t) jet clustering algorithm*, JHEP **04** (2008) 063, arXiv:0802.1189 [hep-ph].

[66] *Selection of jets produced in 13TeV proton-proton collisions with the ATLAS detector*, ATLAS-CONF-2015-029 (July, 2015) . https://cds.cern.ch/record/2037702.

[67] *Jet Calibration and Systematic Uncertainties for Jets Reconstructed in the ATLAS Detector at* $\sqrt{s} = 13$ *TeV*, ATL-PHYS-PUB-2015-015 (July, 2015). https://cds.cern.ch/record/2037613.

[68] *Multi-Boson Simulation for 13 TeV ATLAS Analyses*, ATL-PHYS-PUB-2016-002 (January, 2016) . https://cds.cern.ch/record/2119986.

[69] S. Alioli, P. Nason, C. Oleari, and E. Re, *NLO Higgs boson production via gluon fusion matched with shower in POWHEG*, JHEP **04** (2009) 002, arXiv:0812.0578 [hep-ph].

[70] P. Nason and C. Oleari, *NLO Higgs boson production via vector-boson fusion matched with shower in POWHEG*, JHEP **02** (2010) 037, arXiv:0911.5299 [hep-ph].

[71] T. Sjöstrand, S. Mrenna, and P. Skands, *A brief introduction to PYTHIA 8.1*, Comput. Phys. Commun. **178** (2008) 852 – 867. http://www.sciencedirect.com/science/article/pii/S0010465508000441.

[72] D. J. Lange, *The EvtGen particle decay simulation package*, Nuclear Instruments and Methods in Physics Research Section A: Accelerators, Spectrometers, Detectors and Associated Equipment **462** (2001) 152 – 155. http://www.sciencedirect.com/science/article/pii/S0168900201000894.

[73] J. Alwall, R. Frederix, S. Frixione, V. Hirschi, F. Maltoni, O. Mattelaer, H. S. Shao, T. Stelzer, P. Torrielli, and M. Zaro, *The automated computation of tree-level and next-to-leading order differential cross sections, and their matching to parton shower simulations*, JHEP **07** (2014) 079, arXiv:1405.0301 [hep-ph].

[74] M. Bahr et al., *Herwig++ Physics and Manual*, Eur. Phys. J. **C58** (2008) 639–707, arXiv:0803.0883 [hep-ph].

[75] ATLAS Collaboration, G. Aad et al., *Measurement of the* Z/γ^* *boson transverse momentum distribution in* pp *collisions at* $\sqrt{s}$ *= 7 TeV with the ATLAS detector*, JHEP **09** (2014) 145, arXiv:1406.3660 [hep-ex].

[76] F. Cascioli, T. Gehrmann, M. Grazzini, S. Kallweit, P. Maierhöfer, A. von Manteuffel, S. Pozzorini, D. Rathlev, L. Tancredi, and E. Weihs, *ZZ production at hadron colliders in NNLO QCD*, Phys. Lett. **B735** (2014) 311–313, arXiv:1405.2219 [hep-ph].

[77] M. Grazzini, S. Kallweit, and D. Rathlev, *ZZ production at the LHC: fiducial cross sections and distributions in NNLO QCD*, Phys. Lett. **B750** (2015) 407–410, arXiv:1507.06257 [hep-ph].

[78] B. Biedermann, A. Denner, S. Dittmaier, L. Hofer, and B. Jäger, *Electroweak corrections to $pp \to \mu^+\mu^- e^+ e^- + X$ at the LHC: a Higgs background study*, Phys. Rev. Lett. **116** (2016) 161803, arXiv:1601.07787 [hep-ph].

[79] *gg2VV - Parton-level integrator and event generator*, Accessed on: 2016-12-08, https://gg2vv.hepforge.org/.

[80] F. Caola, K. Melnikov, R. Röntsch, and L. Tancredi, *QCD corrections to ZZ production in gluon fusion at the LHC*, Phys. Rev. **D92** (2015) 094028, arXiv:1509.06734 [hep-ph].

[81] J. M. Campbell, R. K. Ellis, M. Czakon, and S. Kirchner, *Two loop correction to interference in $gg \to ZZ$*, JHEP **08** (2016) 011, arXiv:1605.01380 [hep-ph].

[82] K. Melnikov and M. Dowling, *Production of two Z-bosons in gluon fusion in the heavy top quark approximation*, Phys. Lett. **B744** (2015) 43–47, arXiv:1503.01274 [hep-ph].

[83] T. Gleisberg, S. Hoeche, F. Krauss, M. Schonherr, S. Schumann, F. Siegert, and J. Winter, *Event generation with SHERPA 1.1*, JHEP **02** (2009) 007, arXiv:0811.4622 [hep-ph].

[84] ATLAS Collaboration, G. Aad et al., *The ATLAS Simulation Infrastructure*, Eur. Phys. J. **C70** (2010) 823–874, arXiv:1005.4568 [physics.ins-det].

[85] GEANT4 Collaboration, S. Agostinelli et al., *GEANT4: A Simulation toolkit*, Nucl. Instrum. Meth. **A506** (2003) 250–303.

[86] V. Kostyukhin, *VKalVrt - package for vertex reconstruction in ATLAS.*, ATL-PHYS-2003-031 (August, 2003) . https://cds.cern.ch/record/685551.

[87] ATLAS Collaboration Collaboration, *Study of the Higgs boson properties and search for high-mass scalar resonances in the $H \to ZZ^* \to 4\ell$ decay channel at $\sqrt{s}$ = 13 TeV with the ATLAS detector*, ATLAS-CONF-2016-079 (August, 2016) . http://cds.cern.ch/record/2206253.

[88] *A morphing technique for signal modelling in a multidimensional space of coupling parameters*, ATL-PHYS-PUB-2015-047 (November, 2015) . https://cds.cern.ch/record/2066980.

[89] G. Cowan, K. Cranmer, E. Gross, and O. Vitells, *Asymptotic formulae for likelihood-based tests of new physics*, Eur. Phys. J. **C71** (2011) 1554, arXiv:1007.1727 [physics.data-an].